THESIS ON NATURAL AND EXACT SCIENCES B212

Hybrid PET/MR Imaging of Bone Metabolism and Morphology

ANDREI ŠAMARIN

TUT PRESS

TALLINN UNIVERSITY OF TECHNOLOGY
Technomedicum
Department of Biomedical Engineering

Dissertation was accepted for the defence of the degree of Doctor of Philosophy in Biomedical Technology on April 6, 2016.

Supervisor: Professor Sergei Nazarenko, MD, PhD,
Technomedicum, Tallinn University of Technology and
Department of Nuclear Medicine, North Estonia Medical Centre, Estonia

Co-supervisor: Professor Gustav von Schulthess, MD, PhD, MD hon,
Department of Medical Radiology and Nuclear Medicine, University Hospital Zurich, Switzerland

Opponents: Associate Professor Andrei Iagaru, MD, Division of Nuclear Medicine and Molecular Imaging, Stanford School of Medicine, Stanford University Medical Center, USA

Professor Juhani Knuuti, MD, PhD, Turku PET Centre,
University of Turku and Turku University Hospital, Finland

Defence of the thesis: July 4, 2016

Declaration:

Hereby I declare that this doctoral thesis, my original investigation and achievement, submitted for the doctoral degree at Tallinn University of Technology has not been submitted for any other academic degree.

/Andrei Šamarin/

European Union
Regional Development Fund
Investing in your future

ISSN 1406-4723
ISBN 978-9949-23-955-9 (publication)
ISBN 978-9949-23-956-6 (PDF)

LOODUS- JA TÄPPISTEADUSED B212

Luustiku ainevahetuse ja morfoloogia hübriidkuvamine positronemissioontomograafia ja magnetresonantstomograafia abil

ANDREI ŠAMARIN

TTÜ
KIRJASTUS

CONTENTS

List of Publications

I Samarin A, Kuhn FP, Brandsberg F, von Schulthess G, Burger IA. Image registration accuracy of an in-house developed patient transport system for PET/CT+MR and SPECT+CT imaging. Nucl Med Commun. 2015 Feb;36(2):194-200.

II Samarin A, Burger C, Wollenweber SD, Crook DW, Burger IA, Schmid DT, von Schulthess GK, Kuhn FP. PET/MR imaging of bone lesions – implications for PET quantification from imperfect attenuation correction. Eur J Nucl Med Mol Imaging. 2012 July;39:1154-1160

III Samarin A, Hüllner M, Queiroz MA, Stolzmann P, Burger IA, von Schulthess G, Veit-Haibach P. 18F-FDG-PET/MR increases diagnostic confidence in detection of bone metastases compared with 18F-FDG-PET/CT. Nucl Med Commun. 2015 Dec; 36(12):1165-73

Author's Contribution to the Publications:

Publication I: study design, analysis of the images, statistical analysis of the data, writing of the manuscript

Publication II: study design, conduction of the study including modification and reconstruction of image data, analysis of the images, statistical analysis of the data, writing of the manuscript

Publication III: study design, analysis of the images, interpretation of the data, writing of the manuscript

Approbation

1. **A. Samarin**, C. Burger, D.W. Crook, I.A. Burger, D.T. Schmid, G.K. von Schulthess, F.P. Kuhn. Bone tissue and body region-specific variability of errors in SUV values: implications on attenuation correction methods in MR-PET (abstract). Insights Imaging (2012) 3 (Suppl 1):S242-B-0479. European Congress of Radiology. ECR 2012. Vienna, Austria. March 1–5, 2012

2. **A. Samarin**, C. Burger, F. P. Kuhn, D. T. Schmid, G. K. von Schulthess. The Influence of Bone Attenuation on Tracer Uptake Values of Bone Lesions of Different Composition in PET Imaging (abstract). Eur J Nucl Med Mol Imaging (2011) 38 (Suppl 2):S156-OP313. Annual Congress of European Association of Nuclear Medicine. EANM 2011. Birmingham, United Kingdom, October 15-19, 2011

3. **A. Samarin**, F. P. Kuhn, D. W. Crook, F. Wiesinger, S. D. Wollenweber, G. K. von Schulthess, J. Hodler, D. T. Schmid. Image Registration Accuracy of a Sequential, Tri-modality PET/CT+MR Imaging Setup Using Dedicated Patient Transporter Systems (abstract). Eur J Nucl Med Mol Imaging (2011) 38 (Suppl 2):S220-OP621. Annual Congress of European Association of Nuclear Medicine. EANM 2011. Birmingham, United Kingdom, October 15-19, 2011

4. F. P. Kuhn, **A. Samarin**, D. W. Crook, I. Burger, S. Wollenweber, P. Crandall, F. Brandsberg, G. K. von Schulthess, D. T. Schmid. Sequential multi-modality MR-PET/CT imaging: enabling MR coil removal between MR and PET/CT using a 'glove approach' (abstract). Eur J Nucl Med Mol Imaging (2011) 38 (Suppl 2):S221-OP622. Annual Congress of European Association of Nuclear Medicine. EANM 2011. Birmingham, United Kingdom, October 15-19, 2011

5. D. W. Crook, F. P. Kuhn, **A. Samarin,** C. Mader, T. Hany, J. Hodler, G. K von Schulthess, D. T. Schmid. Comparison of PET/MR with PET/CT findings in the abdomen using a sequential MR-PET/CT system (abstract). Eur J Nucl Med Mol Imaging (2011) 38 (Suppl 2):S157-OP317
Annual Congress of European Association of Nuclear Medicine. EANM 2011. Birmingham, United Kingdom, October 15-19, 2011

6. **A. Samarin**, C. Burger, F. P. Kuhn, G. K. von Schulthess. The Implementation of Tracer Uptake Adjustment Atlases for Correction of Bone Attenuation in PET (abstract). Eur J Nucl Med Mol Imaging (2011) 38 (Suppl 2):S291-P131
Annual Congress of European Association of Nuclear Medicine. EANM 2011. Birmingham, United Kingdom, October 15-19, 2011

INTRODUCTION

Cancer is serious medical and social problem causing humanitarian and economic losses worldwide. Appearance of bone metastases demonstrates that cancer is entering an advanced stage which seriously complicates clinical history as well as management of this disease (Roodman 2004). In recent years a paradigm shift in cancer control is observed towards implementation of precision medicine tools (Prasad et al. 2016). The concept of precision medicine that takes individual disease variability into account for prevention and treatment has the full potential to give everyone the best chance at good health (Collins and Varmus 2015). To achieve this goal powerful methods for characterizing the patients and the disease are needed. Hybrid PET/CT and PET/MR imaging methods using various biomarkers provide a molecular approach to diagnose cancer and assess treatment response. Non-invasive evaluation of bone with regards to the presence of bone metastases enables accurate staging and selection of the optimum treatment of the oncological patient as well as prognosis determination.

With the introduction of fully integrated whole body PET/CT cameras (Beyer et al. 2000), a new area in nuclear medicine has opened. PET/CT technology offers a sequential combination of anatomic information provided by diagnostic CT and imaging of physiology by PET in one integrated device. PET/CT integration is truly synergistic as CT allows anatomical localization and morphological characterization of the metabolic alterations detected by PET as well as providing attenuation correction data. It has become quickly apparent that diagnostic accuracy of integrated PET/CT is superior to PET alone, CT alone and PET and CT read side-by-side (Bar-Shalom et al 2003, Cohade et al 2003, Czernin et al 2007). As a result, the use of fluorine-18 fluorodeoxyglucose (FDG) PET/CT in tumour staging and therapy response assessment has increased markedly (Lardinois et al 2003, von Schulthess et al 2006). The acceptance and clinical use of the PET/CT was widespread and fast (Czernin et al 2007). PET/CT has become one of the mainstays of oncological imaging influencing therapeutic management in up to 36% of the examined patients (Hillner et al 2008).

Major efforts have been made to develop integrated PET/MR systems as MR imaging has certain advantages over CT. MR imaging provides higher soft tissue contrast allowing potentially better anatomical characterization of the disease in organs like brain, breast, liver and prostate, in head and neck and pelvic region and bone marrow (Czernin et al 2013). Furthermore, additional functional imaging capabilities of MR combined with anatomical information and PET data may provide new insights into disease phenotypes and biology (Czernin et al 2014). MR technology allows imaging without ionized radiation resulting in less radiation exposure in PET/MR systems in comparison to PET/CT, an important factor in vulnerable populations such as children and women of childbearing age (Miglioretti et al. 2013).

PET/MR as a whole body imaging modality became clinically available later than PET/CT. Substantial engineering efforts were required to overcome technical challenges (Wehrl et al. 2015). The technological tasks included the development of semiconductor-based light detectors insensitive to high magnetic fields and MR imaging based attenuation correction (AC) of PET data. While MR compatible avalanche photo-diodes based PET detectors have been successfully developed (Pichler et al 2006), MR based attenuation correction of PET data still remains a topic of active research (Attenberger et al 2015). It has been shown that in integrated PET/MR scanners the erroneous PET attenuation correction leads to substantially lower mean standardized uptake values (SUV) in bone tissue compared to PET/CT (Eiber et al 2014), the finding that may be especially important when assessing treatment response in bone metastases or comparing PET/CT and PET/MR studies.

Several imaging techniques are currently available for the detection of the metastatic bone lesions – whole body scintigraphy with technetium-99m methyl diphosphonate (MDP-WBS), CT, MR, PET/CT and PET/MR imaging (Choi and Raghavan 2012; Lecouvet et al. 2013; Schraml et al. 2015). Whole-body MR imaging has been shown to have superior diagnostic accuracy compared with CT and bone scintigraphy in detection of bone metastases because of its ability to assess early infiltration of bone marrow which precedes osteoblastic and osteoclastic response of the bone matrix to malignant tissue infiltration (Steinborn et al.; Engelhard et al. 2004; Mentzel et al. 2004; Yang et al. 2011; Lecouvet et al. 2013). Superiority of MR imaging over CT imaging in early detection of metastatic bone marrow infiltration generates expectation of superiority of PET/MR over PET/CT in respective clinical settings. However, the advantages of PET/MRI as a new technology in patient care need to be compared with PET/CT as a clinical standard.

This doctoral thesis aims on improvement of assessment of bone metabolism and morphology in patients with malignant disease using hybrid PET/MR imaging providing support for diagnosis, treatment and prognosis evaluation.

The doctoral thesis covers the methodology and the results of three studies performed for further development of quantitative PET/MR imaging and assessment of potential clinical utility of PET/MRI, particularly in patients with metastatic bone disease. The current work seeks the solution for accurate fusion of PET and MRI datasets acquired in stand-alone imaging systems that can potentially be solved by development and validation of novel dedicated patient transporter system. The impact of imperfect attenuation correction algorithms currently used in integrated PET/MR systems on bone lesion assessment was not previously fully understood and needed further investigation. We developed a robust approach that allowed to clarify this issue in multiple bone lesions in different parts of the skeletal system - an information potentially leading to improvement of the photon attenuation correction in integrated PET/MR systems. Besides necessary technical solutions, clinical utility of PET/MR in assessment bone morphology and metabolism needed further evaluation. For

this purpose FDG-PET/MR performance in assessment of bone lesions was compared with FDG-PET/CT imaging.

The first study (Publication I) describes implementation of the newly developed dedicated patient transporter system which enables hybrid sequential tri-modality PET/CT + MR imaging. The developed patient shuttle system allowed robust transfer of the patients between PET/CT and MR or SPECT/CT and diagnostic CT scanners, resulting in "hardware-based" fusion of the PET and MR datasets or SPECT and diagnostic CT images. Tri-modality PET/CT + MR setup served as a platform for further investigation of the technical challenges (Publication II) and clinical benefits (Publication III) of PET/MR imaging.

The second study (Publication II) investigates the fundamental issue of photon attenuation correction in integrated PET/MR imaging systems where X-ray based attenuation cannot be used. For this purpose MR based attenuation correction maps were simulated by “removing” bone with its high attenuation values on CT based attenuation maps, and replacing the affected regions with soft tissue specific attenuation values. This approach allowed to evaluate the consequence of using deficient attenuation correction and to point out the need for assigning correct attenuation coefficients for bone tissue in PET/MR imaging.

The third study (Publication III) focuses on the clinical evaluation of a PET/MR system by comparing the diagnostic performance of FDG-PET/MR with FDG-PET/CT in oncological patients with FDG avid bone metastases. In this study an optimized imaging protocol with reduced number of MR pulse sequences was designed thanks to availability of diagnostic information from PET. The MR protocol was without contrast administration and consisted of three MR pulse sequences that allow to perform whole-body PET/MR imaging approximately within the same time as a standard PET/CT.

ABBREVIATIONS

AC – attenuation correction
Ac-CT – computed tomography for attenuation correction
CoM – external cobalt-57 markers
CT – computed tomography
D-CT – diagnostic computed tomography
FDG – fluorine-18 fluorodeoxyglucose
MDP-WBS – whole body scintigraphy with technetium-99m methyl diphosphonate
MR – magnetic resonance
MR STIR – short TI inversion recovery magnetic resonance sequence
MR T1 water, fat, in-phase, out-phase – T1-weighted 3D dual-echo gradient-recalled echo pulse sequence, liver accelerated volume acquisition, corresponding water, fat, in-phase and out-phase reconstruction
MRI – magnetic resonance imaging
NaF – fluorine-18 sodium fluoride
PET – positron emission tomography
PETvol – metabolic tumour volume
PMT – photomultiplier tube
RF – radiofrequency
SD – standard deviation;
SUV – standardized uptake value
SUVmax – maximum standardized uptake value
SUVmean – mean standardized uptake value
TLG – total lesion glycolysis

1. HYBRID PET/MR IMAGING

Cancer is a major source of morbidity and mortality worldwide. Molecular imaging has a major role in diagnosis and management of malignant disease, currently mainly by using FDG as a tracer of energy metabolism. This to a certain extent provides a characterisation of biochemical signatures in an individual tumour, and it can be expected that - as cancer therapies move into an era of precision medicine (Leiblich et al. 2016) – other tracers will provide more specific biochemical information.

Bone metastases are a common complication of cancer and bone is the third most common organ affected by metastases, surpassed only by the lungs and the liver (O'Sullivan et al. 2015). Biological factors like higher blood flow in the areas of red bone marrow and the production of the adhesive molecules that allow binding to marrow stroma by disseminated tumour cells result in the high frequency of skeletal metastases (Woolf et al. 2015). Depending on the tumour type, skeletal metastases can cause an osteolytic reaction with destruction of the bone tissue (lytic metastases), an osteoblastic reaction with excessive bone formation (sclerotic metastases) or a mixed bone tissue response. Bone metastases often have devastating effects as osteolytic metastases can cause severe pain, pathologic fractures, life-threatening hypercalcemia, spinal cord compression and other neural compression syndromes (Roodman 2004). Osteoblastic metastases can cause bone pain and pathologic fractures because of the poor quality of the newly produced excessive bone tissue (Roodman 2004). Therefore early and confident detection of bone metastases enabling accurate staging and selection of the optimum treatment is essential in cancer patients. Once the diagnosis of bone metastases has been established, consistent, reproducible and validated imaging methods are the prerequisite of effective management of cancer patients (Woolf et al. 2015).

Hybrid PET/MR has the potential for accurate diagnosis, treatment response assessment and the surveillance of patients living with metastatic cancer.

1.1. General principles of PET and MR imaging

1.1.1. PET imaging

Positron emission tomography (PET) is based on detection of biologically active targeted molecules administered to the patient and labelled with a positron emitting radioactive isotope. These molecules are selected and applied upon their affinity to particular pathophysiological processes of interest. The positron emitted by the radioactive isotope interacts by annihilation with an electron of the surrounding tissue after very short travelling distance of typically less than 2 millimetres. As a result the annihilation reaction two 511 keV photons are emitted in opposite directions. The near-simultaneous detection of

both emitted photons by a ring of PET camera detectors identifies the line, along which the annihilation has occurred and from this, the location of the administered targeted molecule inside the human body can be inferred (Fig. 1). PET detectors consist of a high-density scintillator and a photomultiplier tube (PMT). The scintillator is used to convert the high-energy annihilation photons to multiple photons with much lower energy in the spectrum of visible light, which is then collected and amplified by the PMTs.

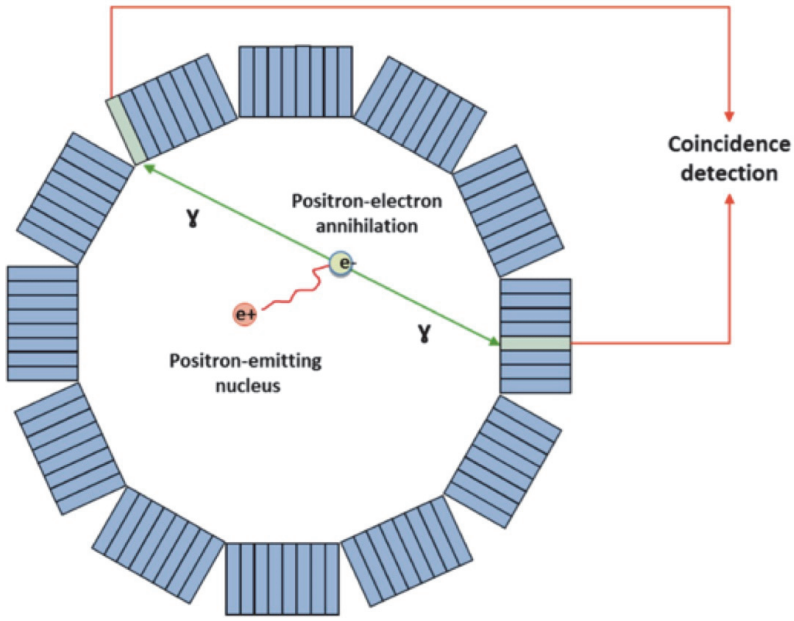

Fig. 1. PET imaging principle. A radioactive isotope emits a positron during its disintegration. The positron annihilates with an electron of the surrounding tissue producing gamma radiation in the form of two photons. The photons are emitted at an angle of nearly 180 degrees. When both photons interact with two of the scintillator crystals of the PET detector ring, a coincidence event is recorded and the location of the radioactive isotope can be established.
Adapted with permission from Gaspar Delso.
Source: Delso G et al. (2015) Abdom Imaging 40:1352-1357.

The detector positions, the energy of the photons and the precise timing of their detection are critical. This information is processed to localize the annihilation and reject – among others - the scattered photons due to Compton interactions with patient tissue or hardware placed in the field of view. A good timing accuracy of the PET detectors can be applied to narrow further localization of annihilation event by obtaining so called Time of Flight information, TOF. One of the main strengths of PET technology is its high sensitivity as in theory photons produced by just a few hundreds of molecules of

radiotracer at a given location can already be detected by a PET scanner (Delso et al. 2015).

1.1.2. PET attenuation correction

Several physical factors affect the correct visualisation of the tracer uptake in tissues in PET images. These factors include photon attenuation, scattered and random coincidences, detector efficiency variations, and scanner dead-time (Kinahan et al. 2003). The major factor is attenuation of the emitted photons in the human body and the hardware present in the field of view incorporating two types of interaction: photoelectric absorption and Compton scattering. These two phenomena can significantly affect both visual image quality and quantitative accuracy of the data. Improper photon attenuation correction of the PET data can lead to impaired detection of the lesions in the areas of non-uniform density (Kinahan et al. 2003). Therefore compensation for photon attenuation needs to be implemented in PET image reconstruction. Several approaches can be used for photon attenuation correction: transmission scans obtained from positron or gamma-ray emitting sources, x-ray sources and more recently, from MR imaging.

In PET scanners the transmission data needed to calculate the attenuation map can be recorded in coincidence-timing mode with an external source of radiation like a Ge-68/Ga-68 positron source (Kinahan et al. 2003). Another option is to use gamma-ray sources like Cs-137. The benefit of this gamma source is reduced transmission noise, but a drawback is a potential bias introduced by transforming the attenuation maps obtained at the 662 keV Cs-137 energy to annihilation gamma ray energy of 511 keV, and an increase in the fraction of scattered photons (Kinahan et al. 2003).

In integrated PET/CT scanners the CT scans can be used for PET attenuation correction purposes allowing to omit the separate, lengthy PET transmission scan. The use of the CT scan for attenuation correction leads to reduction of whole-body scan times by at least 30% and provides essentially noiseless attenuation correction factors compared to those from a standard PET transmission scan (Townsend et al. 2003). Additionally, this approach eliminates the issue of contamination of radionuclide-based transmission scans from emission photons. In CT based PET attenuation correction, the PET-attenuation maps at 511 keV are obtained by using a bilinear function to transform the Hounsfield unit CT maps, which are obtained at photon energies at around 70 keV (Kinahan et al. 1998; Burger et al. 2002). However, it should be kept in mind that mismatch between PET and CT images due to patient respiration, truncation of the CT field-of-view, the use of intravenous and oral CT contrast media, and the presence of metal objects can potentially lead to errors in CT based attenuation correction (Townsend et al. 2003).

In PET/MR scanners, MR images are used for photon attenuation correction. MR signal intensity usually is a complicated function of proton density and the T1- and T2-relaxation times. Therefore, a direct conversion of

the MR image signals to PET attenuation coefficients is not possible. Advanced MR image processing required for generation of MR based photon attenuation maps is an area of active research, as multiple factors can lead to inaccurate MR-based attenuation correction maps. These factors are inaccurate bone and lung tissue segmentation, motion-induced misregistration, RF coils in the PET field of view, B0 and B1 field inhomogeneities, metallic implants and MR contrast agents (Aznar et al. 2014; Attenberger et al. 2015).

1.1.3. MR imaging

The principle of MR imaging is based on the magnetic properties of the hydrogen nuclei inside mostly water and fat molecules and their interaction with different molecular environments. In clinical practice this provides the opportunity to characterize tissues with different structural and molecular properties. The MR imaging signal is generated by the manipulation of the magnetic moments of the protons, which have been aligned by a strong magnetic field. This manipulation is done by applying sequences of excitations through radiofrequency (RF) waves and recording the small signals of relaxation after the excitations detectable outside the body (Shah and Huang 2015). Localization of the origin of the signals from within the body and therefore generation of MR images is achieved by using additional magnetic fields. The recorded signal strengths are dependent on the different densities and relaxation properties of protons in different tissues. In order to improve transmission and reception of RF waves and therefore signal and image quality (Fig. 2), local radiofrequency coils (surface coils) can be placed directly on the patient body.

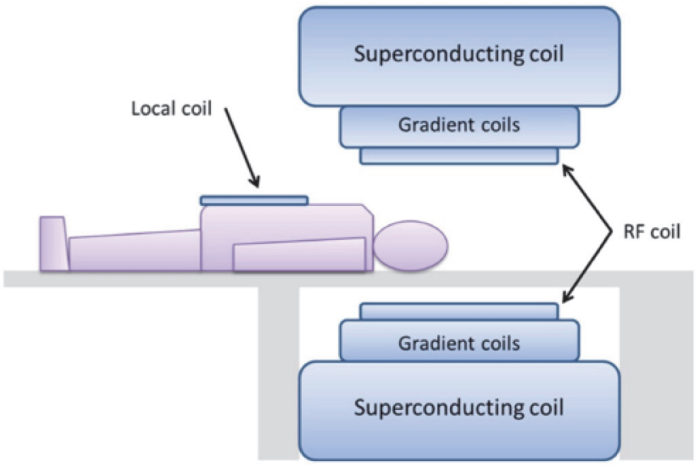

Fig. 2. Schematic sagittal view of an MR scanner. The permanent superconducting coil, gradient coils and RF coils are arranged as concentric cylinders around the patient opening. Local RF coils are placed on the patient for improved signal quality.
Adapted with permission from Gaspar Delso.
Source: Delso G et al. (2015) Abdom Imaging 40:1352-1357.

1.2. Hybrid PET/MR imaging: possibilities for combination of PET and MR technology.

PET and MR systems can be integrated in three major ways (von Schulthess and Schlemmer 2009). This allows characterization of tissue properties from different aspects including metabolism and morphology.

1.2.1. Separate imaging

The scanners are located in the different rooms, commonly far from each other. The patient needs to be offloaded from the one scanner and then get onto second scanner. The integration of PET and CT or MR data is performed by the fusion of PET and CT or MR datasets, respectively using dedicated software. The postural position of the patient on the scanner tables will not be exactly the same therefore causing spatial misregistration between the fused images. Integration of images from two separate devices with software-based image fusion is possible and has been used mainly for brain tumours (Grosu et al. 2005) and prostate (Park et al. 2012) or pelvic tumours (Vargas et al. 2013); however, in body applications, any positional change of the patient will impair fusion accuracy and therefore, software-only based fusion for PET and CT or MR is not considered to be an alternative to hardware integrated PET/CT (Kim et al. 2005) or PET/MR.

1.2.2. Sequential imaging

A dedicated patient transporter (shuttle) is used to integrate PET and CT or MR scanners. The idea is to eliminate patient motion and postural changes during the transfer between the two scanners and therefore achieve "hardware"-based image fusion. In PET/CT, the gantries of PET and CT are juxtaposed and axially aligned, so that axial table motion transfers the patient from one into the other gantry. PET- and MR scanners can be integrated by a similar patient table arrangement in a single room. In this setup the scanners are placed at a distance of 3 or more meters opposing each other and the patient table can swivel such that the patient can be moved into one or the other scanner. Alternatively, a patient shuttle is used, which relies on the undockable MR table. A flat patient transfer board is placed onto this shuttle. After the MR scan, the patient lying on the board is transferred with the board from the undocked MR table to the shuttle system. The shuttle is moved to the other room and patient still lying on the board is transferred on the board from shuttle system to the PET/CT table. This arrangement constitutes a triple-modality PET/CT-MR system. In both arrangements, there are no electromagnetic interferences between PET and MRI components and extensive technical modifications of the individual imaging systems are therefore not required (Spick et al. 2016).

Shuttle integration of two devices installed in two neighbouring rooms can help to make PET/MR integration more cost effective (von Schulthess and

Burger 2010), as this tri-modality imaging setup provides more flexibility in the operation, as the two standalone systems can be run in parallel and separately, which is not possible in a single room system. To reduce the overall imaging time, MR scanning can be performed first and during the PET tracer uptake time. The main drawback of such systems is non-simultaneity of the image acquisition and potential misregistration of the images due to patient motion.

1.2.3. Fully integrated systems

In this configuration PET and MR systems are integrated in one device allowing simultaneous data acquisition without patient or table motion when imaging single fields of view. The main advantages of an integrated device are simultaneous assessment of biological processes (perfusion, oxygenation, hypoxia and others) by PET and MR, substantial time saving due to simultaneous image acquisition and accurate registration of the resulting fused PET and MR images. Additional potential advantages in integrated PET/MR include motion correction of the PET images based on the navigator scans, multiple PET attenuation corrections during different breathing and heart phases, and MR-based PET reconstruction and partial volume correction (Wehrl et al. 2015). It is important to note that a simultaneous PET/CT system cannot be built, that is, PET/CT systems are always of the type discussed under 1.2.2.

However, multiple technological challenges needed to be solved before clinical whole-body integrated PET/MR imaging became a reality. MR compatible solid state PET detectors were developed (Pichler et al. 2006), as PMTs do not work properly in the high magnetic field, which deflects the path of the PMT electrons created by the photoelectric effect (Delso et al. 2015). In addition, special radiofrequency shielding and cooling by means of a constant flow of water or air were developed for the new PET photodetectors. On MR side the main coil and gradients of the wide-bore MR scanner were kept while the innermost radiofrequency coil was replaced with narrow-bore version making approximately 10 cm available for the PET detector ring to be inserted (Delso et al. 2015) (Fig. 3).

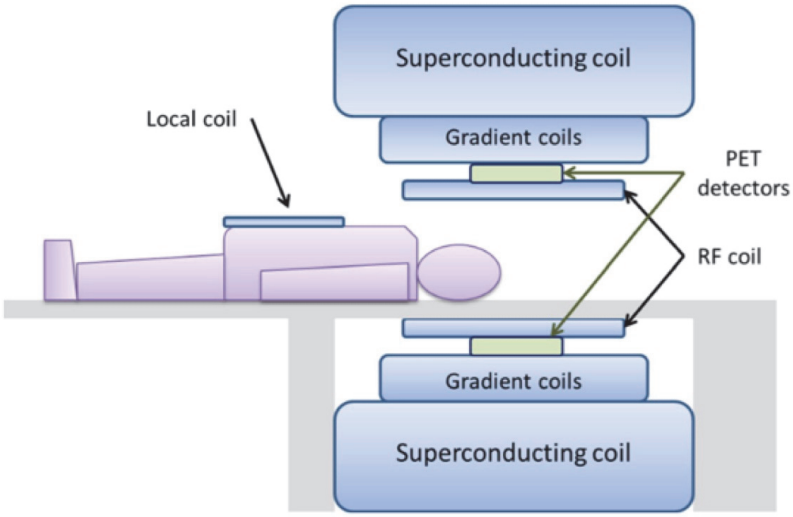

Fig 3. Integrated PET/MR scanner. MR compatible solid-state PET detectors are installed between the superconducting coil, gradient coils and radiofrequency coils. Adapted with permission from Gaspar Delso.
Source: Delso G et al. (2015) Abdom Imaging 40:1352-1357.

One of the major challenges of the integrated PET/MR system remains the accurate attenuation correction of the PET data. Variable photon attenuation in the human body and surrounding hardware will cause PET image degradation. Therefore measurement of the spatial distribution of the attenuation is the prerequisite to correct PET image reconstruction showing true tracer distributions and permitting semi-quantitative evaluation of images by measuring SUV (von Schulthess and Schlemmer 2009). For accurate reconstruction of the PET data it is of paramount importance to know where the attenuating elements such as gradient and surface coils are located inside the field of view of the scanner. Moreover, in integrated PET/MR scanners the redesign of the hardware placed in the field of view was needed (Delso et al. 2015).

1.3. MR based PET attenuation correction in integrated PET/MR systems

Accurate attenuation correction is essential for quantitative analysis of PET tracer distribution, especially for assessing treatment response and comparing PET/MR to PET/CT data. AC of PET data based on MR images is challenging (Hofmann et al. 2009). In PET/CT systems attenuation correction is straightforward as CT data reflecting the density of the patient tissues can be easily transformed into attenuation map at 511 kVp for PET using a bilinear function (Burger et al. 2002) relating mu-values to Hounsfield units. In contrast to CT data, intensity values in MR images do not reflect the X-ray density of tissues, but rather tissue proton densities and relaxation times (Beyer et al.

2008). Most critical is the differentiation of air from bone tissue as they have the lowest and highest attenuation coefficients, respectively, but both appear as a low signal structures in conventional MR sequences. Thus image processing of MR data is necessary for the generation of AC maps.

Proposed approaches to MR-based AC are tissue segmentation, the use of atlases or templates and pattern recognition techniques or a combination of these (Hofmann et al. 2008; Martinez-Möller et al. 2009; Schulz et al. 2011; Hofmann et al. 2011).

In commercially available integrated whole-body PET/MR scanners MR based PET attenuation correction relies on the four-class tissue segmentation (air, lungs, soft tissue, fat) that is performed based on a fast 3D T1-weighted gradient-echo sequence (Beyer et al. 2016). Then for each tissue class the predefined linear attenuation coefficients are applied to obtain a map for PET attenuation correction. However, this approach has certain limitations such as not correctly accounting for bone tissue, poor representation of the lung parenchyma (including incorrect segmentation due breathing artefacts), not accounting for interindividual variability in attenuation coefficients and sensitivity to the presence of metallic implants (Delso et al. 2015). The lack of cortical bone signal in standard MR sequences makes bone segmentation difficult, and therefore in the currently available integrated PET/MR systems bone tissue is ignored and treated as soft tissue in whole-body scans.

Several studies have evaluated the important issue of differences in attenuation correction in PET-imaging deriving from CT-based AC or MR-based AC. The topic of active research is a question whether it is necessary to segment bone in MR AC maps or whether the stronger attenuation of the 511 keV photons by bone can be replaced by the attenuation of soft tissue in such maps. Some investigators state that segmentation of CT images into three (background, lung and soft tissue) or four (back- ground, lungs, fat and soft tissue) tissue classes to generate attenuation maps does not substantially change PET data compared to the use of standard CT AC with a mean under-estimation of bone lesion SUV of 6.5% and 8%, respectively (Martinez-Möller et al. 2009; Schulz et al. 2011). In contrast, another study has shown that segmentation of whole-body CT data into four classes, while neglecting bone, results in SUV errors of > 10% in 58% of osseous lesions (Hofmann et al. 2011). Phantom studies demonstrated an increase of the relative error by up to 6.8% in the body and up to 31.0% for bony regions when the bones are ignored by the AC-algorithm. In simulated clinical studies, the mean relative error may be as high as 15% for body-lesions and 30.7% for bony lesions (Akbarzadeh et al. 2013). Differences for the head and brain are lower (Larsson et al. 2013). All these studies evaluated the effects on a lesion-by-lesion basis, but did not consider that bone lesion density can vary considerably spanning from lytic to sclerotic.

Those MR AC issues may have a potential impact on the evaluation of bone disease in simultaneous PET/MRI, especially for assessing treatment response and comparing PET/MR to PET/CT data.

One of the proposed approaches to retrospectively add bone information to attenuation correction maps is to use the data from previously generated atlases (atlas-based AC). However, the approach can fail when patient anatomy does not match the normal anatomy in atlases due to various anatomical variants and deformation of the tissues caused by disease (Boellaard and Quick 2015). Currently the most promising remedy is provided by ultrashort or zero echo time MR pulse sequences, which can directly visualize bone tissues by MRI (Robson and Bydder 2006; Keereman et al. 2010).

Despite active research and significant technological improvements, the issue of creating valid MR-based AC maps has not yet been solved in PET/MR technology. In a very recent study the whole-body MR-based AC was compared on three clinical PET/MR systems from different vendors (Beyer et al. 2016). Significant differences of MR based AC maps generated for the same subjects but different PET/MR systems was found therefore, limiting the quantitative use of PET/MR in multi-centre imaging studies (Beyer et al. 2016).

1.4. Advantages of hybrid imaging in diagnostic workup

Evolution of imaging technology resulted in development of the integrated PET/CT scanner that became clinically available at the turn of millennium. At University Hospital of Zurich, where the author of current thesis had the opportunity to familiarize himself with hybrid imaging, the first clinical PET/CT started operation in March 2001. Synergistic combination of morphological and functional imaging was successful and PET/CT became the reference standard in oncologic imaging in many centres (Spick et al. 2016). In hybrid PET/CT systems the alterations in metabolism detected by PET are accompanied by the detection of the corresponding structural changes by CT in one imaging session, therefore increasing the diagnostic accuracy. It has been shown that the accuracy of hybrid PET/CT for assessment of the cancers is higher than that of PET and CT alone (Lardinois et al. 2003; Schöder et al. 2004; Antoch et al. 2004; Hillner et al. 2008). The main reasons for the incremental value of hybrid PET/CT imaging compared to PET and CT alone are: mutually enhanced lesion detection on both CT and PET images, better anatomical localization of PET tracer uptake and assessment of structural changes on CT leading to better differentiation of physiologic from pathologic uptake, detection of lesions negative on PET scans and vice versa, CT-based attenuation correction of PET data.

PET and PET/CT have been shown to be highly influential on the management of the oncological patient. Hillner et al reported that incorporation of the tumour metabolism data provided by PET or PET/CT into the imaging strategy of the oncological patients influenced the intended patient management in one third (36.5%) of cases (Hillner et al. 2008).

The most commonly used biological marker in PET imaging is FDG. FDG is an analogue of glucose with the radioactive F-18 isotope substituting for the normal hydroxyl group at the second position in the glucose molecule. FDG

allows imaging of glucose uptake and metabolism. FDG has a half-life of 110 min and can be produced in large quantities, allowing the transfer of the radiopharmaceutical to sites without on-site cyclotron needed for its production. FDG-PET tumour imaging is based on the increased FDG uptake observed into malignant cells due to overexpression of the intracellular and cell membrane glucose transporter proteins and slow intracellular dephospholyration of FDG (Som et al. 1980). As a result, the distribution of FDG in the body allows detection of the tumour tissue, as malignant tumours most frequently show increased glycolytic activity compared to normal tissue. Of note, increased FDG uptake is not specific for malignant cells, but can also be seen in activated inflammatory cells (Yamada et al. 1995). While FDG-PET/CT is a mainstay of oncological hybrid imaging today, various other PET tracers are available for clinical use in disease states, where FDG uptake is not helpful in improving on the diagnosis of the patient.

PET/MR imaging is a promising recent development in hybrid imaging first introduced in 2010 (Delso et al. 2011). MRI provides multiparametric imaging and higher soft tissue contrast (than CT) potentially allowing to further improve the diagnostic accuracy and phenotyping of cancer. The recent data show that PET/MR imaging is feasible and performs at least equally well as PET/CT in most cancers (Spick et al. 2016). Based on the published literature bone metastases and prostate cancer are the areas where diagnostic advantages of PET/MR maybe achieved while disadvantages of PET/MR in comparison to PET/CT exist in lung nodule assessment (Spick et al. 2016).

1.5. Hybrid imaging of bone metastases

Bone metastases are a frequent site of distant spread of the cancer. Bone metastases can occur in up to 70% of patients with advanced breast or prostate cancer, and in up to 30% of patients with other advanced cancers (Roodman 2004). Non-invasive evaluation of the osseous tissue against the presence of bone metastases enables accurate staging and selection of the optimum treatment of oncological patient as well as prognosis determination.

Multiple imaging techniques can be used for the detection of the metastatic bone disease including MDP-WBS, CT, MR, PET/CT and PET/MR imaging (Choi and Raghavan 2012; Lecouvet et al. 2013; Eiber et al. 2014). The choice of the imaging strategy depends on the histologic type of the tumour. In breast cancer, in many centres currently the most commonly used methods for systemic staging are FDG-PET/CT or MDP-WBS with CT (Dashevsky et al. 2015). It has been shown that FDG-PET is more sensitive in the detection of lytic bone metastases whereas MDP-WBS is more sensitive in diagnosing sclerotic metastases (Cook et al. 1998; Uematsu et al. 2005; Huyge et al. 2009). In patients with prostate- (Even-Sapir et al. 2006) and breast cancers (Withofs et al. 2011) NaF-PET/CT has been shown to have superior sensitivity and specificity in comparison to MDP-WBS. In hybrid FDG-PET/CT imaging sensitivity in sclerotic bone metastases is increased due to detection of increased

bone density on CT images. However, in patients who received treatment, sclerotic lesions might indicate a treated lesion rather than an active metastasis. Additionally, histopathological verification of bone metastases is not always available. Adams and colleagues have evaluated the malignancy rate of bone lesions identified on FDG-PET/CT using CT-guided biopsy of suspicious lesions (Adams et al. 2016). They found that bone lesions showing FDG uptake exceeding mediastinal uptake yielded a PPV for malignancy of 89.2%, which was deemed not sufficiently high to justify changes in patient management without histopathological confirmation (Adams et al. 2016).

Whole-body MR imaging has been shown to have superior diagnostic accuracy compared with CT and bone scintigraphy in the detection of bone metastases because of its ability to assess early infiltration of bone marrow that precedes osteoblastic and osteoclastic response of the bone matrix to malignant tissue infiltration (Steinborn et al.; Engelhard et al. 2004; Mentzel et al. 2004; Yang et al. 2011; Lecouvet et al. 2013). Therefore the combination of FDG-PET with morphological information acquired by MR rather than CT may further increase the diagnostic accuracy of hybrid imaging. Some authors have reported that FDG-PET/MR was superior to FDG-PET/CT for anatomic delineation and allocation of bone lesions, and this finding may have clinical relevance in some clinical conditions (primary bone tumours, early bone marrow infiltration, and tumours with low uptake on PET) (Eiber et al. 2014). In another study the diagnostic performance of FDG-PET/MR versus PET/CT was evaluated in a small cohort of 10 patients with bone metastases from various primary tumours (Beiderwellen et al. 2014). Authors reported superior malignant lesion conspicuity in PET/MR compared to PET/CT without significant differences in lesion detection (Beiderwellen et al. 2014). In the most recent study performed in 109 patients with breast cancer higher sensitivity of contrast-enhanced FDG-PET/MR was reported in comparison to contrast enhanced FDG-PET/CT (Catalano et al. 2015). In particular, in this study multi-parametric FDG-PET/MR was positive for 12% of the patients deemed osseous metastasis-negative on the basis of contrast-enhanced PET-CT (Catalano et al. 2015).

While the ability of MR to assess infiltration of the bone marrow makes PET/MRI a promising modality in assessment of metastatic bone disease compared to PET/CT, currently available data is still limited and more evidence is highly anticipated to define the role of hybrid PET/MR in malignant bone disease. The use of multi-parametric MR protocols might provide a diagnostic advantage for PET/MR (Spick et al. 2016).

1.6. Resume

Current review of the literature points out the potential role of PET/MR in clinical management of patients with malignant disease and bone tissue involvement thanks to the ability of this method to image bone metabolism and morphology.

2. AIM OF THE STUDY

This doctoral thesis aims to improve the assessment of bone metabolism and morphology in patients with malignant disease using hybrid PET/MR imaging, providing enhanced support for diagnosis, treatment and prognosis evaluation.

In order to achieve this aim following tasks were set:

1) to achieve an accurate fusion of images acquired in stand-alone imaging systems. For this purpose a new dedicated patient transporter system was developed, and the registration accuracy of image fusion in a tri-modality PET/CT+MR system as well as a SPECT+D-CT system using this shuttle system was assessed.

2) to evaluate the need for accurate bone segmentation in MR based attenuation correction maps for whole body PET/MR imaging and to specifically look at tracer uptake quantification errors in bone lesions of various compositions and lesions close to bone.

3) to compare bone lesion detection, conspicuity and reader confidence of FDG-PET/MR and FDG-PET/CT in patients with FDG avid bone metastases.

3. MATERIALS AND METHODS

3.1. Multimodality image fusion using a newly developed PET/CT-MR and SPECT-CT patient shuttle system (Publication I)

A shuttle system was developed to sequentially integrate PET/CT and MR as well as SPECT/CT and diagnostic CT (D-CT) scanners. The purpose of the system was to produce 'hardware'-based fused images of the resulting PET, SPECT, D-CT and MR datasets. The system enabled the transfer of patients from one to the other scanning table without patient repositioning (**Publication I**). The patient was transferred between the scanners, while lying still on the shuttle board in a constant position. Therefore patient motion and postural changes between the scans on the two independent systems were minimized allowing instant fusion of the images. This avoided the need to use a special image registration software for correcting spatial offsets between images.

3.1.1. Patient transport/shuttle

A flexible side-loading shuttle prototype was developed and constructed in collaboration with a prototyping engineering company (Innovation Design Center, Thalwil, Switzerland). A side-loading shuttle system consisted of a metal trolley with counter balance weights (60 kg) on each side (orange) (Fig. 4). Two sliding 'arms' (coloured in red on image) hold a carbon or glass fibre board (coloured in blue on image) serving as a 'shuttle patient table', which can be slid either to the right or to the left of the shuttle system. This permits approaching and loading the patient onto a scanner table from either side. After sliding the board over the scanner table, the table is elevated until the board is entirely supported by it. Thereby, the board can be released from the arms, which are pulled back.

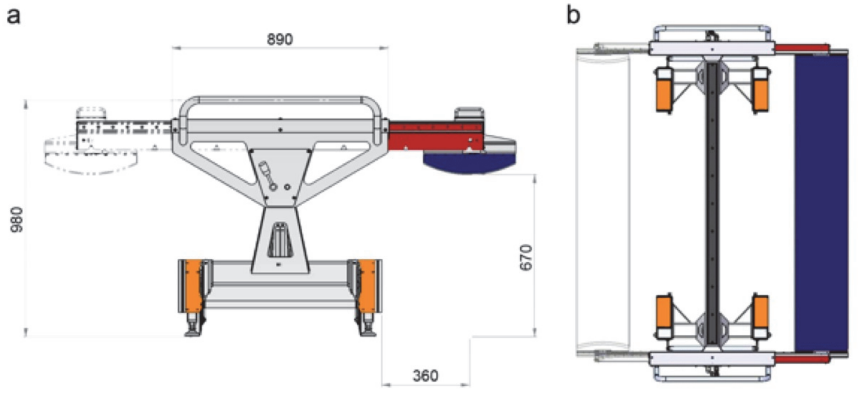

Fig 4. Schematic of the side-loading patient shuttle allowing the transport of the patient from one scanner to another.
Source: Samarin A, Kuhn FP, Brandsberg F, von Schulthess G, Burger IA. Image registration accuracy of an in-house developed patient transport system for PET/CT+MR and SPECT+CT imaging. Nucl Med Commun. 2015 Feb;36(2):194-200.

For SPECT/CT + D-CT integration, the patient transport board consisted of carbon fibre, whereas for the PET/CT + MR system integration, the transport board was built with fibre glass to minimize radio frequency attenuation effects. The MR scanner table was undocked and the patient was positioned on it outside the MR room as the current shuttle prototype was not built with MR-compatible materials. For the integration of MR with PET/CT, the shuttle system was designed such that MR surface coils could be installed and removed without moving the patient. Thus, surface coil-induced CT streak artefacts and PET attenuation artefacts could be avoided. Patient transfer time was around 10 min for both settings. No special, additional restraints were used to reduce patient motion.

The prerequisite for accurate fusion of the images originating from different scanners (e.g. PET/CT and MR, SPECT/CT and D-CT) was matching of scanners coordination systems. In case of sequential integration of PET/CT and MR it was a straightforward process as the gantry laser systems can be used successfully to match the coordinate systems of both scanners. For SPECT + D-CT fusion, fully automatic coregistration with matched coordinate systems was not possible as there is no laser patient positioning system for the SPECT/CT system used in the study (GE Hawkeye SPECT/CT system). Therefore for SPECT/CT and D-CT integration, the approach utilizing cobalt-57 registration markers (CoM) attached to the shuttle system was developed and used to match the coordinate systems (Fig 5).

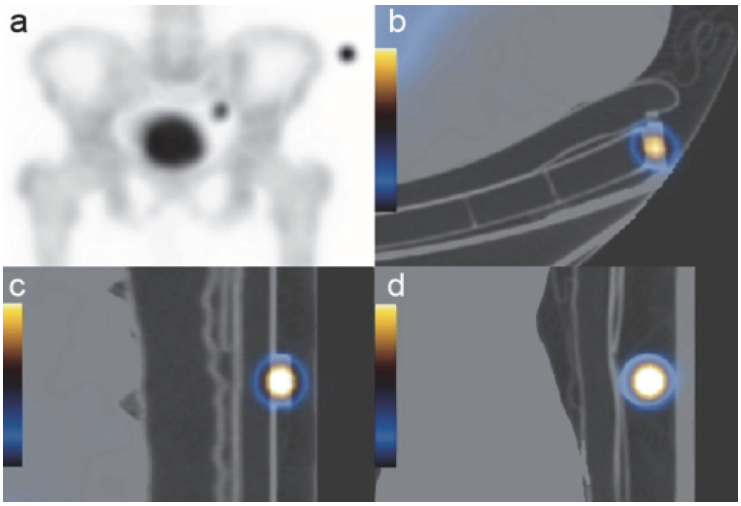

Fig. 5. Matching of the SPECT and D-CT images using the cobalt registration marker. (a) SPECT MIP of the pelvis with a cobalt-57 marker at the left lateral side of the carbon board. (b–d) Visual confirmation of accurate marker fusion in the fused SPECT + diagnostic CT (D-CT) images in (b) axial, (c) coronal and (d) sagittal views using the CoM.

Source: Samarin A, Kuhn FP, Brandsberg F, von Schulthess G, Burger IA. Image registration accuracy of an in-house developed patient transport system for PET/CT+MR and SPECT+CT imaging. Nucl Med Commun. 2015 Feb;36(2):194-200.

3.1.2. Assessment of image registration accuracy

For tri-modality PET/CT + MR imaging fusion, the matched coordinate system allowed fully automatic image fusion of the CT and MR data sets without any software-based or manual registration correction. The misalignment from the automatic registration was recorded as offsets in the X-axis (lateral), Y-axis (anterior-posterior) and Z-axis (cranio-caudal) between anatomical landmarks on CT and MRI. The magnitude of absolute displacement vector was calculated on the basis of the mean three-dimensional offsets. Anatomical landmarks least affected by respiratory motions and well depicted on both CT and MR images were selected: spine, pelvic bones and large paraspinal or pelvic muscles. For assessment of image registration accuracy thirty-one patients underwent sequential PET/CT + MR imaging. In each patient, at least six anatomical landmarks were selected manually: three in the bony structures and three in the large muscles.

For SPECT/CT + D-CT fusion cobalt markers attached to the shuttle table were used to align the coordinate systems and match SPECT and D-CT data with manual registration (Integrated Registration, Advantage Workstation 4.5; GE Healthcare). Attenuation correction CT (Ac-CT) data was acquired in the same imaging session as the SPECT data. The accuracy of CoM-assisted SPECT + D-CT image fusion was verified against the Ac-CT by matching the bony structures between D-CT and Ac-CT datasets. Three anatomical landmarks were selected for each patient. The offsets between the landmarks were recorded in the X-axis (lateral), Y-axis (anterior–posterior) and Z-axis (cranio-caudal). For assessment of image registration accuracy twelve patients underwent sequential SPECT + D-CT imaging. For each patient, the mean offset for the three landmarks was then calculated. The magnitude of the absolute displacement vector was calculated on the basis of the mean three-dimensional offsets.
The imaging setup described above was used in the following studies (**Publications II and III**).

3.2. Evaluation of the need for accurate bone segmentation in MR-based attenuation correction maps for whole-body PET/ MR imaging (Publication II).

Accurate attenuation correction is essential for quantitative analysis of PET tracer distribution. In conventional MR, the lack of cortical bone signal makes bone segmentation difficult and may require implementation of special sequences. In order to better understand the effects of bone attenuation using MR based AC, we undertook the following experiment. Artificial CT-based AC maps were created by segmenting all bony structures out of the CT images using a thresholding procedure. The thus identified bone regions were thereafter replaced with soft tissue densities. The AC-maps were then generated from these altered CT-data, and PET scans were reconstructed using the correct and

the altered CT-data. By subtraction of the thus generated two image data sets we finally generated whole-body error maps using CT data. These maps allowed us to visualize the areas of the body in which the resulting errors from ignoring bone in AC were substantial or only minimal.

3.2.1 Reconstruction of attenuation maps

Twenty two patients with osseous lesions and soft-tissue lesions adjacent to bone underwent sequential PET/CT and 3T MR imaging. In each patient standard and modified CT AC maps were generated from the regular and the "deboned" data sets as described above by a trilinear transformation of non-enhanced low-dose CT images to 511 keV PET attenuation maps (Burger et al. 2002). According to the performed histogram analysis of the CT images (Fig. 6) the density cut-off for the bone tissue segmentation was defined as 100 HU while the representative density value for the soft tissue was set at 36 HU.

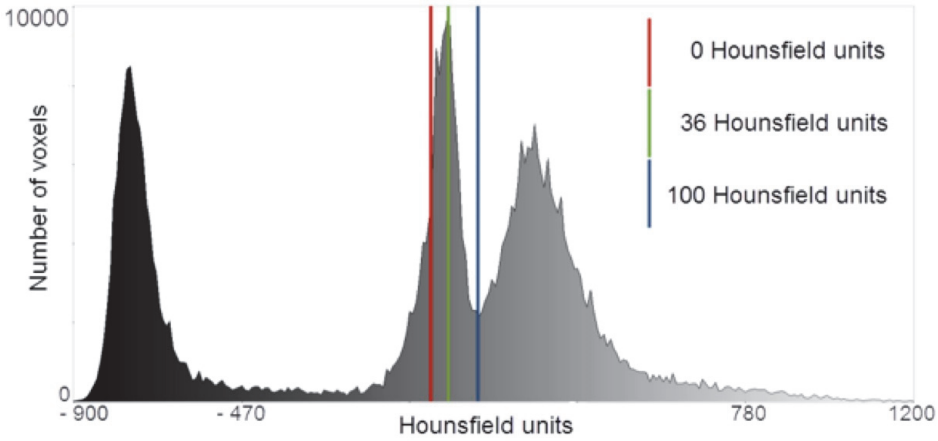

Fig. 6. Histogram analysis of CT images.
Source: Samarin A, Burger C, Wollenweber SD, Crook DW, Burger IA, Schmid DT, von Schulthess GK, Kuhn FP. PET/MR imaging of bone lesions – implications for PET quantification from imperfect attenuation correction. Eur J Nucl Med Mol Imaging. 2012 July;39:1154-1160

Modified AC maps (AC-Mod) were produced using PMOD software (PMOD Technologies, Zurich, Switzerland) by replacing pixels with values higher than 100 HU by pixels with a constant value of 36 HU, thereby simulating substitution of bone by soft tissue in MR-derived segmented AC maps. Standard AC maps (AC-St) were produced from the same but unmodified non-enhanced low-dose CT images. Hounsfield units were transformed into 511 keV attenuation using the following algorithm: AC [1/cm] = intercept + CT value * slope. CT values below 50 HU were converted to attenuation using the kVp-independent soft-tissue conversion with an intercept of 0.096 and a slope of 9.6×10^{-5}. CT values of 50 HU and above were converted using the 120-kVp

bone scale with an intercept of 0.0982 and a slope of 5.11×10^{-5}. Subsequently, two sets of attenuation-corrected PET images were reconstructed based on the modified and standard AC maps. An overview of the image reconstruction procedure is given in Fig. 7.

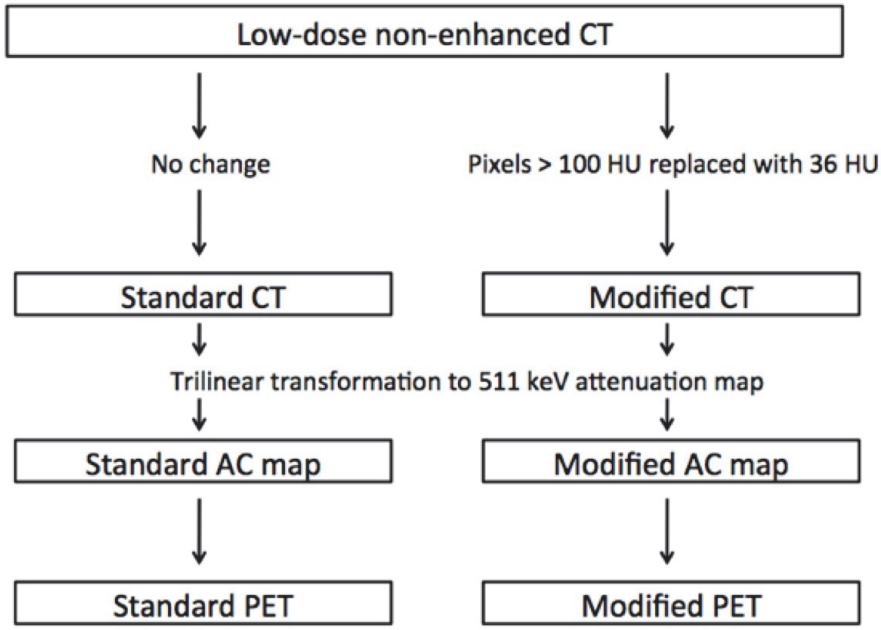

Fig. 7. Generation of AC maps followed by PET data reconstruction. The "no-bone" CT data were used for AC for modified PET images and compared to the PET images that were AC-corrected in standard mode.
Source: Samarin A, Burger C, Wollenweber SD, Crook DW, Burger IA, Schmid DT, von Schulthess GK, Kuhn FP. PET/MR imaging of bone lesions – implications for PET quantification from imperfect attenuation correction. Eur J Nucl Med Mol Imaging. 2012 July;39:1154-1160

3.2.2. Generation of a whole-body SUV error map

Whole-body maps showing the percentage differences in SUV between PET images reconstructed using the modified AC map ($PET_{AC\text{-}Mod}$) and the standard AC map ($PET_{AC\text{-}St}$) were generated using the following formula: $(PET_{AC\text{-}Mod} - PET_{AC\text{-}St}) / PET_{AC\text{-}St} \times 100\%$. The resulting difference map was analysed for body regions showing the largest differences in SUV.

3.2.3. Image analysis

The mean SUV of FDG avid lesions located in bone and in soft tissues adjacent to bone (within 10 mm) were measured by placing a volume of interest of 10 mm

diameter on PET_{AC-St} and PET_{AC-Mod} images. Subsequently, the standard error of SUVmean in the lesions was calculated for the PET_{AC-Mod} images using the PET_{AC-St} images as a reference.

Bone lesions were then divided into lesions involving spine, pelvic bones and other bones. Spine and pelvic lesions were further classified into three classes based on their appearance on CT images: (1) lytic lesions showing predominant and clearly visible destruction of osseous matrix with CT density below 100 HU, (2) sclerotic lesions showing predominantly increased bone density with CT density above 200 HU, and (3) lesions of mixed density showing a combination of destructive and sclerotic changes or lesions without visible change in bone density on CT images with a CT density in the range 100–200 HU.

3.3. Evaluation of clinical benefit of FDG-PET/MR in evaluation of bone metastases compared with FDG-PET/CT (Publication III).

The aim of this study was to investigate whether PET/MR provides an advantage compared with PET/CT for the detection and evaluation of bone metastases. For this purpose we compared detection, lesion conspicuity and reader confidence of FDG-PET/MR and FDG-PET/CT in patients with FDG avid bone metastases.

3.3.1. Patients and image acquisition

In this prospective study, 24 patients underwent sequential whole-body tri-modality FDG-PET/CT – MR imaging as a part of clinical work-up for either staging or restaging of various malignant tumours and suspicion of bone metastases (30 examinations). The primary diseases were breast cancer (12 patients), lung cancer (three patients), tonsil cancer (two patients), non-Hodgkin lymphoma (two patients) and carcinoma of the urethra, gastric cancer, cervical cancer, spindle cell skin cancer and medullary thyroid carcinoma (one patient each). Clinical indication for the PET/CT-examination was primary staging (10 exams) and restaging (20 exams). All patients had histological confirmation of their primary disease.

Sequential PET/CT and MR imaging was performed on a tri-modality PET/CT-MR set-up (full-ring, time-of- flight Discovery PET/CT 690 and a 3-T Discovery MR 750; both GE Healthcare, Waukesha, Wisconsin, USA). A dedicated shuttle board was used to transfer the patients from the MR table to the PET/CT table (**Publication I**). Patients fasted for at least 4 h before injection of a standard dose of an average of 4.5 MBq /kg body weight of FDG.

The MR imaging protocol consisted of whole-body multisection imaging using T1-weighted three-dimensional (3D) dual-echo gradient- recalled echo pulse sequence [liver accelerated volume acquisition (LAVA)-flex; GE Healthcare] and a coronally acquired short TI inversion recovery (STIR) sequence using parallel imaging. Additionally, a T2-weighted sequence with

motion correction [periodically rotated overlapping parallel lines with enhanced reconstruction (Propeller); GE Healthcare] was acquired using a breathing trigger in the thorax for enhanced breathing-triggered lung imaging. Low-dose CT data were acquired for PET attenuation correction and for diagnostic purposes. The PET data were acquired in 3D TOF mode with scan duration of 2 min per bed position, an overlap of bed positions of 23%, an axial FOV of 153 mm and a 700 mm diameter FOV.

3.3.2. Image analysis

Lesion detection

Up to ten PET-positive lesions were evaluated per patient with a maximum of three lesions per body compartment (e.g. cervical, thoracic, lumbar spine, pelvis). Lesions were considered PET positive if their maximum standardized uptake value (SUV_{max}) was higher than liver uptake.

Lesion conspicuity

The conspicuity of PET-positive bone lesions was evaluated on the corresponding PET/CT and PET/MR images. For this analysis, the conspicuity of the morphological imaging component was assessed (CT or MR). Lesions were assessed on the basis of a five-point scale: grade 0 – lesion was not detectable, grade 1 – 1–25% lesion contour detectable, grade 2 – 26–50% contour detectable, grade 3 – 51–75% contour detectable and grade 4 – 76–100% contour detectable.

Reader confidence

Reader confidence was determined qualitatively to evaluate if PET/CT or PET/MR was found more useful for the assessment of bone metastases under evaluation. The following score was used for assessment:

High reader confidence: FDG positive lesions had a morphologic correlate and overall hybrid imaging findings were deemed to be metastatic involvement – 2 points.

Moderate reader confidence: PET-positive findings were suggestive of metastatic disease but showed a questionable morphologic correlate – 1 point.

Low reader confidence: PET findings were inconclusive, no clear morphologic correlate was seen corresponding to the FDG-positive lesion – 0 points

4. RESULTS AND DISCUSSION

4.1. Registration accuracy of a newly developed PET/CT-MR and SPECT-CT patient shuttle system (Publication I)

For both PET/CT+MR and SPECT/CT+D-CT systems, the 'hardware' fusion of imaging data provided registration between datasets with small offsets, showing the feasibility of this sequential approach with a dedicated patient shuttle system.

The mean offset between CT and MR images for the PET/CT + MR setting was 8.1 ± 5.7 mm in the X-axis, 5.0 ± 4.0 mm in the Y-axis and 4.9 ± 5.6 mm in the Z-axis. The magnitude of the absolute displacement vector calculated on the basis of the mean three-dimensional off- sets was 10.7 mm.

The mean offset between anatomical landmarks on Ac-CT and D-CT in the SPECT + D-CT setting was 0.7 ± 0.8 mm in the X-axis, 2.1 ± 1.7 mm in the Y-axis and 0.8 ± 1.8 mm in the Z-axis. The magnitude of the absolute displacement vector calculated on the basis of the mean three-dimensional offsets was 2.4 mm.

In sequential integration of PET/CT and MR, the gantry laser systems can be used successfully to match the coordinate systems of both scanners. In the case of SPECT and D-CT integration, the approach utilizing cobalt sources attached to the shuttle system was developed and successfully used to match the coordinate systems. Although not used in our study, potentially, metal and oil-containing markers attached to the shuttle table can be developed to match the coordination systems of PET/CT and MR in a similar way as for the SPECT D-CT system to complement the scanner gantry laser systems. The present study focused on image fusion accuracy arising from patient motion as well as transportation and repositioning errors. It should be taken into account that respiratory motion can cause considerable registration errors between the PET, CT and MR data. Therefore, in this study, anatomical structures least affected by respiratory motion were used for the analysis of misalignment. Previously, only software-based image fusion data have been published for separate scanner systems like SPECT+D-CT (Grosu et al. 2005; Chowdhury and Scarsbrook 2008; Patel et al. 2009; Park et al. 2012; Vargas et al. 2013) or PET/CT+MR (Nakamoto et al. 2009; Kim et al. 2009; Donati et al. 2010). While the rigid structure of the skull ascertains that software fusion of brain structures is adequate, postural changes in the trunk and extremities may impair fusion accuracy (Kim et al. 2005).

Although fully integrated SPECT with high-end CT scanner systems (≥16 slices) are available, less busy services may opt to install shuttle systems between their nuclear cameras and a nearby D-CT to be more cost effective (von Schulthess and Burger 2010). The same could in fact be true for PET/MR implementations. Although fully integrated PET/MR have the advantage of simultaneous data acquisition without moving the patient or the table when imaging single FOVs, separate PET/CT and MR systems have the advantage of

full flexibility when placed in two separate rooms and might therefore be used more effectively. Furthermore, integrated 'hybrid' PET/MR systems are costly and may be beyond the financial reach for the many centres (von Schulthess and Burger 2010). A simple patient shuttle system could allow the integration of existing scanners to answer specific clinical questions without the need for costly investments.

4.2. Attenuation correction in bone lesions - implications for PET quantification in whole-body PET/ MR imaging (Publication II).

4.2.1. Whole-body error maps

Analysis of the whole-body error maps showed that ignoring bone tissue in AC maps resulted in substantial error in SUV quantification. Not surprisingly, the largest errors were present in bone. The errors are caused by an underestimation of the SUV, which is due to the fact, that the AC algorithm corrects the pixel counts corresponding to soft tissues with smaller attenuation numbers than those in bone. The magnitude of this error decreases rapidly with distance form bone and shows only a very small difference in other areas of the body with the exception of the brain. In addition to areas of underestimation, regions of slight overestimation of SUV were also identified in soft tissue on the SUV error maps, but not exceeding 5%. This is potentially due to differences caused by the interaction between changes in attenuation and the scatter correction of the data.

While all patients were scanned in a sequential PET/CT-MR system, for the generation of the SUV error maps, only original and modified CT data with bone replaced by soft tissue was used in order to determine the error in SUV. Areas in bone and next to bone showed marked errors on the map and therefore 191 lesions, 141 in bone and 50 adjacent to bone were examined in more detail.

4.2.2. SUV errors in bone lesions

Substitution of bone by soft tissue density values in AC maps resulted in a mean underestimation of SUV in all bone lesions of 11.2 ± 5.4%. A minimum SUV underestimation of 1.5% was seen in a rib lesion while a maximum SUV underestimation of 30.8% was identified in a sclerotic lesion located in the femoral bone. A summary of SUV errors in bone lesions of different composition in various regions produced by reconstruction of PET images using the modified AC maps is given in Table 1.

Table 1. Summary of SUV underestimation produced by reconstruction of PET images using modified attenuation correction maps.

Location	Number of lesions	Mean error ± SD (%)	Min error (%)	Max error (%)
SPINE, vertebral bodies				
sclerotic	23	15.9 ± 3.4	9.9	23.5
mixed density	13	10.6 ± 1.5	8.7	11.2
lytic	7	7.2 ± 1.7	4.9	9.3
PELVIC BONES				
sclerotic	17	14.2 ± 4	8.4	23.8
mixed density	15	13.1 ± 4.9	6.2	21.3
lytic	9	6.8 ± 2.7	3.1	12
Spine, vertebral processes	4	9.6 ± 3.8	4.9	13.9
Sacrum	11	8.6 ± 4.6	4.3	19.6
Sternum	7	8.5 ± 2.5	4.8	11.3
Ribs	10	3 ± 1	1.5	4.8
Scapula	3	7.7 ± 3.3	4.8	11.1
Humerus	11	8.4 ± 3	4	11
Femur	11	16.8 ± 7	9.5	30.8
TOTAL BONE LESIONS	141	11.2 ± 5.4	1.5	30.8
SOFT TISSUE LESIONS LOCATED NEAR BONE	50	3.2 ± 1.7	0.2	4

Source: Samarin A, Burger C, Wollenweber SD, Crook DW, Burger IA, Schmid DT, von Schulthess GK, Kuhn FP. PET/MR imaging of bone lesions – implications for PET quantification from imperfect attenuation correction. Eur J Nucl Med Mol Imaging. 2012 July;39:1154-1160

Compared to the studies performed by Martinez-Möller et al. (Martinez-Möller et al. 2009) (21 osseous lesions with an average SUV change of 8 ± 3% and maximal underestimation of 13.1% seen in a lesion in the pelvic bone) and by Schulz et al. (Schulz et al. 2011) (7 bone lesions with an average underestimation of 6.5 ± 4.1% and maximum error of −13.4% seen in a pelvic bone lesion), the average and maximum errors seen in osseous lesions were significantly higher in our study. We found the maximum SUV underestimation for bone lesions of more than 20% in dense sclerotic lesions: 23.5% for spine lesions, 23.8% for pelvic bone lesions and 30.8% for femoral lesions. The results of our study support the findings of Hofmann et al. which showed tracer uptake quantification errors of > 10% in 58% of osseous lesions and errors more than 20% in 22% of the lesions (Hofmann et al. 2011). The difference in the magnitude of

underestimation may be explained by the larger number of osseous lesions examined in our study (n=141), and their location and composition. Additionally, another important factor may be the different approaches to reconstruction of the AC maps as we substituted only bone by soft tissue values rather than using a full three- or four-class CT segmentation. This approach allowed us to determine the effect of bone attenuation by changing only one parameter.

The errors observed are of interest for understanding the systematic errors in MR AC-based PET scans, but are particularly relevant when comparing the data obtained from PET/CT and PET/MR for treatment response assessment. In fact, an AC-induced 20–30% error in SUV of a lesion might change the assessment of treatment response.

This was the first study showing a substantial difference in underestimation of SUV in PET between dense sclerotic and destructive lytic bone lesions when neglecting the bone in AC maps. The presence of 52 spine and 41 pelvic bone lesions allowed the assessment of the dependence of the error on the density of the bone lesions. A substantial difference in SUV underestimation was found between the sclerotic lesions with an average error of −15.9% in spine and −14.2% in pelvic lesions and lytic lesions with respective underestimation values of −7.2% and −6.8%. The commonly used approach to MR-based AC is tissue segmentation with substitution of bone by soft tissue values (Martinez-Möller et al. 2009; Schleyer et al. 2010; Eiber et al. 2011; Schulz et al. 2011; Hofmann et al. 2011). In bone lesions with little or no change in density over the therapeutic course, this type of segmentation will result only in a systematic under-correction of bone attenuation between consecutive PET/MR scans and interpretation is not truly affected. However, the density of the bone lesions can change significantly during the course of the disease—and this will have an impact on their attenuation properties. Treating bone as soft tissue in the MR AC maps of consecutive PET/MR scans performed for assessment of treatment response may result in SUV differences solely due to changes in lesion density and not due to a change in the metabolic activity of the lesion.

The magnitude of the SUV error of bone lesions is dependent not only on their own density but also on the density of the surrounding bones, being smaller in osteoporotic bones and larger in the presence of degenerative changes or in certain disease states (e.g. myelofibrosis, mastocytosis, osteopetrosis).

In summary, MR AC issues have a potential impact on the evaluation of bone disease in simultaneous PET/MRI, especially for assessing treatment response and comparing PET/MR to PET/CT data.

4.2.3. SUV errors in soft tissue lesions near the bone

A total of 50 FDG-positive lesions were identified in the soft tissues adjacent to bony structures in six patients. In these lesions, substitution of the bone by soft tissue values in the AC maps resulted in underestimation errors of 3.2 ± 1.7% (mean ± SD). Among these lesions, the smallest error of 0.2% was found in a lung lesion adjacent to a rib, while the largest error of 4% was seen in a lymph node adjacent to the osseous pelvis.

Such errors lower than 5% may be negligible for clinical purposes. While the data do not allow the relevance of skull bone for the AC of brain lesions to be addressed, other authors have shown that this is mandatory to quantify brain PET examinations (Catana et al. 2010).

In agreement with lesion-based evaluations of other studies (Martinez-Möller et al. 2009; Schulz et al. 2011), our AC maps suggest that for lesions in soft tissues, fat or lung, the omission of bone from the AC of PET data is clinically not relevant, at least at the levels of accuracy at which SUV values are used nowadays.

4.3. FDG-PET/MR increases diagnostic confidence in detection of bone metastases compared to FDG-PET/CT (Publication III).

A total of 86 FDG positive bone lesions were identified in 30 PET/CT and PET/MRI data sets performed in 24 patients. In 12 data sets, patients had multiple disseminated bone lesions, while in the remaining 18 data sets less than 10 lesions were present per patient. The metabolic and morphologic characteristics of the lesions are summarized in Table 2.

4.3.1. Detection of bone lesions

Overall, in both examinations, PET/CT and PET/MRI detected the same number of lesions based on the PET-component (since both examinations used the same PET-data set). In those 30 data sets, 95% of analyzed FDG positive bone lesions (82/86 lesions) had a morphologic correlate on the MR-component. Furthermore, on all PET/MRI examinations at least one morphological correlate was found on the MR-component. PET/CT imaging allowed identification of structural changes on the CT-component in 76% of the FDG positive lesions (65/86 lesions). A morphologic correlate on the CT component of the PET/CT was clearly identified in 23 PET/CT studies out of 30.

Overall, in seven examinations (7 patients), FDG-positive bone lesions (n=9) were seen only on the MR component while no clearly visible changes were noted in the bony structures on CT. In two of those examinations (2 patients), patients had one single FDG positive lesion that was neither visible on MR nor CT images. However, in both of these examinations a single additional FDG-positive bone lesion (2 lesions in total) were seen again only on MR in a different location. No additional lesions were seen on CT in those cases. The remaining lesions, which were FDG-positive but CT-negative, were all seen in patients where several other bone metastases were detected on both, the PET-component and the CT-component.

In two different examinations (2 patients), a structural bone change in two FDG positive lesions was noted only on CT but not on the MRI. Again, in those patients additional FDG positive bone lesions (4 lesions) showed a morphological correlate on MR.

The study performed suggests that one of the clinical scenarios where

PET/MRI may be beneficial over PET/CT, is an oncological patient with only few early bone metastases. In the series of patients evaluated in the current study, 25% of the lesions evaluated showed no definite morphological change of the bony structure on CT, while 95% of lesions had a clear morphological correlate on MR. Although all these lesions were still detected because of their FDG-avidity, in cases of low metabolic activity (e.g. post-therapy), moving artefacts and small size, a pathological FDG uptake in those lesions might not be very obvious. In this situation the clear depiction of lesions on the MR-component would ensure the detection of the lesions and correct distant staging of the disease. This observation is supported by the recent work of Eiber et al. who draw a similar conclusion (Eiber et al. 2014).

Table 2. Summary of metabolic and morphologic characteristics of all FDG positive bone lesions.

	N	Min	Max	Mean	SD
Metabolic characteristics					
SUVmax	86	2.2	29.7	7.96	5.2
SUVmean	86	1.2	14.2	4.6	2.69
TLG	86	477	441931	32243.91	77688.86
PETvol	86	0.42	83.8	5.74	12.1
Size, mm					
CT	65	4	84	17.03	16.77
MR T1 in-phase	82	5	85	20.63	17.2
Conspicuity, score					
CT	86	0	4	2.35	1.62
MR STIR	86	0	4	2.23	1.57
MR T1 water	86	0	4	2.48	1.42
MR T1 fat	86	0	4	3.09	1.44
MR T1 in-phase	86	0	4	2.21	1.46
MR T1 out-phase	86	0	4	2.76	1.47

Source: Samarin A, Hüllner M, Queiroz MA, Stolzmann P, Burger IA, von Schulthess G, Veit-Haibach P. 18F-FDG-PET/MR increases diagnostic confidence in detection of bone metastases compared with 18F-FDG-PET/CT. Nucl Med Commun. 2015 Dec; 36(12):1165-73

4.3.2. Lesion conspicuity

In lesion-by-lesion analysis of FDG-PET positive bone lesions, PET/MR imaging provided better results in detection of morphologic changes: the mean

lesion conspicuity was significantly better on T1 fat MR imaging compared to CT imaging (p=0.005, Table 3). The overall lesion conspicuity on STIR MR was similar to CT images.

Table 3. Comparison of lesions conspicuity scores between CT and MR images.

Lesions conspicuity	p-value
MR STIR versus CT	0.496
MR T1 water versus CT	0.516
MR T1 fat versus CT	0.005[a]
MR T1 in-phase versus CT	0.834
MR T1 out-phase versus CT	0.069

[a] - the mean lesion conspicuity was significantly higher on T1 fat MR imaging compared to CT imaging.
Source: Samarin A, Hüllner M, Queiroz MA, Stolzmann P, Burger IA, von Schulthess G, Veit-Haibach P. 18F-FDG-PET/MR increases diagnostic confidence in detection of bone metastases compared with 18F-FDG-PET/CT. Nucl Med Commun. 2015 Dec; 36(12):1165-73

In the sub-analysis based on lesions density (on the CT-component) the mean conspicuity of neither lytic nor sclerotic lesions was not significantly different on T1 fat MR imaging compared to CT imaging. However, the mean conspicuity of both sclerotic and lytic lesions was significantly higher on CT imaging compared to STIR MR imaging (p=0.014 and p=0.004, respectively). Further characteristics of this sub-analysis are summarized in Table 4.

Table 4. Conspicuity scores (mean values) of the lesions based on their CT density.

	Lytic	Sclerotic	Non-visible on CT
N of lesions (CT based)	48	17	21
CT score	3.08	3.18	0
MR STIR score	2.11	1.88	2.88
MR T1 water score	2.3	2.86	2.48
MR T1 fat score	2.77	3.37	3.52
MR T1 in-phase score	1.88	2.52	2.21
MR T1 out-phase score	2.53	3	3.05

Source: Samarin A, Hüllner M, Queiroz MA, Stolzmann P, Burger IA, von Schulthess G, Veit-Haibach P. 18F-FDG-PET/MR increases diagnostic confidence in detection of bone metastases compared with 18F-FDG-PET/CT. Nucl Med Commun. 2015 Dec; 36(12):1165-73

In the 21 FDG positive bone lesions without a corresponding structural change visible in PET/CT imaging (65/86 were seen), the lesions were seen best in T1 fat sequence of PET/MR imaging with a mean conspicuity of 3.52 and a mean size on T1 imaging of 19.5 mm. Further characteristics of these lesions are summarized in Table 5. The mean size of the FDG positive bone lesions was found to be significantly larger on T1 weighted MR images compared to CT images.

Table 5. Metabolic and morphologic characteristics (mean values) of FDG positive bone lesions non-visible on CT by location

	Thorax	Spine	Pelvis	Extremities	Total
N	2	7	6	6	21
Metabolic characteristics					
SUVmax	4.6	7.4	17.6	7,8	10.1
SUVmean	2.2	4.3	8.3	4.9	5.4
Size, mm					
MR T1 in-phase	17	18.3	28.5	13.7	19.5
Conspicuity, score					
MR STIR	1	2.3	3.7	3.7	2.9
MR T1 water	1	3.1	3.3	2.7	2.9
MR T1 fat	1	3.9	3	3.3	3.5
MR T1 in-phase	1	2.9	3	2.2	2.5
MR T1 out-phase	1	3.3	3.7	2.8	3.1

Source: Samarin A, Hüllner M, Queiroz MA, Stolzmann P, Burger IA, von Schulthess G, Veit-Haibach P. 18F-FDG-PET/MR increases diagnostic confidence in detection of bone metastases compared with 18F-FDG-PET/CT. Nucl Med Commun. 2015 Dec; 36(12):1165-73

Overall, improved lesion conspicuity was found in the current study in evaluation of PET/MRI compared to PET/CT. The lesion-by-lesion analysis revealed that the highest lesion conspicuity was achieved by PET/MR imaging using a T1 weighted sequence highlighting the alterations in the bone marrow (T1 fat reconstruction). The significant increase in lesion conspicuity on MR imaging was mainly due to 21 FDG positive bone lesions not visible on CT imaging. These lesions likely represent bone marrow infiltration that have not yet resulted in substantial changes in bone density, but already resulted in MR signal alterations (Choi and Raghavan 2012). Interestingly, the mean size of these lesions was quite large (19.5 mm). These results are partly in line with a recent study with a similar number of evaluated lesions (Eiber et al. 2014).

There, PET/MRI with a T1w- sequence in addition to the Dixon-based attenuation correction sequence was superior in lesion delineation. Several differences have to be noted compared to the current study. One of the reasons for the improved delineation in this additional T1w sequence might be the higher matrix compared to the Dixon sequence. However, overall detection was not significantly different. Additional differences are that the PET/CT was partly done with contrast media compared to a non-contrast PET/MRI. In the current study, strictly non-contrast PET/CT was used for comparison with PET/MR.

The presence of FDG-positive bone lesions on PET with negative findings at CT is not uncommon and a known clinical issue. In the study of Taira et al. 27% (31 out of 113) of analysed FDG-positive bone lesions were found to be CT-negative (Taira et al. 2007). Additionally, MRI has been shown to find metastasis not visible on FDG-PET or CT imaging (Ghanem et al. 2007). In an early comparison, Antoch et al. reported that MRI was more accurate in evaluating the bone structure for the presence of metastasis in a study comparing the staging accuracies of whole-body MRI and PET/CT (Antoch et al. 2003). These finding were later supported by a study of Schmidt and co-workers where whole-body MR imaging was found to have superior sensitivity and accuracy compared to PET/CT in detection of bone metastases (Schmidt et al. 2007). Therefore, in PET/MRI even in cases of low FDG-activity, the likelihood of correct detection and staging seems to be higher than PET/CT. On the other hand, according to the results of our study, in patients with a high likelihood of metastatic bone disease, the use of PET/MRI would likely not result in improved diagnostic confidence, as both PET/CT and PET/MRI would detect multiple lesions with no further therapeutic consequence.

Interestingly, in the patient population of the current study the mean conspicuity of neither lytic nor sclerotic lesions was significantly different on T1 imaging compared to CT- density. However, there was a difference of sclerotic and lytic lesions compared to STIR. This is remarkable, because usually in MR-imaging fat-saturated T2 imaging is being considered the ideal sequence to search for the major pathologies and especially bone lesions (Vanel et al. 2000; Vanel et al. 2009). In PET/MRI (or PET/CT-MRI) the PET-component is always available (no choice) but one has a choice which sequences are being used in the MR-part of the examination. In fact, in order to minimize imaging time, one has to strive to use the minimal number of MR pulse sequences in PET/MR. Thus, in the context of PET/MR, the sequences of choice might be different to those used MR-imaging alone.

4.3.3. Reader confidence in diagnosing bone metastases

The overall reader confidence based on the above mentioned scale for PET/CT was 1.76 and 2.0 for PET/MRI ($p=0.0029$). PET/MR showed a high confidence in all patients. In PET/CT a high confidence was found in 23 cases and a moderate confidence in 7 cases. In 23 studies no difference of reader confidence

was observed between PET/CT and PET/MR imaging. These patients either had several lesions seen on both modalities or had multiple disseminated lesions where the difference in detection of single lesions didn't lead to change of overall reader confidence. Thus, in the seven studies in which all FDG-positive bone lesions (n=9) were seen only on the MR component, a significant increase was found concerning reader confidence for PET/MRI vs. PET/CT.

Although overall lesion detection was the same on PET/CT and PET/MRI, the additionally detected lesions on the MRI-component obviously support the diagnostic confidence for the reader – a fact not neglectable in clinical routine reading, again, and this is particularly true, when lesions exhibit low FDG-uptake.

In summary, in this study the overall detection rate of PET/CT and PET/MRI was the same, based on the FDG-positivity of the evaluated bone metastases. However, we could demonstrate that the lesion conspicuity as well as the reader confidence was improved in PET/MRI compared to PET/CT based on the soft tissue contrast of the MR-component. Furthermore, several morphological correlates were identified in PET/MRI that were not present in PET/CT.

5. CONCLUSIONS

The main results of the current study were as follows:

1). Sequential PET/CT + MR imaging using a newly developed dedicated patient shuttle system is feasible, resulting in clinically acceptable offsets between data sets using the gantry laser systems. Therefore in the absence of a fully integrated PET/MR system, sequential connection of the available standalone PET/CT and MR scanners allows achievement of benefits of hybrid PET/MR imaging in the daily clinical setting.

2). Treating bone as soft tissue in simulated MR-derived attenuation correction maps for PET/ MR leads to a substantial underestimation of SUV values in bone lesions. The errors depend substantially on lesion composition, with the largest error being seen in sclerotic lesions. Thus in fully integrated PET/MR systems depiction of the cortical bone and sclerotic areas in MR-based attenuation correction maps is essential for accurate quantification of tracer uptake values in bone lesions.

3). FDG-PET/MRI offers higher reader confidence and improved conspicuity in bone metastases compared with FDG-PET/CT.
The analysis of FDG avid bone metastases showed that the highest lesion conspicuity was achieved by FDG-PET/MR imaging using a T1-weighted MR sequence highlighting the alterations in the bone marrow: the mean lesion conspicuity was significantly better on T1 fat reconstruction MR imaging compared with CT imaging. The significant increase in lesion conspicuity on MR imaging was mainly because of multiple FDG-positive bone lesions not visible on CT imaging. In studies in which all FDG-positive bone lesions were seen only on the MR component, a significant increase was found in reader confidence for PET/MRI versus PET/CT.

Finally, the results of this doctoral study support the use of PET/MR for imaging of bone metabolism and morphology in patients with malignant disease. In fully integrated PET/MR systems, segmentation of the bone tissue in MR-based attenuation correction maps is a prerequisite for quantitative hybrid imaging.

REFERENCES

Adams HJA, de Klerk JMH, Heggelman BGF, et al (2016) Malignancy rate of biopsied suspicious bone lesions identified on FDG PET/CT. Eur J Nucl Med Mol Imaging. doi: 10.1007/s00259-015-3282-4

Akbarzadeh A, Ay MR, Ahmadian A, et al (2013) MRI-guided attenuation correction in whole-body PET/MR: assessment of the effect of bone attenuation. Ann Nucl Med 27:152–62. doi: 10.1007/s12149-012-0667-3

Antoch G, Saoudi N, Kuehl H, et al (2004) Accuracy of whole-body dual-modality fluorine-18-2-fluoro-2-deoxy-D-glucose positron emission tomography and computed tomography (FDG-PET/CT) for tumor staging in solid tumors: comparison with CT and PET. J Clin Oncol 22:4357–68. doi: 10.1200/JCO.2004.08.120

Antoch G, Vogt FM, Freudenberg LS, et al (2003) Whole-body dual-modality PET/CT and whole-body MRI for tumor staging in oncology. JAMA 290:3199–206. doi: 10.1001/jama.290.24.3199

Attenberger U, Catana C, Chandarana H, et al (2015) Whole-body FDG PET-MR oncologic imaging: pitfalls in clinical interpretation related to inaccurate MR-based attenuation correction. Abdom Imaging 40:1374–1386. doi: 10.1007/s00261-015-0455-3

Aznar MC, Sersar R, Saabye J, et al (2014) Whole-body PET/MRI: The effect of bone attenuation during MR-based attenuation correction in oncology imaging. Eur J Radiol 83:1177–1183. doi: 10.1016/j.ejrad.2014.03.022

Beiderwellen K, Huebner M, Heusch P, et al (2014) Whole-body [^{18}F]FDG PET/MRI vs. PET/CT in the assessment of bone lesions in oncological patients: initial results. Eur Radiol 24:2023–30. doi: 10.1007/s00330-014-3229-3

Beyer T, Lassen ML, Boellaard R, et al (2016) Investigating the state-of-the-art in whole-body MR-based attenuation correction: an intra-individual, inter-system, inventory study on three clinical PET/MR systems. MAGMA. doi: 10.1007/s10334-015-0505-4

Beyer T, Townsend DW, Brun T, et al (2000) A combined PET/CT scanner for clinical oncology. J Nucl Med 41:1369–1379.

Beyer T, Weigert M, Quick HH, et al (2008) MR-based attenuation correction for torso-PET/MR imaging: pitfalls in mapping MR to CT data. Eur J Nucl Med Mol Imaging 35:1142–6. doi: 10.1007/s00259-008-0734-0

Boellaard R, Quick HH (2015) Current image acquisition options in PET/MR. Semin Nucl Med 45:192–200. doi: 10.1053/j.semnuclmed.2014.12.001

Burger C, Goerres G, Schoenes S, et al (2002) PET attenuation coefficients from CT images: experimental evaluation of the transformation of CT into PET 511-keV attenuation coefficients. Eur J Nucl Med Mol Imaging 29:922–7. doi: 10.1007/s00259-002-0796-3

Catalano OA, Nicolai E, Rosen BR, et al (2015) Comparison of CE-FDG-PET/CT with CE-FDG-PET/MR in the evaluation of osseous metastases in breast cancer patients. Br J Cancer 112:1452–60. doi:

10.1038/bjc.2015.112
Catana C, van der Kouwe A, Benner T, et al (2010) Toward implementing an MRI-based PET attenuation-correction method for neurologic studies on the MR-PET brain prototype. J Nucl Med 51:1431–8. doi: 10.2967/jnumed.109.069112
Choi J, Raghavan M (2012) Diagnostic imaging and image-guided therapy of skeletal metastases. Cancer Control 19:102–12.
Chowdhury FU, Scarsbrook AF (2008) The role of hybrid SPECT-CT in oncology: current and emerging clinical applications. Clin Radiol 63:241–51. doi: 10.1016/j.crad.2007.11.008
Collins FS, Varmus H (2015) A New Initiative on Precision Medicine. N Engl J Med 372:793–5. doi: 10.1056/NEJMp1500523
Cook GJ, Houston S, Rubens R, et al (1998) Detection of bone metastases in breast cancer by 18FDG PET: differing metabolic activity in osteoblastic and osteolytic lesions. J Clin Oncol 16:3375–9.
Dashevsky BZ, Goldman DA, Parsons M, et al (2015) Appearance of untreated bone metastases from breast cancer on FDG PET/CT: importance of histologic subtype. Eur J Nucl Med Mol Imaging 42:1666–73. doi: 10.1007/s00259-015-3080-z
Delso G, Fürst S, Jakoby B, et al (2011) Performance measurements of the Siemens mMR integrated whole-body PET/MR scanner. J Nucl Med 52:1914–22. doi: 10.2967/jnumed.111.092726
Delso G, ter Voert E, Veit-Haibach P (2015) How does PET/MR work? Basic physics for physicians. Abdom Imaging 1352–1357. doi: 10.1007/s00261-015-0437-5
Donati OF, Hany TF, Reiner CS, et al (2010) Value of retrospective fusion of PET and MR images in detection of hepatic metastases: comparison with 18F-FDG PET/CT and Gd-EOB-DTPA-enhanced MRI. J Nucl Med 51:692–9. doi: 10.2967/jnumed.109.068510
Eiber M, Martinez-Möller A, Souvatzoglou M, et al (2011) Value of a Dixon-based MR/PET attenuation correction sequence for the localization and evaluation of PET-positive lesions. Eur J Nucl Med Mol Imaging 38:1691–701. doi: 10.1007/s00259-011-1842-9
Eiber M, Takei T, Souvatzoglou M, et al (2014) Performance of Whole-Body Integrated 18F-FDG PET/MR in Comparison to PET/CT for Evaluation of Malignant Bone Lesions. J Nucl Med 55:191–7. doi: 10.2967/jnumed.113.123646
Engelhard K, Hollenbach HP, Wohlfart K, et al (2004) Comparison of whole-body MRI with automatic moving table technique and bone scintigraphy for screening for bone metastases in patients with breast cancer. Eur Radiol 14:99–105. doi: 10.1007/s00330-003-1968-7
Even-Sapir E, Metser U, Mishani E, et al (2006) The detection of bone metastases in patients with high-risk prostate cancer: 99mTc-MDP Planar bone scintigraphy, single- and multi-field-of-view SPECT, 18F-fluoride PET, and 18F-fluoride PET/CT. J Nucl Med 47:287–97.

Ghanem NA, Pache G, Lohrmann C, et al (2007) MRI and (18)FDG-PET in the assessment of bone marrow infiltration of the spine in cancer patients. Eur Spine J 16:1907–12. doi: 10.1007/s00586-007-0350-x

Grosu AL, Weber WA, Franz M, et al (2005) Reirradiation of recurrent high-grade gliomas using amino acid PET (SPECT)/CT/MRI image fusion to determine gross tumor volume for stereotactic fractionated radiotherapy. Int J Radiat Oncol Biol Phys 63:511–9. doi: 10.1016/j.ijrobp.2005.01.056

Hillner BE, Siegel BA, Liu D, et al (2008) Impact of positron emission tomography/computed tomography and positron emission tomography (PET) alone on expected management of patients with cancer: initial results from the National Oncologic PET Registry. J Clin Oncol 26:2155–61. doi: 10.1200/JCO.2007.14.5631

Hofmann M, Bezrukov I, Mantlik F, et al (2011) MRI-based attenuation correction for whole-body PET/MRI: quantitative evaluation of segmentation- and atlas-based methods. J Nucl Med 52:1392–9. doi: 10.2967/jnumed.110.078949

Hofmann M, Pichler B, Schölkopf B, Beyer T (2009) Towards quantitative PET/MRI: a review of MR-based attenuation correction techniques. Eur J Nucl Med Mol Imaging 36 Suppl 1:S93–104. doi: 10.1007/s00259-008-1007-7

Hofmann M, Steinke F, Scheel V, et al (2008) MRI-based attenuation correction for PET/MRI: a novel approach combining pattern recognition and atlas registration. J Nucl Med 49:1875–83. doi: 10.2967/jnumed.107.049353

Huyge V, Garcia C, Vanderstappen A, et al (2009) Progressive osteoblastic bone metastases in breast cancer negative on FDG-PET. Clin Nucl Med 34:417–20. doi: 10.1097/RLU.0b013e3181a7d03c

Keereman V, Fierens Y, Broux T, et al (2010) MRI-based attenuation correction for PET/MRI using ultrashort echo time sequences. J Nucl Med 51:812–8. doi: 10.2967/jnumed.109.065425

Kim J-H, Czernin J, Allen-Auerbach MS, et al (2005) Comparison between 18F-FDG PET, in-line PET/CT, and software fusion for restaging of recurrent colorectal cancer. J Nucl Med 46:587–95.

Kim S-K, Choi HJ, Park S-Y, et al (2009) Additional value of MR/PET fusion compared with PET/CT in the detection of lymph node metastases in cervical cancer patients. Eur J Cancer 45:2103–9. doi: 10.1016/j.ejca.2009.04.006

Kinahan PE, Hasegawa BH, Beyer T (2003) X-ray-based attenuation correction for positron emission tomography/computed tomography scanners. Semin Nucl Med 33:166–179. doi: 10.1053/snuc.2003.127307

Kinahan PE, Townsend DW, Beyer T, Sashin D (1998) Attenuation correction for a combined 3D PET/CT scanner. Med Phys 25:2046–53.

Lardinois D, Weder W, Hany TF, et al (2003) Staging of non-small-cell lung cancer with integrated positron-emission tomography and computed tomography. N Engl J Med 348:2500–7. doi: 10.1056/NEJMoa022136

Larsson A, Johansson A, Axelsson J, et al (2013) Evaluation of an attenuation

correction method for PET/MR imaging of the head based on substitute CT images. MAGMA 26:127–36. doi: 10.1007/s10334-012-0339-2
Lecouvet FE, Larbi A, Pasoglou V, et al (2013) MRI for response assessment in metastatic bone disease. Eur Radiol 23:1986–97. doi: 10.1007/s00330-013-2792-3
Leiblich A, Stevens D, Sooriakumaran P (2016) The Utility of Molecular Imaging in Prostate Cancer. Curr Urol Rep 17:26. doi: 10.1007/s11934-015-0573-z
Martinez-Möller A, Souvatzoglou M, Delso G, et al (2009) Tissue classification as a potential approach for attenuation correction in whole-body PET/MRI: evaluation with PET/CT data. J Nucl Med 50:520–6. doi: 10.2967/jnumed.108.054726
Mentzel H-J, Kentouche K, Sauner D, et al (2004) Comparison of whole-body STIR-MRI and 99mTc-methylene-diphosphonate scintigraphy in children with suspected multifocal bone lesions. Eur Radiol 14:2297–302. doi: 10.1007/s00330-004-2390-5
Miglioretti DL, Johnson E, Williams A, et al (2013) The use of computed tomography in pediatrics and the associated radiation exposure and estimated cancer risk. JAMA Pediatr 167:700–7. doi: 10.1001/jamapediatrics.2013.311
Nakamoto Y, Tamai K, Saga T, et al (2009) Clinical value of image fusion from MR and PET in patients with head and neck cancer. Mol Imaging Biol 11:46–53. doi: 10.1007/s11307-008-0168-x
O'Sullivan GJ, Carty FL, Cronin CG (2015) Imaging of bone metastasis: An update. World J Radiol 7:202–11. doi: 10.4329/wjr.v7.i8.202
Park H, Wood D, Hussain H, et al (2012) Introducing parametric fusion PET/MRI of primary prostate cancer. J Nucl Med 53:546–51. doi: 10.2967/jnumed.111.091421
Patel CN, Chowdhury FU, Scarsbrook AF (2009) Hybrid SPECT/CT: the end of 'unclear' medicine. Postgrad Med J 85:606–13. doi: 10.1136/pgmj.2008.077859
Pichler BJ, Judenhofer MS, Catana C, et al (2006) Performance test of an LSO-APD detector in a 7-T MRI scanner for simultaneous PET/MRI. J Nucl Med 47:639–47.
Prasad V, Fojo T, Brada M (2016) Precision oncology: origins, optimism, and potential. Lancet Oncol 17:e81–6. doi: 10.1016/S1470-2045(15)00620-8
Robson MD, Bydder GM (2006) Clinical ultrashort echo time imaging of bone and other connective tissues. NMR Biomed 19:765–80. doi: 10.1002/nbm.1100
Roodman GD (2004) Mechanisms of bone metastasis. N Engl J Med 350:1655–64. doi: 10.1056/NEJMra030831
Schleyer PJ, Schaeffter T, Marsden PK (2010) The effect of inaccurate bone attenuation coefficient and segmentation on reconstructed PET images. Nucl Med Commun 31:708–16. doi: 10.1097/MNM.0b013e32833b0573
Schmidt GP, Schoenberg SO, Schmid R, et al (2007) Screening for bone

metastases: whole-body MRI using a 32-channel system versus dual-modality PET-CT. Eur Radiol 17:939–49. doi: 10.1007/s00330-006-0361-8

Schöder H, Larson SM, Yeung HWD (2004) PET/CT in oncology: integration into clinical management of lymphoma, melanoma, and gastrointestinal malignancies. J Nucl Med 45 Suppl 1:72S–81S.

Schraml C, Schmid M, Gatidis S, et al (2015) Multiparametric analysis of bone marrow in cancer patients using simultaneous PET/MR imaging: Correlation of fat fraction, diffusivity, metabolic activity, and anthropometric data. J Magn Reson Imaging n/a–n/a. doi: 10.1002/jmri.24865

Schulz V, Torres-Espallardo I, Renisch S, et al (2011) Automatic, three-segment, MR-based attenuation correction for whole-body PET/MR data. Eur J Nucl Med Mol Imaging 38:138–52. doi: 10.1007/s00259-010-1603-1

Shah SN, Huang SS (2015) Hybrid PET/MR imaging: physics and technical considerations. Abdom Imaging 40:1358–1365. doi: 10.1007/s00261-015-0443-7

Som P, Atkins HL, Bandoypadhyay D, et al (1980) A fluorinated glucose analog, 2-fluoro-2-deoxy-D-glucose (F-18): nontoxic tracer for rapid tumor detection. J Nucl Med 21:670–5.

Spick C, Herrmann K, Czernin J (2016) 18F-FDG PET/CT and PET/MRI perform equally well in cancer patients: Evidence from studies in more than 2300 patients. J Nucl Med. doi: 10.2967/jnumed.115.158808

Steinborn MM, Heuck AF, Tiling R, et al Whole-body bone marrow MRI in patients with metastatic disease to the skeletal system. J Comput Assist Tomogr 23:123–9.

Taira A V, Herfkens RJ, Gambhir SS, Quon A (2007) Detection of bone metastases: assessment of integrated FDG PET/CT imaging. Radiology 243:204–11. doi: 10.1148/radiol.2431052104

Townsend DW, Beyer T, Blodgett TM (2003) PET/CT scanners: A hardware approach to image fusion. Semin Nucl Med 33:193–204. doi: 10.1053/snuc.2003.127314

Uematsu T, Yuen S, Yukisawa S, et al (2005) Comparison of FDG PET and SPECT for detection of bone metastases in breast cancer. AJR Am J Roentgenol 184:1266–73. doi: 10.2214/ajr.184.4.01841266

Vanel D, Casadei R, Alberghini M, et al (2009) MR imaging of bone metastases and choice of sequence: spin echo, in-phase gradient echo, diffusion, and contrast medium. Semin Musculoskelet Radiol 13:97–103. doi: 10.1055/s-0029-1220880

Vanel D, Dromain C, Tardivon A (2000) MRI of bone marrow disorders. Eur Radiol 10:224–9. doi: 10.1007/s003300050038

Vargas HA, Burger IA, Donati OF, et al (2013) Magnetic resonance imaging/positron emission tomography provides a roadmap for surgical planning and serves as a predictive biomarker in patients with recurrent

gynecological cancers undergoing pelvic exenteration. Int J Gynecol Cancer 23:1512–9. doi: 10.1097/IGC.0b013e3182a41e61

von Schulthess GK, Burger C (2010) Integrating imaging modalities: what makes sense from a workflow perspective? Eur J Nucl Med Mol Imaging 37:980–90. doi: 10.1007/s00259-009-1378-4

Von Schulthess GK, Schlemmer HPW (2009) A look ahead: PET/MR versus PET/CT. Eur J Nucl Med Mol Imaging 36:3–9. doi: 10.1007/s00259-008-0940-9

Wehrl HF, Sauter AW, Divine MR, Pichler BJ (2015) Combined PET/MR: A Technology Becomes Mature. J Nucl Med 56:165–168. doi: 10.2967/jnumed.114.150318

Withofs N, Grayet B, Tancredi T, et al (2011) ^{18}F-fluoride PET/CT for assessing bone involvement in prostate and breast cancers. Nucl Med Commun 32:168–76. doi: 10.1097/MNM.0b013e3283412ef5

Woolf DK, Padhani a R, Makris A (2015) Assessing response to treatment of bone metastases from breast cancer: what should be the standard of care? Ann Oncol 26:1048–57. doi: 10.1093/annonc/mdu558

Yamada S, Kubota K, Kubota R, et al (1995) High accumulation of fluorine-18-fluorodeoxyglucose in turpentine-induced inflammatory tissue. J Nucl Med 36:1301–6.

Yang H-L, Liu T, Wang X-M, et al (2011) Diagnosis of bone metastases: a meta-analysis comparing ^{18}FDG PET, CT, MRI and bone scintigraphy. Eur Radiol 21:2604–17. doi: 10.1007/s00330-011-2221-4

Acknowledgements

I would like to sincerely thank everyone who contributed to my doctoral study and made this thesis possible.

I would like to express my deepest gratitude to Professor Sergei Nazarenko, my mentor and supervisor, for facilitating entering a scientific track for me, creation of the unique possibilities for professional development and providing invaluable guidance in the scientific world.

I am sincerely thankful to Professor Gustav von Schulthess, my supervisor, for providing me an outstanding opportunity for joining the Zurich University Hospital research team, for his continuous generous help and support in research activities and visionary discussions on the topic of hybrid imaging. I appreciate the time and inspiring positive support from Dr. Patrick Veit-Haibach, Dr. Irene Burger, Dr. Cyrill Burger and the whole "family" of Department of Nuclear Medicine at the Zurich University Hospital.

I would like to thank Professors Kalju Meigas, Ivo Fridolin and Hiie Hinrikus for their guidance and support.

I would like to appreciate the support from Dr. Maret Talk for establishing fruitful conditions for research activities in the department. My special thanks go to Dr. Ruth Brand, Dr. Liina Karusoo and all my good colleagues from Department of Radiology at North Estonia Medical Centre who did all the clinical work while I was involved in the research activities.

Most importantly, I would like to thank my parents Galina and Aleksei for their exceptional love, care and support. I am grateful to my brother Aleksandr for taking care of me and being such a great example. I express my sincere thanks to my wife Jevgenia and son Arthur for inspiring me every day.

ABSTRACT

Hybrid PET/MR imaging of bone metabolism and morphology

Recent developments of imaging technologies point out the potential role of PET/MRI in the clinical management of patients with malignant disease and bone tissue involvement, thanks to the ability of this method to image bone metabolism and morphology together. There are a number of technological issues which have to be solved in order to achieve clinical usefulness of PET/MRI. Current work deals with three major aspects of this development: co-registration of three cardinal 3D imaging techniques (PET, CT and MRI), assessment of photon attenuation correction in the human body, and clinical comparison of PET/CT and PET/MRI based hybrid imaging of bone metabolism and morphology.

In the current study a tri-modality PET/CT-MRI setup was used as a platform to investigate the need for accurate bone segmentation in MR based PET attenuation correction maps and for the assessment of the potential clinical utility of PET/MRI in patients with metastatic bone disease. The patient shuttle system developed and described allowed robust transfer of the patients between PET/CT and MR scanners resulting in "hardware-based" fusion of the PET and MR datasets.

In order to better understand the effects of bone attenuation in a MR based PET AC approach lacking bone segmentation, whole-body SUV error maps were generated using original and modified "no-bone" CT AC data. This approach allowed the visualization of the areas of the body in which the resulting errors from ignoring bone in AC were substantial or only minimal. For evaluation of the potential clinical benefit of FDG-PET/MRI in bone imaging compared to FDG-PET/CT, detection and assessment of FDG avid bone metastases by both techniques was performed.

The study showed that neglecting bone in simulated MR based AC for whole-body PET can lead to substantial underestimation of tracer uptake in bone lesions depending on location and lesion composition. Therefore accurate quantification of tracer uptake values in PET/MR imaging requires application of MR sequences that are able to depict bone and calcified areas.

Hybrid FDG-PET/MRI achieved higher reader confidence and improved conspicuity of bone metastases compared to FDG-PET/CT imaging. MR imaging allowed improved visualization of the morphologic correlates of metabolically active bone lesions detected on FDG-PET images compared with CT imaging. This finding supports the use of PET/MRI for assessment of bone marrow infiltration in patients with oncological diseases.

Results of this doctoral study support the use of PET/MRI as a precision medicine tool for imaging of bone metabolism and morphology in patients with malignant disease. In fully integrated PET/MR systems segmentation of the bone tissue in MR-based attenuation correction maps is a prerequisite for quantitative hybrid imaging.

KOKKUVÕTE

Luustiku ainevahetuse ja morfoloogia hübriidkuvamine positronemissioontomograafia ja magnetresonantstomograafia abil

Kuvamistehnikate äsjased arengud osutavad PET/MRT võimalustele pahaloomuliste kasvajatega patsientide kliinilises käsitluses, eriti luustiku haaratuse korral. Seda tänu antud meetodi võimele kajastada luukoe metabolismi ja morfoloogiat. PET/MRT laialdase kliinilise juurutamise eelduseks on olnud mitmete tehnikaalaste väljakutsete lahendamine. Käesolev töö tegeleb kolme olulise vaatenurgaga selles arengus: kolme peamise 3D kuvamistehnikaga (PET, KT ja MRT) info koregistreerimine, footonite sumbuvuskorrektsioon inimkehas ning luustiku metabolismi ja morfoloogia võrdlev kliiniline hübriidkuvamine PET/KT ja PET/MRT abil.

Käesolevas uuringus kasutati tehnilise platvormina trimodaalset PET/KT-MRT kuvamist, mille abil uuriti luustiku täpse eristamise olulisust MRT põhistel sumbuvuskorrektsiooni maatriksitel. Sama platvormi kasutati PET/MRT kliinilise väärtuse uurimiseks kasvaja luusiiretega patsientidel. Väljatöötatud süstiklahendus võimaldas uuritud patsiente lihtsalt liigutada PET/KT ja MRT seadmete vahel, olles PETi ja MRT kujutiste riistvaralise ühildamise eelduseks. Selleks, et paremini mõista MRT-põhiselt genereeritud sumbuvuskorrektsiooni mõju, simuleeriti KT-põhisel sumbuvuskorrektsioonil luustiku puudumist ja sellest tulenevat SUV väärtuste viga. Selline analüüs võimaldas eristada keha piirkondi, kus sumbuvuskorrektsiooni viga oli oluline või kõigest minimaalne. FDG-PET/MRT võimaliku kliinilise tähenduse uurimiseks FDG-d koguvate luumetastaaside avastamisel kasutati võrdlemiseks FDG-PET/KT-d.

Uuring näitas, et luukoest tingitud sumbuvuse eiramisel MRT-põhise sumbuvuskorrektsiooni puhul alahinnatakse kogu keha PET uuringul märkaine kogunemist luukolletesse sõltuvalt kolde asukohast ja tihedusest. Seetõttu tuleb PET/MRT uuringul märkaine kogunemise täpseks kvantifitseerimiseks kasutada MRT sekventse, mis toovad esile luustiku ja kaltsifitseerunud piirkonnad.

FDG-PET/MRT hübriidkuvamisel ilmnes luumetastaaside visualiseerumise suurem usaldusväärsus ja parem nähtavus võrreldes FDG-PET/KT hübriidkuvamisega. FDG-PET kujutisel avastatud metaboolselt aktiivsete kollete morfoloogiline vaste oli MRT-l paremini näha kui KT-l. See tähelepanek toetab PET/MRT kasutamist pahaloomuliste kasvajatega patsientide luuüdi haaratuse hindamiseks.

Käesoleva väitekirja tulemused osutavad PET/MRT-le kui täppismeditsiini meetodile luustiku ainevahetuse ja morfoloogia uurimiseks pahaloomuliste kasvajatega haigetel. Täielikult integreeritud PET/MRT seadme kasutamisel on kvantitatiivse hübriidkuvamise eelduseks luukoe korrektne eristamine MRT põhisel sumbuvuskorrektsioonil.

APPENDIX 1

PUBLICATIONS

Publication I

Samarin A, Kuhn FP, Brandsberg F, von Schulthess G, Burger IA. Image registration accuracy of an in-house developed patient transport system for PET/CT+MR and SPECT+CT imaging. Nuclear Medicine Communications. 2015 Feb;36(2):194-200.

Original article

Nuclear Medicine Communications

Image registration accuracy of an in-house developed patient transport system for PET/CT + MR and SPECT + CT imaging

Andrei Samarin[a], Felix P. Kuhn[a], Fredrik Brandsberg[b], Gustav von Schulthess[a] and Irene A. Burger[a]

Objective **The aim of this study was to investigate the registration accuracy of a newly developed patient shuttle system that can integrate different scanners by patient transfer without repositioning for 'hardware'-based image fusion. We aimed to assess the registration accuracy of image fusion in two different settings: a trimodality PET/CT + MR system and a SPECT + CT system.**

Materials and methods **In this prospective study, 43 patients underwent either sequential PET/CT and MR ($n = 31$) or sequential SPECT and diagnostic CT (D-CT) ($n = 12$). A side-loading patient shuttle system was used for patient transport. For PET/CT + MR, hardware-only coregistration was performed and then validated with anatomical landmarks on CT and MR. SPECT + D-CT image fusion was performed with external cobalt-57 markers and manual fusion. Registration accuracy was analysed by anatomical landmarks on the attenuation correction CT and the D-CT.**

Results **For the PET/CT + MR system, the mean offset between original CT and MR images in all 31 patients was 8.1 ± 5.7 mm in the *X*-axis, 5 ± 4 mm in the *Y*-axis and 4.9 ± 5.6 mm in the *Z*-axis. The validation of the cobalt-57 marker-assisted SPECT + D-CT fusion yielded offsets of 0.7 ± 1.7 mm in the *X*-axis, 2.1 ± 1.7 mm in the *Y*-axis and 0.8 ± 1.8 mm in the *Z*-axis.**

Conclusion **Sequential PET/CT + MR and SPECT + D-CT imaging using a dedicated patient shuttle system is feasible, resulting in mean offsets between data sets of 10.7 mm using the gantry laser system and 2.4 mm with fiducial markers. *Nucl Med Commun* 36:194–200 © 2015 Wolters Kluwer Health | Lippincott Williams & Wilkins.**

Nuclear Medicine Communications 2015, **36**:194–200

Keywords: coregistration, image fusion, patient transporter, PET/CT + MR, sequential hybrid imaging, SPECT + CT

[a]Department of Nuclear Medicine, University Hospital of Zurich, Zurich and [b]Innovation Design Center, Thalwil, Switzerland

Correspondence to Andrei Samarin, MD, Department of Nuclear Medicine, University Hospital of Zurich, Ramistrasse 100, 8091 Zurich, Switzerland
Tel: +41 44 255 3555; fax: +41 44 255 4414; e-mail: andsam@gmail.com

Received 20 March 2014 **Revised** 28 July 2014 **Accepted** 13 September 2014

Introduction

With the introduction of fully integrated PET/CT cameras more than a decade ago, a new area in nuclear medicine was opened, combining the anatomic information of a diagnostic CT (D-CT) with physiology. As a result, the use of fluorine-18 fluorodeoxyglucose (^{18}F-FDG) PET/CT in tumour staging and therapy response assessment has increased markedly [1–3]. Inspired by the success of PET/CT, major efforts have been made to develop integrated PET/MR systems as MR has certain advantages over CT, providing higher soft tissue contrast and additional functional imaging capabilities. It has already been established that the information of a SPECT/CT is superior in diagnostic accuracy and confidence to that of SPECT and CT separately, especially in skeletal lesions [4–7]. The success of integrated imaging has thereby led to an increasing use of SPECT/CT and may lead to widespread clinical applications of PET/MR.

However, from a workflow and cost perspective, it is not obvious that fully integrated systems are the optimal solution for cost-effective image acquisition. A calculation of the scanning costs as a function of investment and operating costs showed that PET/CT is a cost-effective implementation of an integrated device while most current SPECT/CT systems are not because lengthy data acquisition on the SPECT system blocks fast data acquisition on the CT system during a large fraction of the imaging time [8]. Integration of two devices deployed in two neighbouring rooms by a patient transfer device (shuttle) could help to make SPECT/CT and potentially PET/MR systems more cost effective [8]. Integration of images from two separate devices with software-based image fusion is possible and has been used mainly for brain tumours [9], prostate [10] or pelvic tumours [11]; however, in body applications, any positional change of the patient will impair fusion accuracy and therefore only software-based fusion for PET and CT was not considered as an alternative for PET/CT [12].

We have developed a shuttle system to integrate PET, SPECT, D-CT and MR systems enabling the transfer of patients from one to the other scanning table without patient repositioning between scans. This allows 'hardware'-based image fusion. For the integration of MR with PET/CT, the shuttle system was designed such that MR surface coils could be installed and removed without

0143-3636 © 2015 Wolters Kluwer Health | Lippincott Williams & Wilkins

DOI: 10.1097/MNM.0000000000000229

Table 1 PET/CT + MR patient characteristics

Number of patients (*n*)	31
Age (mean ± SD) (years)	56.3 ± 14.2
Male [*n* (%)]	19 (61)
Injected dose of ^{18}F-FDG (MBq)	348 ± 8.4
Region of MR scan	
Abdomen	15
Abdomen and pelvis	9
Chest	5
Chest and abdomen	1
Chest, abdomen and pelvis	1
Indications	
Head and neck [*n* (%)]	3 (9.6)
Oropharyngeal cancer	3
Thorax [*n* (%)]	11 (35.5)
Pleural mesothelioma	2
Bronchial carcinoma	4
Breast cancer	3
Oesophageal cancer	2
Lymphoma [*n* (%)]	5 (16.1)
Hodgkin lymphoma	3
Non-Hodgkin lymphoma	2
Abdominal [*n* (%)]	8 (25.8)
Cholangiocellular carcinoma	1
Pancreatic cancer	1
Colon cancer	6
Melanoma [*n* (%)]	4 (12.9)

^{18}F-FDG, fluorine-18 fluorodeoxyglucose.

Table 2 SPECT + D-CT patient characteristics

Number of patients (*n*)	12
Age (mean ± SD) (years)	69.5 ± 6.9
Male [*n* (%)]	3 (25)
Injected dose of ^{99m}Tc-DPD (MBq)	669 ± 12
Field of view	
Knee	3
Lumbar spine	6
Pelvis	1
Lower leg	2
Indication	
Osseous metastasis [*n* (%)]	7 (58)
Breast cancer	6
Prostate cancer	1
Inflammatory disease [*n* (%)]	5 (42)
Prosthesis	3
Osteomyelitis	2

D-CT, diagnostic CT.

moving the patient. Thus, surface coil-induced CT streak artefacts and PET attenuation artefacts could be avoided. We have already shown that lesion discrimination and anatomical mapping with this shuttle system is feasible with a fast two-point Dixon-based T1w 3D MRI sequence and leads to similar results when comparing lesion characterization and conspicuity with low-dose CT [13]. Furthermore, our group investigated the possibility of the use of MRI sequences for attenuation correction in a trimodality PET/CT + MR system [14]. Other groups are also investigating the feasibility and benefit of fully integrated versus in-line PET/MR systems [15]; however, a tool that allows the flexible combination of a several different imaging systems has not been developed or investigated as yet.

Therefore, the purpose of this study was to assess the registration accuracy of image fusion in two different settings: a trimodality PET/CT + MR system as well as a SPECT + D-CT system.

Materials and methods

Patients

In this institutional review board-approved prospective study, 43 patients underwent either sequential PET/CT + MR ($n = 31$) or SPECT + D-CT ($n = 12$) between July 2010 and June 2011 as a part of their clinical work-up. Patient characteristics are summarized in Table 1 for PET/CT + MR and Table 2 for SPECT + D-CT. All SPECT scans were performed for the assessment of osseous pathology.

Image acquisition

PET/CT + MR scanning

PET/CT imaging was performed on a full-ring, time-of-flight PET/CT system (Discovery PET/CT 690; GE Healthcare, Waukesha, Wisconsin, USA). Patients fasted for at least 4 h. Sixty minutes after an injection of 348 ± 8.4 MBq of ^{18}F-FDG low-dose CT and PET data were acquired. CT parameters were as follows: 50–79 mAs/slice, 120 kVp, a pitch of 0.984 : 1, collimation of 64 × 0.625 mm, field of view (FOV) of 50 cm, a noise index of 20%, reconstructed to images of 0.625 mm transverse pixel size and 3.75-mm slice thickness.

After PET/CT scanning, the patients were transferred to a 3-T MR system (Discovery MR750; GE Healthcare) installed in an adjacent room. In every patient, the MR protocol included an axial T1-weighted fast dual gradient echo MR sequence with fat-water reconstruction (TR 3.8 ms, TE_1 1.15 ms, TE_2 2.3 ms, FOV 48 cm, acquisition matrix 320 × 256, with a slice thickness 6.8 mm). The water images obtained were then used for the registration performance analysis.

PET/CT and MR gantry laser systems were used to position the patient board and automatically match the coordinate systems of both scanners to allow subsequent registration of the acquired data sets.

SPECT + CT scanning

SPECT data were acquired on a Hawkeye (Millennium VG; GE Healthcare) SPECT/CT system with integrated attenuation correction CT (Ac-CT) with a 128 × 128 matrix, a 30 s acquisition time per step and a 3° rotation step size. For emission data acquisition, low-energy/high-resolution collimators were used with an energy window of 140 ± 10% keV and a FOV of 40 cm. Ac-CT parameters were as follows: 2.5 mA, 140 kV, slice thickness 10 mm and matrix 256 × 256.

After SPECT imaging, the patient was transported to a 64-slice CT (Lightspeed VCT; GE Healthcare) for a D-CT of the region of interest. D-CT parameters were as follows: 70–300 mAs/slice, 120 kV, pitch 1.188, rotation time of 0.75 s, collimation of 64 × 0.625 mm, FOV of 50 cm, a noise index of 25%, reconstructed to images of

0.625-mm transverse pixel size and 1.5-mm slice thickness.

Cobalt-57 markers (CoM) were placed on the patients' shuttle board for manual matching of the coordinate systems of Hawkeye SPECT/CT and D-CT scanners and registration of the acquired data sets.

Patient transport/shuttle

The primary goal of this study was to assess the accuracy of image fusion with a flexible shuttle system that enables the sequentially integrated use of PET/CT and MR as well as SPECT and D-CT scanners. A flexible side-loading shuttle prototype was developed and constructed in collaboration with a prototyping engineering company (Innovation Design Center, Thalwil, Switzerland) (Fig. 1). Development and production costs for this prototype were around €22k.

For SPECT + CT, the patient transport board consisted of carbon fibre, whereas for the PET/CT + MR system, the transport board was built with fibre glass to minimize radio frequency attenuation effects. The MR scanner table was undocked and the patient was positioned on it outside the MR room as the current shuttle prototype is not built with MR-compatible materials. Patient transfer time was around 10 min for both settings. No special, additional restraints were used to reduce patient motion.

Assessment of image registration accuracy

PET/CT + MR system

For trimodality PET/CT + MR imaging fusion, the matched coordinate system allowed fully automatic image fusion of the CT and MR data sets without any software-based or manual registration correction. The misalignment from the automatic registration was recorded as offsets in the *X*-axis (lateral), *Y*-axis (anterior—posterior) and *Z*-axis (cranio-caudal) between anatomical landmarks on CT and MRI. The magnitude of absolute displacement vector was calculated on the basis of the mean three-dimensional offsets. Anatomical landmarks least affected by respiratory motions and well depicted on both CT and MR images were selected: spine, pelvic bones and large paraspinal or pelvic muscles. In each patient, at least six anatomical landmarks were selected manually: three in the bony structures and three in the large muscles. Assessment of misalignment from the automatic registration was performed by two board-certified radiologists in consensus. Dedicated registration software package (Integrated Registration, Advantage Workstation 4.5; GE Healthcare) was used for the analysis.

SPECT + D-CT system

For SPECT + D-CT fusion, fully automatic coregistration with matched coordinate systems was not possible as

Fig. 1

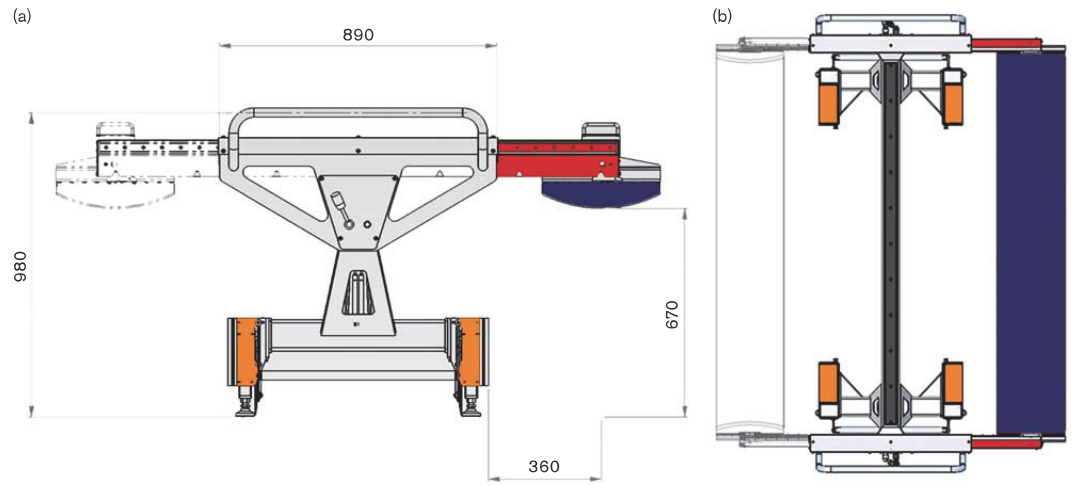

Side-loading shuttle. Frontal view (a) and top view (b) of the side-loading shuttle system, consisting of a metal trolley with counter balance weights (60 kg) on each side (orange). Two sliding 'arms' (red) hold a carbon or glass fibre board (blue) serving as a 'shuttle patient table', which can be slid either to the right or to the left of the shuttle system. This permits approaching and loading the patient onto a scanner table from either side. After sliding the board over the scanner table, the table is elevated until the board is entirely supported by it. Thereby, the board can be released from the arms, which are pulled back.

Fig. 2

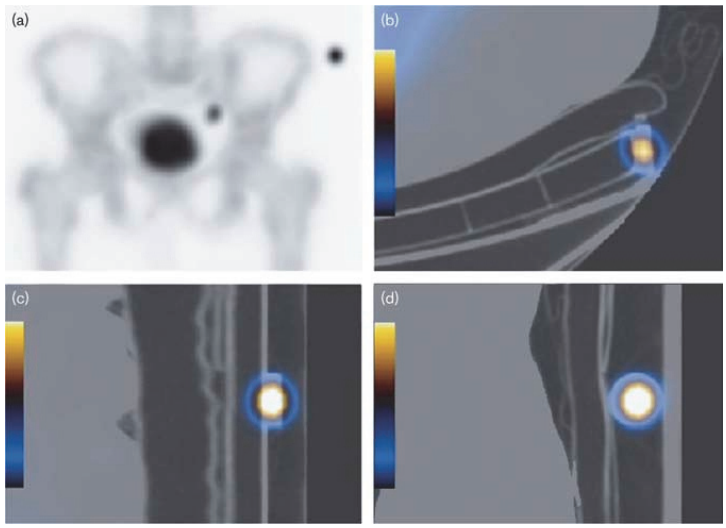

Cobalt registration marker. (a) SPECT MIP of the pelvis with a cobalt-57 marker (CoM) at the left lateral side of the carbon board. (b–d) Visual confirmation of accurate marker fusion in the fused SPECT + diagnostic CT (D-CT) images in (b) axial, (c) coronal and (d) sagittal views using the CoM.

Fig. 3

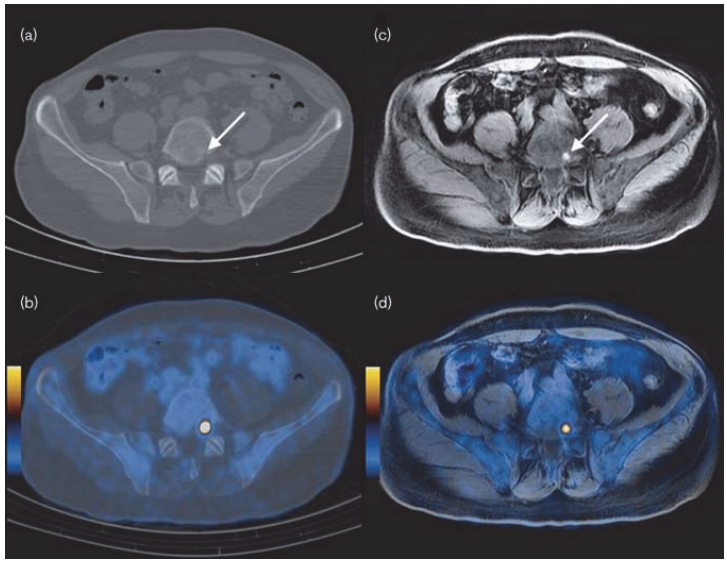

PET/CT + MR in a patient with melanoma. Bone metastasis in a 63-year-old man with malignant melanoma. (a) On CT cortical destruction is seen in the left posterior aspect of the L5 vertebral body (white arrow). (b) Fused fluorine-18 fluorodeoxyglucose (^{18}F-FDG) PET/CT image shows increased ^{18}F-FDG uptake in the osseous lesion. (c) Nonenhanced T1-weighted MR image acquired on a standalone MR scanner clearly shows the hyperintense lesion consistent with melanoma metastasis (white arrow). (d) Accurate PET/MR fusion of sequential PET and MR imaging achieved with the side-loading shuttle system with subsequent manual correction.

there is no laser patient positioning system for the Hawkeye SPECT/CT system. We therefore used external CoM attached to the shuttle table to align the coordinate systems and match SPECT and CT data (Fig. 2) with manual registration (Integrated Registration, Advantage Workstation 4.5; GE Healthcare). The accuracy of CoM-assisted image fusion was then verified against the Ac-CT by matching the bony structures between D-CT and Ac-CT datasets. Three anatomical landmarks were selected for each patient. The offsets between the landmarks were recorded in the *X*-axis (lateral), *Y*-axis (anterior–posterior) and *Z*-axis (craniocaudal). For each patient, the mean offset for the three landmarks was then calculated. The magnitude of the absolute displacement vector was calculated on the basis of the mean three-dimensional offsets.

Results

PET/CT + MR

The mean offset between CT and MR images for the PET/CT + MR setting was 8.1 ± 5.7 mm in the *X*-axis, 5.0 ± 4.0 mm in the *Y*-axis and 4.9 ± 5.6 mm in the *Z*-axis. The magnitude of the absolute displacement vector calculated on the basis of the mean three-dimensional offsets was 10.7 mm. Two clinical examples of sequential PET/CT + MR imaging with resulting accurate fusion of PET/MR images are presented in Figs 3 and 4.

SPECT + D-CT

The mean offset between anatomical landmarks on Ac-CT and D-CT in the SPECT + D-CT setting was 0.7 ± 0.8 mm in the *X*-axis, 2.1 ± 1.7 mm in the *Y*-axis and 0.8 ± 1.8 mm in the *Z*-axis. The magnitude of the absolute displacement vector calculated on the basis of the mean three-dimensional offsets was 2.4 mm. A clinical example of sequentially fused SPECT + D-CT images is shown in Fig. 5.

Discussion

The present results show that the principle of a flexible side-loading patient shuttle can be used to achieve 'hardware' fusion with offsets between PET/CT + MR of mean 10.7

Fig. 4

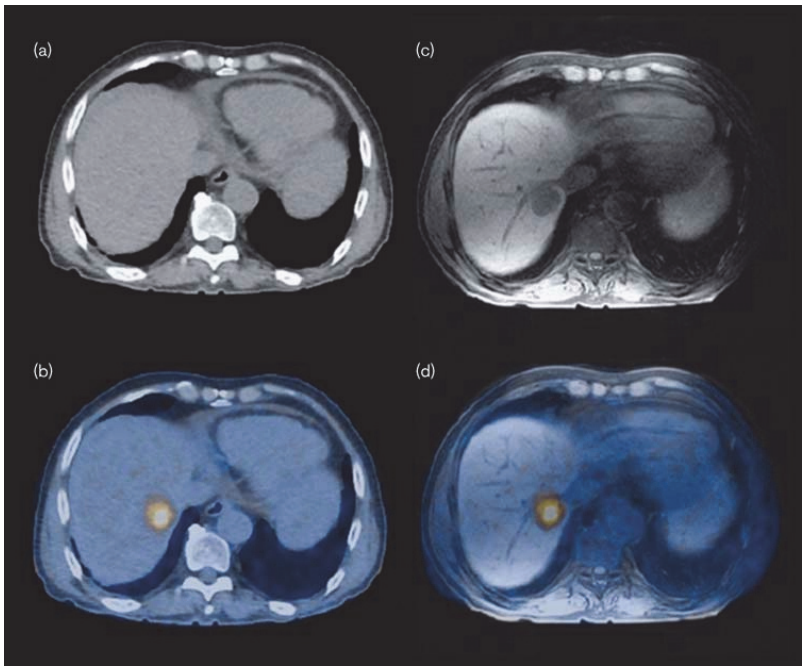

PET/CT + MR in a patient with colorectal cancer. Male patient (65 years old) with a liver metastasis of colorectal cancer in liver segment VII. (a) On nonenhanced CT image, no lesion is visible in the liver parenchyma. (b) Fused PET/CT images shows focal increased fluorine-18 fluorodeoxyglucose (^{18}F-FDG) uptake in liver segment VII. (c) Nonenhanced T1-weighted MR image acquired on a standalone MR scanner clearly shows a hypointense lesion in segment VII. (d) Accurate PET/MR fusion of sequential PET and MR imaging achieved with the shuttle system with subsequent manual correction, showing the hepatic metastasis in segment VII.

Fig. 5

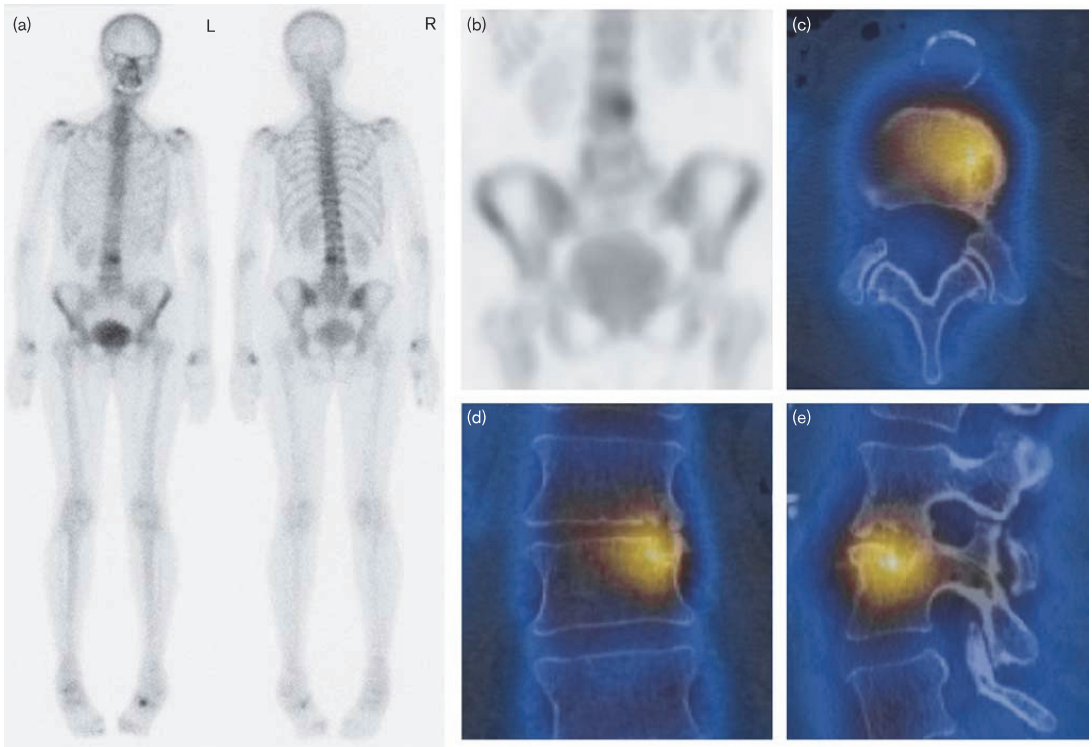

SPECT + diagnostic CT (D-CT) in a patient with breast cancer. A woman with breast cancer (71 years old), referred for staging. (a) Unclear lesion in the lumbar spine on whole-body ^{99m}Tc-DPD-scintigraphy. (b) SPECT MIP image showing the unclear lesion. (c–e) Fused SPECT + D-CT images in axial, coronal and sagittal view, respectively. Accurate fusion of sequentially acquired SPECT and D-CT images with the side-loading shuttle system allowed identification of the lesion as degenerative spondylosis L3/L4.

and 2.4 mm using fiducial markers with the SPECT + D-CT systems. Until now, only software-based image fusion data have been published for separate scanner systems such as SPECT + D-CT or PET/CT + MR [9–11,16–20]. Although the rigid structure of the skull ascertains that software fusion of brain structures is adequate, postural changes in the trunk and extremities may impair fusion accuracy [12].

Therefore, we developed and evaluated a dedicated shuttle system. In sequential integration of PET/CT and MR, the gantry laser systems can be used successfully to match the coordinate systems of both scanners. In the case of SPECT and D-CT integration, the approach utilizing cobalt sources attached to the shuttle system was developed and used to match the coordinate systems. For the trimodality PET/CT + MR system, the 'hardware' fusion of PET/CT and MR data provided registration between datasets with small offsets, showing the feasibility of this sequential approach with a dedicated patient shuttle system.

Although fully integrated SPECT with high-end CT scanner systems (≥16 slices) are available, less busy services may opt to install shuttle systems between their nuclear cameras and a nearby D-CT to be more cost effective [8]. The same could in fact be true for PET/MR implementations. Although fully integrated PET/MR have the advantage of simultaneous data acquisition without moving the patient or the table when imaging single FOVs, separate PET and MR systems have the advantage of full flexibility when placed in two separate rooms and might therefore be used more effectively. Furthermore, integrated 'hybrid' PET/MR or SPECT/CT systems are costly and beyond reach from the financial perspective for the majority of centres. A simple patient shuttle system could allow the integration of existing scanners to answer specific clinical questions without the need for costly investments.

The present study focused on image fusion accuracy arising from patient motion as well as transportation and

repositioning errors. It could be seen as a limitation that no phantom study is included to evaluate pure physical error arising from transportation and repositioning with the shuttle. However, as we were mainly interested in the performance in a daily clinical setting, patient data were analysed to evaluate the total robustness of the system. It should be taken into account that respiratory motion can cause considerable registration errors between the PET, CT and MR data. Therefore, in this study, anatomical structures least affected by respiratory motion were used for the analysis of misalignment.

A fully automatic coregistration of SPECT + D-CT data was not possible. However, manual fusion of the shuttle system cobalt sources (CoM) between SPECT and D-CT in a first step is tantamount for the laser positioning system. With this preparatory step, osseous landmarks in Ac-CT versus D-CT were only 1.2 ± 2.6 mm apart. Although not used in our study, potentially, metal and oil-containing markers attached to the shuttle table can be developed to match the coordination systems of PET/CT and MR in a similar way as for the SPECT D-CT system to complement the scanner gantry laser systems.

Further technical improvements of patient shuttle systems, such as interlocks of the shuttle with the imaging tables, might result in even more accurate coregistration between different modalities, minimizing operator dependence and obviating manual fusion.

Conclusion

Sequential PET/CT + MR and SPECT + D-CT imaging using a newly developed in-house solution for a dedicated patient shuttle system is feasible, resulting in mean offsets between data sets of 10.7 mm using the gantry laser system and 2.4 mm with fiducial markers.

Acknowledgements

This work was partially supported by a research grant from GE Healthcare, Waukesha, Wisconsin, USA.

Irene A. Burger was supported financially by Professor Dr Max Cloëtta Foundation (Switzerland) and the Swiss Society of Nuclear Medicine.

Andrei Samarin was supported by the European Union through the European Regional Development Fund.

Conflicts of interest

Fredrik Brandsberg is co-owner of Innovation Design Center, Thalwil, Switzerland. For the remaining authors there are no conflicts of interest.

References

1 Cohade C, Osman M, Leal J, Wahl RL. Direct comparison of (18)F-FDG PET and PET/CT in patients with colorectal carcinoma. *J Nucl Med* 2003; **44**:1797–1803.
2 Lardinois D, Weder W, Hany TF, Kamel EM, Korom S, Seifert B, *et al.* Staging of non-small-cell lung cancer with integrated positron-emission tomography and computed tomography. *N Engl J Med* 2003; **348**:2500–2507.
3 Von Schulthess GK, Steinert HC, Hany TF. Integrated PET/CT: current applications and future directions. *Radiology* 2006; **238**:405–422.
4 Delbeke D, Schöder H, Martin WH, Wahl RL. Hybrid imaging (SPECT/CT and PET/CT): improving therapeutic decisions. *Semin Nucl Med* 2009; **39**:308–340.
5 Even-Sapir E, Flusser G, Lerman H, Lievshitz G, Metser U. SPECT/multislice low-dose CT: a clinically relevant constituent in the imaging algorithm of nononcologic patients referred for bone scintigraphy. *J Nucl Med* 2007; **48**:319–324.
6 Helyar V, Mohan HK, Barwick T, Livieratos L, Gnanasegaran G, Clarke SE, Fogelman I. The added value of multislice SPECT/CT in patients with equivocal bony metastasis from carcinoma of the prostate. *Eur J Nucl Med Mol Imaging* 2010; **37**:706–713.
7 Papathanassiou D, Bruna-Muraille C, Jouannaud C, Gagneux-Lemoussu L, Eschard JP, Liehn JC. Single-photon emission computed tomography combined with computed tomography (SPECT/CT) in bone diseases. *Joint Bone Spine* 2009; **76**:474–480.
8 Von Schulthess GK, Burger C. Integrating imaging modalities: what makes sense from a workflow perspective? *Eur J Nucl Med Mol Imaging* 2010; **37**:980–990.
9 Grosu AL, Weber WA, Franz M, Stärk S, Piert M, Thamm R, *et al.* Reirradiation of recurrent high-grade gliomas using amino acid PET (SPECT)/CT/MRI image fusion to determine gross tumor volume for stereotactic fractionated radiotherapy. *Int J Radiat Oncol Biol Phys* 2005; **63**:511–519.
10 Park H, Wood D, Hussain H, Meyer CR, Shah RB, Johnson TD, *et al.* Introducing parametric fusion PET/MRI of primary prostate cancer. *J Nucl Med* 2012; **53**:546–551.
11 Vargas HA, Burger IA, Donati OF, Andikyan V, Lakhman Y, Goldman DA, *et al.* Magnetic resonance imaging/positron emission tomography provides a roadmap for surgical planning and serves as a predictive biomarker in patients with recurrent gynecological cancers undergoing pelvic exenteration. *Int J Gynecol Cancer* 2013; **23**:1512–1519.
12 Kim JH, Czernin J, Allen-Auerbach MS, Halpern BS, Fueger BJ, Hecht JR, *et al.* Comparison between ^{18}F-FDG PET, in-line PET/CT, and software fusion for restaging of recurrent colorectal cancer. *J Nucl Med* 2005; **46**:587–595.
13 Kuhn FP, Crook DW, Mader CE, Appenzeller P, von Schulthess GK, Schmid DT. Discrimination and anatomical mapping of PET-positive lesions: comparison of CT attenuation-corrected PET images with coregistered MR and CT images in the abdomen. *Eur J Nucl Med Mol Imaging* 2013; **40**:44–51.
14 Samarin A, Burger C, Wollenweber SD, Crook DW, Burger IA, Schmid DT, *et al.* PET/MR imaging of bone lesions – implications for PET quantification from imperfect attenuation correction. *Eur J Nucl Med Mol Imaging* 2012; **39**:1154–1160.
15 Cho ZH, Son YD, Choi EJ, Kim HK, Kim JH, Lee SY, *et al.* In-vivo human brain molecular imaging with a brain-dedicated PET/MRI system. *MAGMA* 2013; **26**:71–79.
16 Chowdhury FU, Scarsbrook AF. The role of hybrid SPECT-CT in oncology: current and emerging clinical applications. *Clin Radiol* 2008; **63**:241–251.
17 Donati OF, Hany TF, Reiner CS, von Schulthess GK, Marincek B, Seifert B, Weishaupt D. Value of retrospective fusion of PET and MR images in detection of hepatic metastases: comparison with ^{18}F-FDG PET/CT and Gd-EOB-DTPA-enhanced MRI. *J Nucl Med* 2010; **51**:692–696.
18 Kim SK, Choi HJ, Park SY, Lee HY, Seo SS, Yoo CW, *et al.* Additional value of MR/PET fusion compared with PET/CT in the detection of lymph node metastases in cervical cancer patients. *Eur J Cancer* 2009; **45**:2103–2109.
19 Nakamoto Y, Tamai K, Saga T, Higashi T, Hara T, Suga T, *et al.* Clinical value of image fusion from MR and PET in patients with head and neck cancer. *Mol Imaging Biol* 2009; **11**:46–53.
20 Patel CN, Chowdhury FU, Scarsbrook AF. Hybrid SPECT/CT: the end of 'unclear' medicine. *Postgrad Med J* 2009; **85**:606–613.

PUBLICATIONS

Publication II

Samarin A, Burger C, Wollenweber SD, Crook DW, Burger IA, Schmid DT, von Schulthess GK, Kuhn FP. PET/MR imaging of bone lesions – implications for PET quantification from imperfect attenuation correction. European Journal of Nuclear Medicine and Molecular Imaging. 2012 July;39:1154-1160

Eur J Nucl Med Mol Imaging
DOI 10.1007/s00259-012-2113-0

ORIGINAL ARTICLE

PET/MR imaging of bone lesions – implications for PET quantification from imperfect attenuation correction

Andrei Samarin · Cyrill Burger · Scott D. Wollenweber · David W. Crook · Irene A. Burger · Daniel T. Schmid · Gustav K. von Schulthess · Felix P. Kuhn

Received: 11 October 2011 / Accepted: 11 March 2012

Abstract
Purpose Accurate attenuation correction (AC) is essential for quantitative analysis of PET tracer distribution. In MR, the lack of cortical bone signal makes bone segmentation difficult and may require implementation of special sequences. The purpose of this study was to evaluate the need for accurate bone segmentation in MR-based AC for whole-body PET/MR imaging.
Methods In 22 patients undergoing sequential PET/CT and 3-T MR imaging, modified CT AC maps were produced by replacing pixels with values of >100 HU, representing mostly bone structures, by pixels with a constant value of 36 HU corresponding to soft tissue, thereby simulating current MR-derived AC maps. A total of 141 FDG-positive osseous lesions and 50 soft-tissue lesions adjacent to bones were evaluated. The mean standardized uptake value (SUVmean) was measured in each lesion in PET images reconstructed once using the standard AC maps and once using the modified AC maps. Subsequently, the errors in lesion tracer uptake for the modified PET images were calculated using the standard PET image as a reference.
Results Substitution of bone by soft tissue values in AC maps resulted in an underestimation of tracer uptake in osseous and soft tissue lesions adjacent to bones of 11.2±5.4 % (range 1.5–30.8 %) and 3.2±1.7 % (range 0.2–4 %), respectively. Analysis of the spine and pelvic osseous lesions revealed a substantial dependence of the error on lesion composition. For predominantly sclerotic spine lesions, the mean underestimation was 15.9±3.4 % (range 9.9–23.5 %) and for osteolytic spine lesions, 7.2±1.7 % (range 4.9–9.3 %), respectively.
Conclusion CT data simulating treating bone as soft tissue as is currently done in MR maps for PET AC leads to a substantial underestimation of tracer uptake in bone lesions and depends on lesion composition, the largest error being seen in sclerotic lesions. Therefore, depiction of cortical bone and other calcified areas in MR AC maps is necessary for accurate quantification of tracer uptake values in PET/MR imaging.

Keywords PET · MR · Attenuation correction · Bone segmentation · CT simulation

A. Samarin · C. Burger · D. W. Crook · I. A. Burger · D. T. Schmid · G. K. von Schulthess · F. P. Kuhn
Department of Medical Radiology, University Hospital of Zurich, Zurich, Switzerland

S. D. Wollenweber
GE Healthcare,
Waukesha, WI, USA

A. Samarin (✉)
Nuclear Medicine, University Hospital Zurich,
Rämistrasse 100,
8091 Zurich, Switzerland
e-mail: andsam@gmail.com

Introduction

Accurate attenuation correction (AC) is essential for quantitative analysis of PET tracer distribution, especially for assessing treatment response and comparing PET/MR to PET/CT data. AC of PET data based on MR images is challenging [1]. In contrast to CT data which can be easily transformed into attenuation coefficients for PET, intensity values in MR images do not reflect the X-ray density of tissues [2, 3]. Thus image processing of MR data is necessary for the generation of AC maps. Proposed approaches to

Published online: 14 April 2012

MR-based AC (MR AC) are tissue segmentation, the use of atlases or templates and pattern recognition techniques or a combination of these [4–7]. Tissue segmentation has worked well in PET/CT; however, the lack of cortical bone signal in currently available MR sequences makes bone segmentation difficult. A remedy might be provided by ultrashort or zero echo time sequences [8, 9].

There are no substantial clinical data showing whether it is necessary to segment bone in MR AC maps or whether the stronger attenuation of the 511 keV photons by bone can be replaced by the attenuation of soft tissue in such maps. Some investigators state that segmentation of CT images into three (background, lung and soft tissue) or four (background, lungs, fat and soft tissue) tissue classes to generate attenuation maps does not substantially change PET data compared to the use of standard CT AC with a mean underestimation of bone lesion SUV of 6.5 % and 8 %, respectively [5, 6]. In contrast, a recent study has shown that segmentation of whole-body CT data into four classes, while neglecting bone, results in SUV errors of >10 % in 58 % of osseous lesions [7]. All these studies evaluated the effects on a lesion by lesion basis, but did not consider that bone lesion density can vary considerably spanning from lytic to sclerotic.

In order to better understand the effects of bone attenuation using MR AC without bone segmentation, we generated whole-body error maps using CT data that allowed us to visualize the areas of the body in which the resulting errors from ignoring bone in AC were substantial or were only minimal.. Additionally, this approach allowed determination of the systematic error in PET/MR compared to PET/CT when neglecting bone for MR AC. Approaches for correcting for such errors may be necessary because some patients will undergo PET/MR and PET/CT examinations interchangeably for therapy monitoring in the future.

Errors in SUV from MR AC ignoring bone not only depend on the body region, but also on the density of the bone lesions themselves. This in turn depends on the underlying disease process and may change significantly during the course of a disease or after therapy. Frequently bone lesions are initially lytic, but on follow-up examinations the bone lesions may become sclerotic. These changes in lesion density will not be evident when treating bone as soft tissue in MR AC maps. The influence of the composition of bone lesions on the errors in SUV in segmented AC approaches has not been studied before.

The purpose of this study was therefore twofold: to generate error maps to estimate the accuracy of bone segmentation in MR AC for whole-body PET/MR imaging and to specifically look at errors in bone lesions of various compositions and lesions close to bone.

Materials and methods

Patients

This institutional review board-approved retrospective study included 22 patients with osseous lesions and soft-tissue lesions adjacent to bone who were selected from a total of 120 patients. All 22 patients underwent sequential PET/CT and 3-T MR imaging between December 2010 and June 2011 as part of a clinical/research work-up. In this study, only the PET/CT part of the studies was used. The patient characteristics are summarized in Table 1.

Image acquisition

PET/CT imaging was performed on a full-ring, state-of-the art time-of-flight PET/CT system (Discovery PET/CT 690; GE Healthcare). Patients fasted for at least 4 h prior to injection of a dose of 360.7±18 of ^{18}F-FDG (Table 1). After an uptake time of 60 min, native low-dose CT data and PET emission data were acquired from the mid-thigh to the vertex of the skull. CT data were acquired with 50–79 mAs per slice, 120 kVp, a pitch of 0.984:1, a collimation of 64×0.625 mm, a measured FOV of 50 cm and a noise index of 20 %, and were reconstructed to images of 0.625 mm transverse pixel size and 3.75 mm slice thickness. PET data were acquired in 3-D mode with a fixed scan duration of 2 min and an axial FOV of 153 mm per bed position. Seven axial FOVs were used.

Reconstruction of attenuation maps

In each patient standard and modified CT AC maps were generated by a trilinear transformation of non-enhanced low-dose CT images to 511 keV PET attenuation maps [2]. According to the performed histogram analysis of CT images (Fig. 1) the density cut-off for the bone tissue segmentation was defined as 100 HU while the representative density value for the soft tissue was set at 36 HU. Modified AC maps (AC-Mod) were produced using PMOD software (PMOD Technologies, Zurich, Switzerland) by replacing pixels with values higher than 100 HU by pixels with a

Table 1 Patient characteristics

Characteristic	Value
Number of patients	22
Age (years, mean ± SD)	58.2±14.9
Weight (kg, mean ± SD)	75.3±8.4
Male	16 (73 %)
^{18}F-FDG dose (MBq, mean ± SD)	360.7±18
^{18}F-FDG uptake time (min, mean ± SD)	62.2±3.6

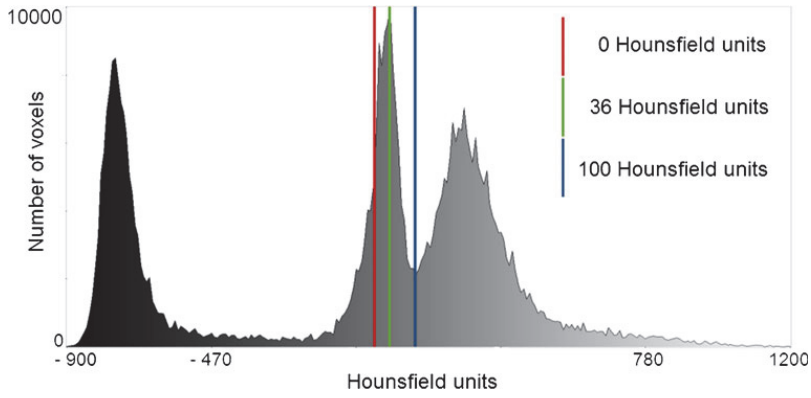

Fig. 1 Histogram analysis of CT images. The density cut-off for bone tissue segmentation was defined based on this histogram as 100 HU while that for soft tissue was set at 36 HU

constant value of 36 HU, thereby simulating substitution of bone by soft tissue in MR-derived segmented AC maps. Standard AC maps (AC-St) were produced from the same but unmodified non-enhanced low-dose CT images. Hounsfield units were transformed into 511 keV attenuation using the following algorithm: AC [1/cm]=intercept + CT value * slope. CT values below 50 HU were converted to attenuation using the kVp-independent soft-tissue conversion with an intercept of 0.096 and a slope of 9.6×10^{-5}. CT values of 50 HU and above were converted using the 120-kVp bone scale with an intercept of 0.0982 and a slope of 5.11×10^{-5}. Subsequently, two sets of attenuation-corrected PET images were reconstructed based on the modified and standard AC maps. An overview of the image reconstruction procedure is given in Fig. 2.

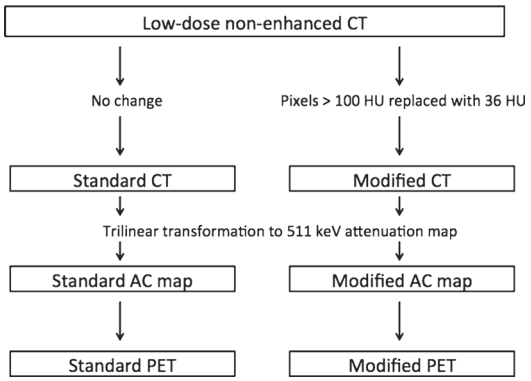

Fig. 2 Generation of AC maps followed by PET data reconstruction. The modified CT data were generated by replacing all pixels in CT sections with values >100 HU by pixels with a value of 36 HU. The "no-bone" CT data obtained were then used for AC of PET images and compared to the PET images which were AC-corrected in standard mode

Generation of a whole-body SUV error map

Whole-body maps showing the percentage differences in SUV between PET images reconstructed using the modified AC map ($PET_{AC\text{-}Mod}$) and the standard AC map ($PET_{AC\text{-}St}$) were generated using the following formula: $(PET_{AC\text{-}Mod}-PET_{AC\text{-}St})/PET_{AC\text{-}St}\times100$ %. The resulting difference map was analysed for body regions showing the largest differences in SUV.

Image analysis

First, the mean SUV of FDG avid lesions located in bone and in soft tissues adjacent to bone (within 10 mm) were measured by placing a volume of interest of 10 mm diameter on $PET_{AC\text{-}St}$ and $PET_{AC\text{-}Mod}$ images. The volume of interest was placed within PET-positive lesions of at least 1 cm^3. Subsequently, the standard error of SUVmean in the lesions was calculated for the $PET_{AC\text{-}Mod}$ images using the $PET_{AC\text{-}St}$ images as a reference. SUVmean rather than SUVmax was measured because recent literature suggests that reporting SUVmean gives results closer to reality than SUVmax [10, 11]

Bone lesions were then divided into lesions involving spine, pelvic bones and other bones. Spine and pelvic lesions were further classified into three classes based on their appearance on CT images: (1) lytic lesions showing predominant and clearly visible destruction of osseous matrix with CT density below 100 HU, (2) sclerotic lesions showing predominantly increased bone density with CT density above 200 HU, and (3) lesions of mixed density showing a combination of destructive and sclerotic changes or lesions without visible change in bone density on CT images with a CT density in the range 100–200 HU. The means and standard errors were similarly calculated for these classes as for all bone lesions and for the various anatomic locations (Table 2).

Table 2 Summary of SUV underestimation produced by reconstruction of PET images using modified AC maps

Location	Number of lesions	Mean error ± SD (%)	Minimum error (%)	Maximum error (%)
Spine, vertebral bodies				
Sclerotic	23	15.9±3.4	9.9	23.5
Mixed density	13	10.6±1.5	8.7	11.2
Lytic	7	7.2±1.7	4.9	9.3
Pelvic bones				
Sclerotic	17	14.2±4	8.4	23.8
Mixed density	15	13.1±4.9	6.2	21.3
Lytic	9	6.8±2.7	3.1	12
Spine, vertebral processes	4	9.6±3.8	4.9	13.9
Sacrum	11	8.6±4.6	4.3	19.6
Sternum	7	8.5±2.5	4.8	11.3
Ribs	10	3±1	1.5	4.8
Scapula	3	7.7±3.3	4.8	11.1
Humerus	11	8.4±3	4	11
Femur	11	16.8±7	9.5	30.8
Total bone lesions	141	11.2±5.4	1.5	30.8
Soft-tissue lesions located near bone	50	3.2±1.7	0.2	4

Results

Analysis of the whole-body error maps showed that the largest errors with an average of 15–20 % were present in bone (Figs. 3 and 4). In the soft tissues the highest SUV errors were seen in the brain and tissues just adjacent to the bones (10–15 %) with a rapid decrease in error magnitude with distance from bone. Errors in other areas of the body SUV error maps were generally below 5 %. In addition to areas of underestimation, regions of slight overestimation of SUV were also identified in soft tissue on the SUV error maps (Fig. 3), but again not exceeding 5 %. Bone lesions and soft-tissue lesions adjacent to bone were quantitatively assessed for SUV errors (Table 2). Quantitative analysis of brain lesions was not performed as the focus was on body imaging and our series contained only a single patient with a brain lesion. In Fig. 4, axial images of a fusion of SUV error maps and original CT images are shown with colour codes giving error ranges.

A total of 141 FDG-positive osseous lesions were found in 13 patients including 43 lesions in the vertebral bodies of the thoracic and lumbar spine, 41 lesions in the pelvic bones and 57 lesions in other bones. Further analysis of the density of vertebral body lesions on CT images revealed 23 sclerotic, 13 with normal or mixed density and 7 lytic lesions. In the pelvis, 17 sclerotic, 15 normal or mixed density and 9 lytic lesions were found.

Substitution of bone by soft tissue density values in AC maps resulted in a mean underestimation of SUV in all bone

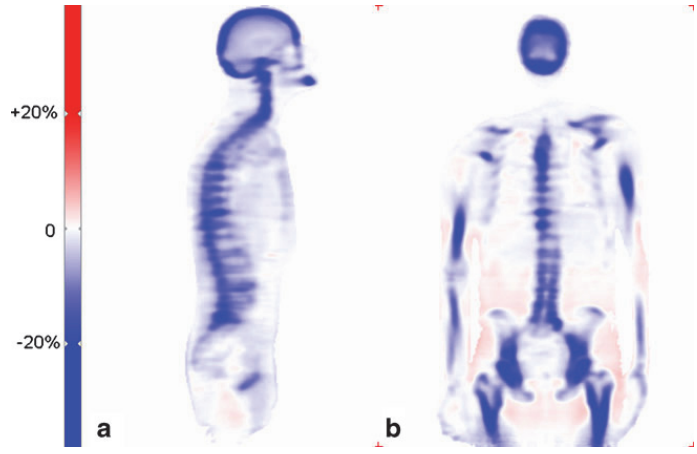

Fig. 3 Example whole-body error maps in the sagittal (**a**) and coronal (**b**) planes showing the difference in percentage SUV between PET images reconstructed using modified AC maps treating bone as soft tissue and standard AC maps. Error maps were generated using the following formula: $(PET_{AC\text{-}Mod} - PET_{AC\text{-}St})/PET_{AC\text{-}St} \times 100$ %. While most areas show SUV underestimation (*blue*), there are also some areas of slight SUV overestimation (*red*)

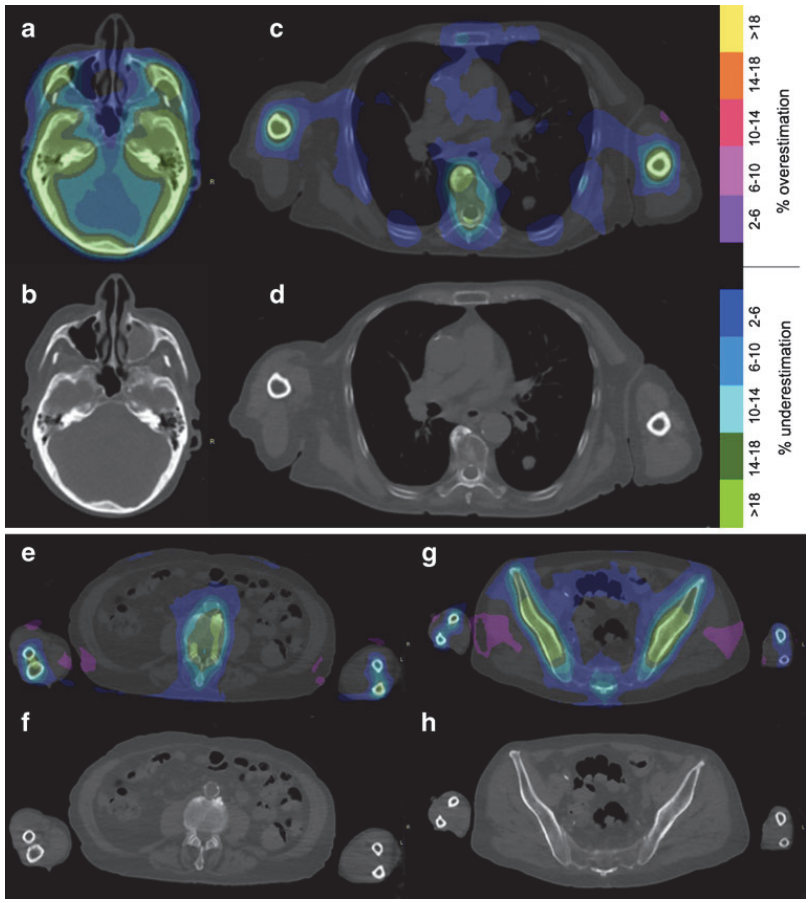

Fig. 4 Example axial images through the base of the skull (**a**, **b**), chest (**c**, **d**), abdomen (**e**, **f**) and pelvis (**g**, **h**) showing fusion of SUV error maps and original CT images. The largest underestimation in SUV is seen in bone and rapidly decreases from soft tissue adjacent to bone (within 10 mm) to more distant soft tissue. Of note, the error is substantially larger in a dense osteophyte in the right anterior aspect of the thoracic vertebral body shown (**c**, **d**) compared to the other parts of the vertebral body

lesions of 11.2±5.4 %. A minimum SUV underestimation of 1.5 % was seen in a rib lesion while a maximum SUV underestimation of 30.8 % was identified in a sclerotic lesion located in the femoral bone. A summary of SUV errors in bone lesions of different composition in various regions produced by reconstruction of PET images using the modified AC maps is given in Table 2.

Analysis of 52 spine and 41 pelvic lesions revealed an important dependence of the underestimation error on the composition of the lesions, while this error was substantially smaller in other lesions and thus not further analysed. For predominantly sclerotic, normal/mixed density and lytic lesions of the thoracic and lumbar spine vertebral bodies, the underestimation errors were 15.9±3.4 % (mean ± SD, range 23.5–9.9 %), 10.6±1.5 % (range 11.2–8.7 %) and 7.2±1.7 % (range 9.3–4.9 %), respectively. For osseous lesions in the pelvis, the corresponding underestimation errors for sclerotic, normal/mixed density and lytic lesions were 14.2±4 % (range 23.8–8.4 %), 13.1±4.9 % (range 21.3–6.2 %) and 6.8±2.7 % (range 12–3.1 %), respectively.

A total of 50 FDG-positive lesions were identified in the soft tissues adjacent to bony structures in six patients. In these lesions, substitution of the bone by soft tissue values in the AC maps resulted in underestimation errors of 3.2±1.7 % (mean ± SD). Among these lesions, the smallest error of 0.2 % was found in a lung lesion adjacent to a rib, while the largest error of 4 % was seen in a lymph node adjacent to the osseous pelvis.

Discussion

Decreases in SUV were highest for lesions within or next to bone when PET images were reconstructed using a modified AC map treating bone as soft tissue versus a standard AC map. The magnitude of this error decreased rapidly with the distance

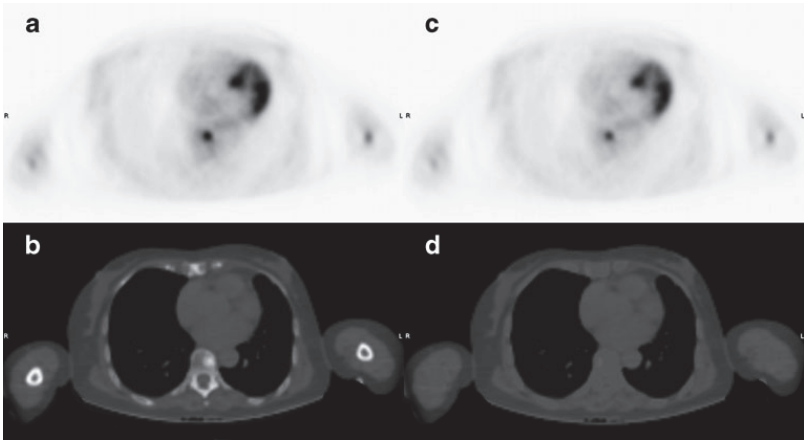

Fig. 5 A 70-year-old woman with a sclerotic bone metastasis of breast cancer in thoracic vertebral body 10. **a** PET image reconstructed using the standard CT AC map shows an FDG-avid lesion in the left anterior aspect of T10. **b** Standard CT AC map shows that the bone lesion is sclerotic. **c** PET image reconstructed using the modified CT AC map. **d** In the modified CT AC map bone is substituted by soft tissue. In this case modification of the AC map has resulted in underestimation of FDG uptake by 23 % in this bone metastasis in the modified PET image

form bone and showed only a very small difference in other areas of the body (brain not analysed in this study). Therefore 191 lesions, 141 in bone and 50 adjacent to bone were examined in more detail. Based on the analysis of the 141 FDG-positive bone lesions, substitution of bone by soft tissue in AC maps for PET resulted in average underestimation of SUV in bones by around 10 %. Lesions located in the ribs showed an average error below 5 %, while lesions located in the proximal femur showed a larger average error of more than 15 %. Importantly, in our study the maximum SUV underestimation for bone lesions of more than 20 % was seen in dense sclerotic lesions: 23.5 % for spine lesions, 23.8 % for pelvic bone lesions and 30.8 % for femoral lesions.

Compared to the studies performed by Martinez-Möller et al. [5] (21 osseous lesions with an average SUV change of 8± 3 % and maximal underestimation of 13.1 % seen in a lesion in the pelvic bone) and by Schulz et al. [6] (7 bone lesions with an average underestimation of 6.5±4.1 % and maximum error of −13.4 % seen in a pelvic bone lesion), the average and maximum errors seen in osseous lesions were significantly higher in our study. The results of our study support the findings of Hofmann et al. which showed tracer uptake quantification errors of >10 % in 58 % of osseous lesions and errors >20 % in 22 % of the lesions [7]. The difference in the magnitude of underestimation may be explained by the larger number of osseous lesions examined in our study (141), and their location and composition. Additionally, another important factor may be the different approaches to reconstruction of the AC maps as we substituted only bone by soft tissue values rather than using a full three- or four-class CT segmentation. This approach allowed us to determine the effect of bone attenuation by changing only one parameter.

The errors observed are of interest for understanding the systematic errors in MR AC-based PET scans, but are particularly relevant when comparing the data obtained from PET/CT and PET/MR for treatment response assessment. In fact, an AC-induced 20–30 % error in SUV of a lesion might change the assessment of treatment response.

To our knowledge this is the first study showing a substantial difference in underestimation of SUV in PET between dense sclerotic and destructive lytic bone lesions when neglecting the bone in AC maps. The presence of 52 spine and 41 pelvic bone lesions allowed us to assess the dependence of the error on the density of the bone lesions. We found a substantial difference in SUV underestimation between the sclerotic lesions with an average error of −15.9 % in spine and −14.2 % in pelvic lesions and lytic lesions with respective underestimation values of −7.2 % and −6.8 %. The commonly used approach to MR-based AC is tissue segmentation with substitution of bone by soft tissue values [5–7, 12, 13]. In bone lesions with little or no change in density over the therapeutic course, this type of segmentation will result only in a systematic under-correction of bone attenuation between consecutive PET/MR scans and interpretation is not truly affected. However, the density of the bone lesions can change significantly during the course of the disease—and this will have an impact on their attenuation properties. Treating bone as soft tissue in the MR AC maps of consecutive PET/MR scans performed for assessment of treatment response may result in SUV differences solely due to changes in lesion density and not due to a change in the metabolic activity of the lesion.

The magnitude of the SUV error of bone lesions is dependent not only on their own density but also on the density of the surrounding bones, being smaller in osteoporotic bones and

larger in the presence of degenerative changes or in certain disease states (e.g. myelofibrosis, mastocytosis, osteopetrosis).

Analysis of whole-body SUV error maps also revealed an underestimation of tracer uptake in soft tissues adjacent to bone. Dedicated analysis of 48 soft tissue lesions in close proximity to bone revealed that the errors were lower than 5 % (mean underestimation 3.2 %, maximum 4 %), which for clinical purposes may be negligible. While our data do not allow the relevance of skull bone for the AC of brain lesions to be addressed, other authors have shown that this is mandatory to quantify brain PET examinations [14]. In addition to the SUV underestimation highlighted above, minor SUV overestimation was also seen in some soft tissue regions. This is potentially due to differences caused by the interaction between changes in attenuation and the scatter correction of the data, but again is hardly clinically relevant.

In agreement with lesion-based evaluations of other studies [5, 6], our AC maps suggest that for lesions in soft tissues, fat or lung, the omission of bone from the AC of PET data is clinically not relevant, at least at the levels of accuracy at which SUV values are used nowadays. However, neglecting bone can lead to relatively high SUV errors in lesions within bone, especially in sclerotic areas. Therefore, in PET/MR, the application of MR sequences able to depict bone might be necessary not only for MR AC in brain tissue, but also for lesions within bone throughout the body. In such lesions we have no a priori knowledge without CT data if they are lytic, sclerotic or mixed, and this can change during the course of a disease, making therapy monitoring challenging when using MR AC ignoring attenuation by bone.

Conclusion

Treating bone as soft tissue in MR-derived AC maps for PET/MR leads to a substantial underestimation of SUV values in bone lesions. The errors depend substantially on lesion composition, with the largest error being seen in sclerotic lesions. Therefore depiction of the cortical bone and sclerotic areas in MR AC maps is necessary for accurate quantification of tracer uptake values in whole-body PET/MR imaging.

Acknowledgments The authors thank Albert Lonn for useful discussions.

Research support This work was supported in part by a research grant from GE Healthcare, Waukesha, WI, USA.

Conflicts of interest One of the authors (S.W.) is an employee of GE HealthCare, Waukesha WI, USA.
The research group receives research support from GE Healthcare.

References

1. Hofmann M, Pichler B, Scholkopf B, Beyer T. Towards quantitative PET/MRI: a review of MR-based attenuation correction techniques. Eur J Nucl Med Mol Imaging. 2009;36 Suppl 1:S93–S104. doi:10.1007/s00259-008-1007-7.
2. Burger C, Goerres G, Schoenes S, Buck A, Lonn AH, Von Schulthess GK. PET attenuation coefficients from CT images: experimental evaluation of the transformation of CT into PET 511-keV attenuation coefficients. Eur J Nucl Med Mol Imaging. 2002;29(7):922–7. doi:10.1007/s00259-002-0796-3.
3. Beyer T, Weigert M, Quick HH, Pietrzyk U, Vogt F, Palm C, et al. MR-based attenuation correction for torso-PET/MR imaging: pitfalls in mapping MR to CT data. Eur J Nucl Med Mol Imaging. 2008;35(6):1142–6. doi:10.1007/s00259-008-0734-0.
4. Hofmann M, Steinke F, Scheel V, Charpiat G, Farquhar J, Aschoff P, et al. MRI-based attenuation correction for PET/MRI: a novel approach combining pattern recognition and atlas registration. J Nucl Med. 2008;49(11):1875–83. doi:10.2967/jnumed.107.049353.
5. Martinez-Möller A, Souvatzoglou M, Delso G, Bundschuh RA, Chefd'hotel C, Ziegler SI, et al. Tissue classification as a potential approach for attenuation correction in whole-body PET/MRI: evaluation with PET/CT data. J Nucl Med. 2009;50(4):520–6. doi:10.2967/jnumed.108.054726.
6. Schulz V, Torres-Espallardo I, Renisch S, Hu Z, Ojha N, Bornert P, et al. Automatic, three-segment, MR-based attenuation correction for whole-body PET/MR data. Eur J Nucl Med Mol Imaging. 2011;38(1):138–52. doi:10.1007/s00259-010-1603-1.
7. Hofmann M, Bezrukov I, Mantlik F, Aschoff P, Steinke F, Beyer T, et al. MRI-based attenuation correction for whole-body PET/MRI: quantitative evaluation of segmentation- and atlas-based methods. J Nucl Med. 2011;52(9):1392–9. doi:10.2967/jnumed.110.078949.
8. Keereman V, Fierens Y, Broux T, De Deene Y, Lonneux M, Vandenberghe S. MRI-based attenuation correction for PET/MRI using ultrashort echo time sequences. J Nucl Med. 2010;51(5):812–8. doi:10.2967/jnumed.109.065425.
9. Robson MD, Bydder GM. Clinical ultrashort echo time imaging of bone and other connective tissues. NMR Biomed. 2006;19(7):765–80. doi:10.1002/nbm.1100.
10. Schwartz J, Humm JL, Gonen M, Kalaigian H, Schoder H, Larson SM, et al. Repeatability of SUV measurements in serial PET. Med Phys. 2011;38(5):2629–38.
11. Burger IA, Huser DM, Burger C, von Schulthess GK, Buck A. Repeatability of FDG quantification in tumor imaging: averaged SUVs are superior to SUVmax. Nucl Med Biol. 2012; in press. doi:10.1016/j.nucmedbio.2011.11.002
12. Schleyer PJ, Schaeffter T, Marsden PK. The effect of inaccurate bone attenuation coefficient and segmentation on reconstructed PET images. Nucl Med Commun. 2010;31(8):708–16. doi:10.1097/MNM.0b013e32833b0573.
13. Eiber M, Martinez-Moller A, Souvatzoglou M, Holzapfel K, Pickhard A, Loffelbein D, et al. Value of a Dixon-based MR/PET attenuation correction sequence for the localization and evaluation of PET-positive lesions. Eur J Nucl Med Mol Imaging. 2011;38(9):1691–701. doi:10.1007/s00259-011-1842-9.
14. Catana C, van der Kouwe A, Benner T, Michel CJ, Hamm M, Fenchel M, et al. Toward implementing an MRI-based PET attenuation-correction method for neurologic studies on the MR-PET brain prototype. J Nucl Med. 2010;51(9):1431–8. doi:10.2967/jnumed.109.069112.

PUBLICATIONS

Publication III

Samarin A, Hüllner M, Queiroz MA, Stolzmann P, Burger IA, von Schulthess G, Veit-Haibach P. ^{18}F-FDG-PET/MR increases diagnostic confidence in detection of bone metastases compared with ^{18}F-FDG-PET/CT. Nuclear Medicine Communications. 2015 Dec; 36(12):1165-73

Original article

Nuclear Medicine Communications

^{18}F-FDG-PET/MR increases diagnostic confidence in detection of bone metastases compared with ^{18}F-FDG-PET/CT

Andrei Samarin[a,e], Martin Hüllner[a,c,d], Marcelo A. Queiroz[a], Paul Stolzmann[a,b,d], Irene A. Burger[a,b,d], Gustav von Schulthess[a] and Patrick Veit-Haibach[a,b,d]

Purpose **The aim of this study was to compare detection, lesion conspicuity and reader confidence of ^{18}F-fluorodeoxyglucose (^{18}F-FDG)-PET/MR and ^{18}F-FDG-PET/computed tomography (CT) in patients with ^{18}F-FDG avid bone metastases.**

Materials and methods **In this prospective study, a total of 30 PET/CT and PET/MRI data sets were performed in 24 patients. Each examination was evaluated for the presence of PET-positive bone lesions consistent with metastatic involvement. Conspicuity of PET-positive bone lesions was evaluated on the corresponding PET/CT and PET/MR images and compared using the Wilcoxon signed-ranks test. Reader confidence was determined to evaluate whether PET/CT or PET/MR was more useful for the assessment of the bone metastases and was compared using Student's *t*-test.**

Results **Overall, in both examinations, PET/CT and PET/MRI detected 86 ^{18}F-FDG-positive bone lesions. On all 30 PET/MRI examinations, at least one morphological correlate for ^{18}F-FDG-positive bone lesions was found on the MR component (82 out of 86 lesions). PET/CT imaging allowed identification of corresponding structural changes on the CT component in 23 out of 30 studies (65 out of 86 lesions). In lesion-by-lesion analysis, the mean lesion conspicuity was significantly better on T1 fat MR imaging compared with CT imaging ($P = 0.005$). In seven out of 30 studies, a significant increase in reader confidence of PET/MRI compared with PET/CT was found.**

Conclusion **PET/MRI offers higher reader confidence and improved conspicuity in bone metastases compared with PET/CT. However, the overall detection rate was not different. The highest possible clinical impact of PET/MRI appears to be in patients with limited, early bone metastatic disease.** *Nucl Med Commun* **36:1165–1173**

Nuclear Medicine Communications 2015, **36**:1165–1173

Keywords: bone metastases, hybrid imaging, PET/CT, PET/MR

Departments of [a]Nuclear Medicine, [b]Diagnostic and Interventional Radiology, [c]Department of Neuroradiology, University Hospital Zurich, University of Zurich, [d]University of Zurich, Zurich, Switzerland and [e]Department of Medical Radiology, North Estonia Medical Centre, Tallinn, Estonia

Correspondence to Andrei Samarin, MD, Department of Medical Radiology, North Estonia Medical Centre, Sutiste tee 19, 13419 Tallinn, Estonia
Tel: +372 6171147; fax: +372 6171242; e-mail: andsam@gmail.com

Received 3 April 2015 **Revised** 1 August 2015 **Accepted** 20 August 2015

Introduction

The presence of bone metastases is a major prognostic factor in patients with oncological disease. Early and confident detection of bone metastases enables accurate staging and selection of the optimum treatment of oncological disease.

Multiple imaging techniques are currently available for the detection of the metastatic bone disease including bone scintigraphy, CT, MR and PET/CT imaging [1,2]. Recently, PET/MR hybrid imaging was introduced as a promising tool in oncological imaging research [3]. One of the potential benefits of PET/MR compared with other imaging modalities may be improved detection and characterization of bone metastases.

Whole-body MR imaging has been shown to have superior diagnostic accuracy compared with CT and bone scintigraphy in detection of bone metastases because of its ability to assess early infiltration of bone marrow that precedes osteoblastic and osteoclastic response of the bone matrix to malignant tissue infiltration [4,2,5–7]. The comparison of whole-body MR and PET/CT for the detection of bone metastases in solid tumours and haematological malignancies yielded heterogeneous results depending on the tumour histology and the PET tracer used [8–14]. Importantly, integrated PET/CT has been reported to show a high positive predictive value of 98% for identification of bone metastases when both PET and CT components of the examination are concordant [15]. However, when CT and PET results are discordant, the positive predictive value of PET/CT significantly decreases to 61% [15]. The implementation of hybrid PET/MR imaging may potentially improve detection of early bone marrow infiltration, reduce the number of discordant findings and therefore increase diagnostic confidence in the detection and evaluation of bone metastasis.

It is not yet clear whether PET/MR provides a clinical benefit compared with PET/CT for the detection and evaluation of bone metastasis.

The aim of our study was to compare detection, lesion conspicuity and reader confidence of ^{18}F-FDG-PET/MR

0143-3636 DOI: 10.1097/MNM.0000000000000387

and ^{18}F-FDG-PET/CT in patients with ^{18}F-FDG avid bone metastases.

Materials and methods

Patients

In this prospective study, 24 patients (nine men, 15 women; median age 61.5 years, range 43–89 years) underwent sequential whole-body trimodality ^{18}F-FDG-PET/CT – MR between May 2011 and June 2013 as a part of clinical work-up for either staging or restaging/follow-up of various malignant tumours and suspicion of bone metastases (30 examinations). The primary diseases were breast cancer (12 patients), lung cancer (three patients), tonsil cancer (two patients), non-Hodgkin lymphoma (two patients) and carcinoma of the urethra, gastric cancer, cervical cancer, spindle cell skin cancer and medullary thyroid carcinoma (one patient each). Clinical indication for the PET/CT-examination was therapy follow-up (11 exams), primary staging (10 exams) and restaging (nine exams). All patients had histological confirmation of their primary disease. The mean follow-up period was 18.5 months (range: 12–36 months). No further selection was applied for patient inclusion. Patients unwilling to undergo an additional MR examination, those who had claustrophobia and those with MR-incompatible medical devices (e.g. cardiac pacemaker, insulin pump, neurostimulator, cochlear implant) were not considered for study inclusion. Six out of 24 patients underwent the PET/CT + MR study twice (mean interval 311 days) and, therefore, 30 studies were available for overall analysis. This study was approved by the institutional ethics committee and written informed consent was obtained from all patients before the examination. Patient characteristics are summarized in Table 1.

Table 1 Patient characteristics

Patient number	Age (years)	Sex	Diagnosis
1	46	F	Breast carcinoma
2	89	F	Breast carcinoma
3	54	F	Breast carcinoma
4	50	F	Breast carcinoma
5	44	F	Breast carcinoma
6	61	M	Renal carcinoma. Tonsil carcinoma
7	48	M	Malignant lymphoma
8	58	M	Spindle cell skin cancer
9	69	M	Medullary thyroid carcinoma
10	49	F	Breast carcinoma
11	81	F	Cancer of the uterine cervix
12	83	F	Breast carcinoma
13	44	F	Adenocarcinoma of the stomach
14	43	F	Lung adenocarcinoma
15	62	F	Breast carcinoma
16	69	M	Lung adenocarcinoma
17	66	F	Breast carcinoma
18	63	M	Malignant lymphoma
19	69	M	Lung adenocarcinoma
20	64	M	Carcinoma of the urethra
21	49	F	Breast carcinoma
22	78	F	Breast carcinoma
23	67	M	Tonsil carcinoma
24	58	F	Breast carcinoma

F, female; M, male.

Image acquisition

Sequential PET/CT and MR imaging was performed on a trimodality PET/CT-MR set-up (full-ring, time-of-flight Discovery PET/CT 690 and a 3-T Discovery MR 750; both GE Healthcare, Waukesha, Wisconsin, USA). Patients fasted for at least 4 h before injection of a standard dose of an average of 4.5 MBq /kg body weight of ^{18}F-FDG.

After injection, all patients were positioned on a dedicated shuttle board that was placed on top of the MR table. Patients had a resting time of ~30 min before going into the MR. A mechanism able to transfer the shuttle board from the MR-table to the PET/CT table ensured that patient transport from the MR system to the PET/CT and placement/removal of dedicated radiofrequency coils were possible without repositioning the patient [16]. With this, image sets of PET/CT and PET/MR were available for diagnostic and comparative purposes. After placing the patient onto the shuttle board, a dedicated radiofrequency coil (GEM 32-channel torso coil, posterior and anterior array combined; GE Healthcare) was positioned on the patient. The MR imaging protocol consisted of three different sequences. Whole-body multisection imaging was performed using a T1-weighted three-dimensional (3D) dual-echo gradient-recalled echo pulse sequence [liver accelerated volume acquisition (LAVA)-Flex; GE Healthcare]. LAVA acquisition was performed during end-expiratory breath-hold for breathing sensitive areas (thorax, abdomen). Whole-body multisection imaging was also performed with a coronally acquired short TI inversion recovery (STIR) sequence using parallel imaging. No breath-hold technique was used. Finally, a T2-weighted sequence with motion correction [periodically rotated overlapping parallel lines with enhanced reconstruction (Propeller); GE Healthcare] was acquired using a breathing trigger in the thorax. This sequence was used for enhanced breathing-triggered lung imaging. The total MR acquisition time was ca. 16 min. Detailed acquisition parameters for all MR sequences are presented in Table 2.

After completion of the MR examination, patients were shuttled to the PET/CT.

Low-dose CT data were acquired for PET attenuation correction (AC) and for diagnostic purposes. Tube voltage was 120 kV (peak), reference tube current was 12.35 mA/slice, automated dose modulation range was 15–80 mAs/slice, collimation was 64×0.625 mm, pitch was 0.984 : 1, rotation time was 0.5 s, field of view (FOV) was 50 cm and noise index was 20%. CT image sets were reconstructed using an iterative algorithm (Adaptive Statistical Iterative Reconstruction; GE Healthcare). The PET data were acquired in 3D TOF mode with a scan duration of 2 min per bed position, an overlap of bed

Table 2 Acquisition parameters for MR imaging

Parameters	LAVA	STIR	Propeller
TR/TE (ms)	4.3/1.3 (OP), 2.6 (IP)	2000/42	9321/122
Flip angle	12°	N/A	N/A
Partial Fourier	0.9%	N/A	N/A
TI (ms)	N/A	160	N/A
Partial imaging acceleration factor	2	2	3
Slice thickness (mm)	4.0	6	4.5
FOV (cm)	50	50	40
Acquisition matrix (pixels)	288×224	384×224	288×288
Receiver bandwidth (kHz)	142.86	100	62.5
Acquisition time per body section (s)	18	123	N/A
Body sections per patient	4	3	1
Total acquisition time (min)	ca. 3	ca. 8	ca. 5
Coverage	Whole body	Whole body	Chest, upper abdomen

FOV, field of view; IP, in-phase; LAVA, liver accelerated volume acquisition, T1-weighted 3D dual-echo gradient-recalled echo pulse sequence; OP, opposed phase; Propeller, periodically rotated overlapping parallel lines with enhanced reconstruction, T2-weighted sequence with motion correction; STIR, short TI inversion recovery sequence; TE, time to echo; TI, inversion time; TR, time of repetition.

positions of 23%, an axial FOV of 153 mm and a 700 mm diameter FOV. The emission data were corrected for attenuation using the low-dose CT (CTAC) and iteratively reconstructed [matrix size 256×256, VUE Point FX (3D TOF-OSEM) with three iterations, 18 subsets]. Images were filtered in image space using an in-plane Gaussian convolution kernel with a full-width at half-maximum of 4.0 mm, followed by a standard axial filter with a three-slice kernel. This procedure has been used in this standard manner in other studies as well [17].

Image processing

The PET, CT and MR images acquired were sent to a dedicated review workstation (Advantage workstation, version 4.6; GE Healthcare) that enables simultaneous review of PET, CT and MR images side by side or in fused/overlay mode (PET/CT, PET/MR). For this study, PET/CT and PET/MRI data sets were compared. The standard of reference consisted of histology (if available) or follow-up with at least one additional cross-sectional imaging examination.

Image analysis

Assessment of lesions in all below-mentioned categories was performed by two readers (certified in radiology and nuclear medicine) in consensus. PET/CT was evaluated first. Then, with a time gap of 6 weeks, the PET/MR images were also evaluated by the same readers in consensus. The readers were blinded to any possible previous PET/CT or MR imaging. However, the readers were aware of the diagnosis of the patients and were aware of the clinical question for the respective clinical PET/CT.

Detection of PET-positive bone lesions

First, each PET examination was evaluated for the presence of PET-positive bone lesions. Lesions were considered PET positive if their maximum standardized uptake value (SUV_{max}) was significantly higher than liver uptake. In cases where increased uptake was visible but inferior to liver uptake, the surrounding tissue was taken as a reference. For every lesion SUV_{max}, the mean standardized uptake value (SUV_{mean}), total lesion glycolysis and metabolic tumour volume (PET_{vol}) were measured. The threshold value as percentage of SUV_{max} was adjusted manually for each lesion such that the borders of the volume of interest only included activity that could be ascribed to the lesion. The location and the number of the lesions were recorded. Up to ten PET-positive lesions were evaluated per patient with a maximum of three lesions per body compartment (e.g. cervical, thoracic, lumbar spine, pelvis). In patients with multiple confluent lesions in the same compartment, lesions that were clearly distinguishable from each other were selected for analysis. ^{18}F-FDG-negative lesions with benign radiological appearance were not evaluated in this study.

Lesion conspicuity

The conspicuity of PET-positive bone lesions was evaluated on the corresponding PET/CT and PET/MR images. For this analysis, the conspicuity of the morphological imaging component was assessed (CT or MR). Lesions were assessed on the basis of a five-point scale: grade 0 – lesion was not detectable, grade 1 – 1–25% lesion contour detectable, grade 2 – 26–50% contour detectable, grade 3 – 51–75% contour detectable and grade 4 – 76–100% contour detectable. The evaluation described was applied for all the reconstructions of the T1-weighted 3D gradient echo sequence (in-phase, out-phase, fat and water), for the whole-body STIR sequence and for the CT images. A time gap of 6 weeks between the assessment of PET/CT and PET/MR images was applied to eliminate potential bias.

Lesion size

Measurements of the maximum lesion diameters on CT and MR images were obtained. Lesions not visible on the CT or MR images were not measured in that particular modality and noted as 'not measurable'. Measurements on the MRI component were taken on the reconstructed T1 in-phase images.

Lesion density

All lesions were assigned to three groups on the basis of their CT appearance. (a) Sclerotic lesions with predominantly an increase in bone density. (b) Lytic lesions with predominantly destruction of bone tissue. (c) ^{18}F-FDG-positive lesions without change in bone density, for example lesions not visible on CT imaging.

Reader confidence

Reader confidence was determined qualitatively to evaluate whether PET/CT or PET/MR was more useful for the assessment of the evaluated bone metastases. The following score was used for assessment.

High reader confidence

^{18}F-FDG-positive lesions had a morphologic correlate and overall hybrid imaging findings correlated to metastatic involvement – 2 points.

Moderate reader confidence

PET-positive findings are suggestive of metastatic disease, but only partially show a morphologic correlate – 1 point.

Low reader confidence

PET findings are inconclusive, no clear morphologic correlate is seen for ^{18}F-FDG-positive lesions – 0 points.

Statistical analysis

Ordinal variables were expressed as median (range), nominal variables as mode (percentage) and ratio variables as geometric mean ± SD. For the purpose of clarity, the conspicuity score was also expressed as mean ± SD. The size and conspicuity of lesions in different modalities were compared using the Wilcoxon signed-ranks test for matched pairs. Size, conspicuity and PET parameters of lesions stratified by CT-density and location on CT and MR images were compared using the Mann–Whitney *U*-test for independent samples. Reader confidence was compared using Student's *t*-test. A *P*-value of less than 0.05 was considered statistically significant. All statistical analyses were carried out with IBM SPSS Statistics 19.0.1 (IBM, Armonk, New York, USA).

Results

A total of 30 PET/CT and PET/MRI data sets were performed in 24 patients. A total of 86 ^{18}F-FDG-positive bone lesions were identified. In 12 data sets, patients had multiple disseminated bone lesions, whereas in the remaining 18 data sets, less than 10 lesions were present in each patient. The metabolic and morphologic characteristics of the lesions are summarized in Table 3.

Table 3 Summary of metabolic and morphologic characteristics of all ^{18}F-FDG-positive bone lesions

	N	Minimum	Maximum	Mean	SD
Metabolic characteristics					
SUV_{max}	86	2.2	29.7	7.96	5.2
SUV_{mean}	86	1.2	14.2	4.6	2.69
TLG	86	477	441 931	32 243.91	77 688.86
PET_{vol}	86	0.42	83.8	5.74	12.1
Size (mm)					
CT	65	4	84	17.03	16.77
MR T1 in-phase	82	5	85	20.63	17.2
Conspicuity, score					
CT	86	0	4	2.35	1.62
MR STIR	86	0	4	2.23	1.57
MR T1 water	86	0	4	2.48	1.42
MR T1 fat	86	0	4	3.09	1.44
MR T1 in-phase	86	0	4	2.21	1.46
MR T1 out-phase	86	0	4	2.76	1.47

MR T1 water, fat, in-phase, out-phase, T1-weighted 3D dual-echo gradient-recalled echo pulse sequence, liver accelerated volume acquisition, corresponding water, fat, in-phase and out-phase reconstruction; MR STIR: short TI inversion recovery sequence; PET_{vol}, metabolic tumour volume; SUV_{max}, maximum standardized uptake value; SUV_{mean}, mean standardized uptake value; TLG, total lesion glycolysis.

Detection

Overall, in both examinations, PET/CT and PET/MRI detected the same number of lesions on the basis of the PET component (as both examinations used the same PET-data set).

In those 30 data sets, 95% of analyzed ^{18}F-FDG-positive bone lesions (82/86 lesions) had a morphologic correlate on the MR component. Thus, on all PET/MRI examinations, at least one morphological correlate was found on the MR component.

PET/CT imaging enabled identification of structural changes on the CT component in 76% of the ^{18}F-FDG-positive lesions (65/86 lesions). A morphologic correlate on the CT component of the PET/CT was clearly identified in 23 PET/CT studies out of 30.

Overall, in seven examinations (seven patients), ^{18}F-FDG-positive bone lesions ($n = 9$) were seen only on the MR component without clearly visible changes of the bony structure on CT. In two of these examinations (two patients), patients had one single ^{18}F-FDG-positive lesion that was not visible on MR or CT images. However, in both of these examinations, a single additional ^{18}F-FDG-positive bone lesion (two lesions in total) was seen again only on the MR component in a different location. No additional lesions were seen on the CT component in those cases. The remaining lesions that were ^{18}F-FDG positive but CT negative were all seen in patients where several other bone metastases were detected on both the PET component and the CT component.

In two different examinations (two patients), the structural bone change in two ^{18}F-FDG-positive lesions was seen only in the CT component but not in the MRI component. Again, in those patients, additional ^{18}F-FDG-positive bone lesions (four lesions) showed a morphological correlate on the MR component.

Reader confidence

The overall reader confidence on the basis of the above-mentioned scale for PET/CT was 1.76 and 2.0 for PET/MRI ($P = 0.0029$). PET/MR showed a high confidence in all patients. However, in PET/CT, a high confidence was found in 23 cases and a moderate confidence in seven cases (Figs 1 and 2). In 23 studies, no change in reader confidence was observed between PET/CT and PET/

Fig. 1

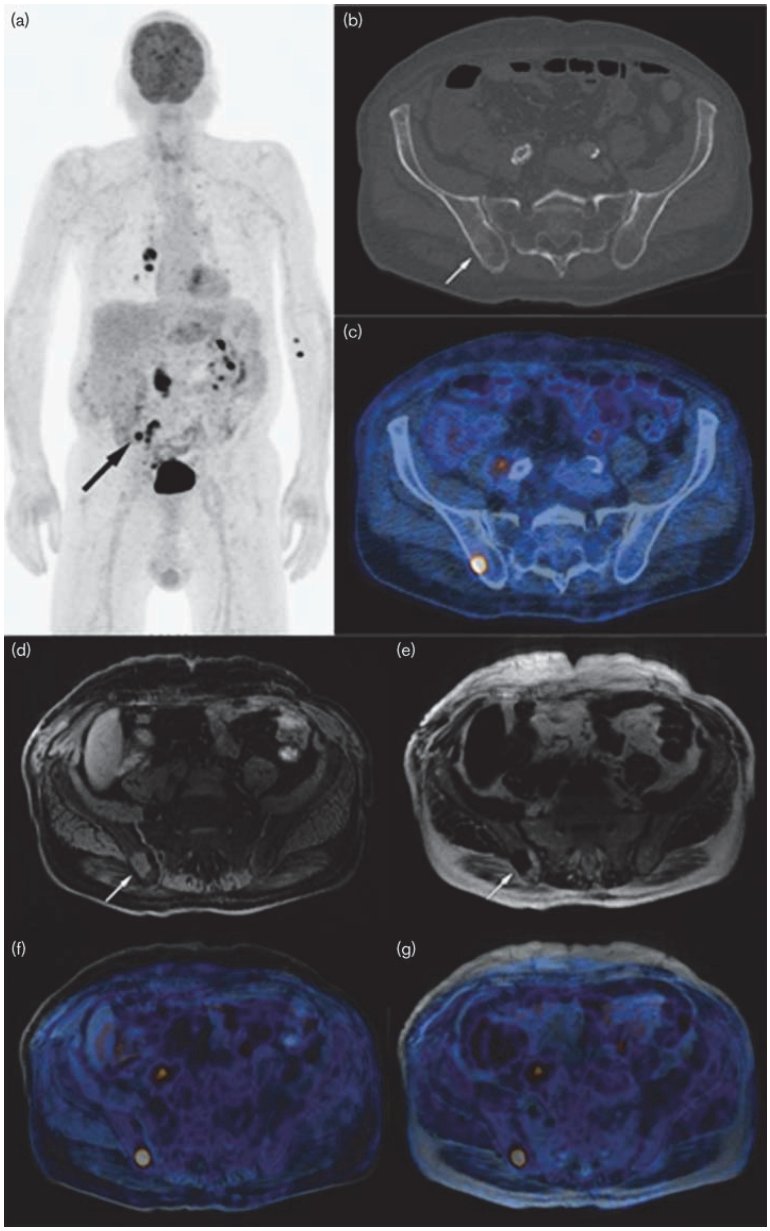

Male patient (64 years old) with metastatic carcinoma of the urethra. (a) Three-dimensional ^{18}F-FDG-PET image shows metastatic spread of the cancer. A single ^{18}F-FDG avid bone metastasis is present in the right iliac bone (black arrow). (b) On axial CT image, only the partially visible sclerotic lesion is seen in the corresponding location (white arrow) – such findings can be easily overseen when reading CT images prospectively. (c) Fused PET/CT axial image. (d, e) In contrast to the CT image, this single bone lesion is clearly depicted on axial MR images (white arrows) as a signal increase on the T1 water image (d) and as a signal drop on the T1 fat image (e) compared with the normal bone marrow. (f, g) Corresponding fused PET/MR images. In this case, PET/MR imaging provided higher reader confidence for the diagnosis of metastatic bone marrow involvement compared with the PET/CT imaging as a morphologic correlate for the ^{18}F-FDG avid bone lesion was clearly seen only on MR imaging. CT, computed tomography; ^{18}F-FDG, ^{18}F-fluorodeoxyglucose.

Fig. 2

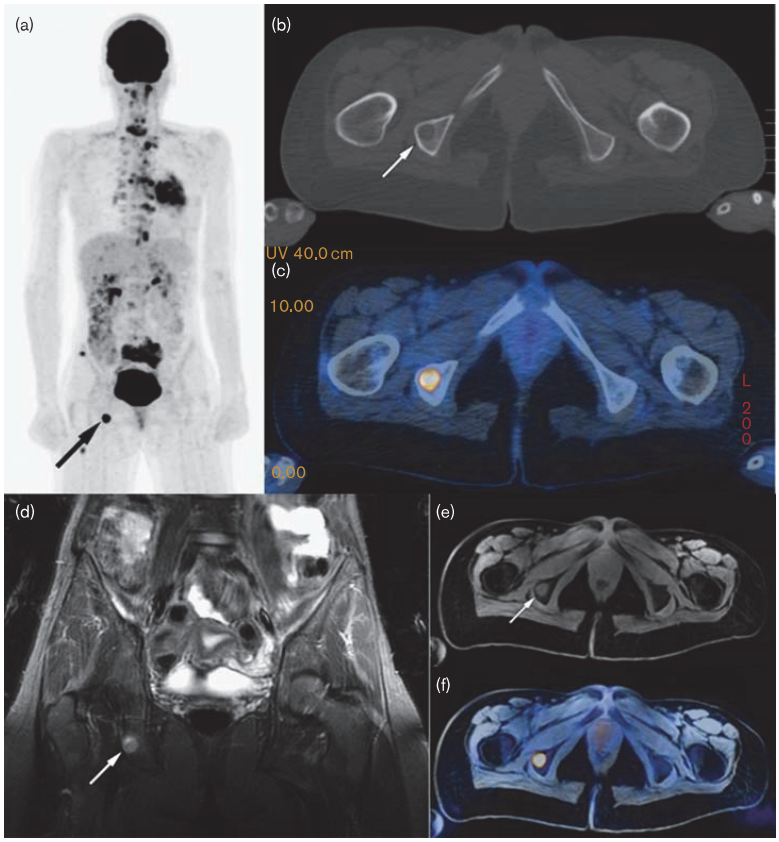

Female patient (43 years old) with adenocarcinoma of the lung. (a) Three-dimensional ^{18}F-FDG-PET image shows metastatic spread of the cancer. One of the multiple ^{18}F-FDG avid bone metastases is present in the right ischium (black arrow). (b) Axial CT image shows clear osteolysis in the corresponding location (white arrow). (c) Fused PET/CT axial image. (d) Coronal STIR MR image and (e) axial T1 water image clearly depict the lesion because of its high signal intensity (white arrows). (f) Corresponding axial fused PET/MR image. In this case, PET/CT and PET/MR imaging provided equal reader confidence for the diagnosis of metastatic bone marrow involvement as a morphologic correlate for the ^{18}F-FDG avid bone lesion was clearly seen on both CT and MR images. CT, computed tomography; ^{18}F-FDG, ^{18}F-fluorodeoxyglucose.

MR imaging. These patients either had several lesions seen on both modalities or had multiple disseminated lesions where the difference in the detection of single lesions did not lead to a change in overall reader confidence. Thus, in the seven studies in which all ^{18}F-FDG-positive bone lesions ($n = 9$) were seen only on the MR component, a significant increase was found in reader confidence for PET/MRI versus PET/CT.

Lesion conspicuity

In lesion-by-lesion analysis, PET/MR imaging provided better results in the detection of morphologic changes in the ^{18}F-FDG-positive bone lesions analysed: the mean lesion conspicuity was significantly better on T1 fat MR imaging compared with CT imaging ($P = 0.005$, Table 4). The overall lesion conspicuity on STIR-weighted MR images was similar to CT images.

Table 4 Comparison of lesions conspicuity scores between CT and MR images

Lesions' conspicuity	*P*-value
MR STIR vs. CT	0.496
MR T1 water vs. CT	0.516
MR T1 fat vs. CT	0.005[a]
MR T1 in-phase vs. CT	0.834
MR T1 out-phase vs. CT	0.069

CT, computed tomography; MR T1 water, fat, in-phase, out-phase, T1-weighted 3D dual-echo gradient-recalled echo pulse sequence, liver accelerated volume acquisition, corresponding water, fat, in-phase and out-phase reconstruction; MR STIR: short TI inversion recovery sequence.
[a]The mean lesion conspicuity was significantly higher on T1 fat MR imaging compared with CT imaging.

Table 5 Conspicuity scores (mean values) of the lesions on the basis of their CT density

	Lytic	Sclerotic	Nonvisible on CT
N of lesions (CT based)	48	17	21
CT score	3.08	3.18	0
MR STIR score	2.11	1.88	2.88
MR T1 water score	2.3	2.86	2.48
MR T1 fat score	2.77	3.37	3.52
MR T1 in-phase score	1.88	2.52	2.21
MR T1 out-phase score	2.53	3	3.05

CT, computed tomography; MR T1 water, fat, in-phase, out-phase, T1-weighted 3D dual-echo gradient-recalled echo pulse sequence, liver accelerated volume acquisition, corresponding water, fat, in-phase and out-phase reconstruction; MR STIR: short TI inversion recovery sequence.

In the subanalysis based on lesions density (on the CT-component), the mean conspicuity of neither lytic nor sclerotic lesions was significantly different on T1 fat MR imaging compared with CT imaging. However, the mean conspicuity of both sclerotic and lytic lesions was significantly higher on CT imaging compared with STIR MR imaging ($P = 0.014$ and 0.004, respectively). Further characteristics of this subanalysis are summarized in Tables 5 and 6.

In the 21 ^{18}F-FDG-positive bone lesions without a corresponding structural change visible in PET/CT imaging (65/86 were seen), the lesions were seen best in the T1 fat sequence of PET/MR imaging with a mean conspicuity of 3.52 and a mean size on T1 imaging of 19.5 mm. Further characteristics of these lesions are summarized in Table 7. The mean size of the ^{18}F-FDG-positive bone lesions was found to be significantly larger on T1-weighted MR images compared with CT images.

Discussion

In our study, we found that the overall detection rate of PET/CT and PET/MRI was the same on the basis of the ^{18}F-FDG positivity of the bone metastases evaluated here.

However, we could show that lesion conspicuity as well as reader confidence were improved in PET/MRI compared with PET/CT on the basis of the soft tissue contrast of the MR component. Furthermore, several morphological correlates were identified in PET/MRI that were not present in PET/CT.

Table 6 Comparison of sclerotic and lytic lesions conspicuity scores between CT and MR images

Lesions' conspicuity	*P*-value
Lytic lesions	
MR STIR vs. CT	0.004[a]
MR T1 fat vs. CT	0.309
Sclerotic lesions	
MR STIR vs. CT	0.014[b]
MR T1 fat vs. CT	0.425

CT, computed tomography; MR T1 water, fat, in-phase, out-phase, T1-weighted 3D dual-echo gradient-recalled echo pulse sequence, liver accelerated volume acquisition, corresponding water, fat, in-phase and out-phase reconstruction; MR STIR: short TI inversion recovery sequence.
[a,b]Mean conspicuity of both sclerotic and lytic lesions was significantly higher on CT imaging compared with STIR MR imaging.

Table 7 Metabolic and morphologic characteristics (mean values) of ^{18}F-FDG-positive bone lesions nonvisible on CT by location

	Thorax	Spine	Pelvis	Extremities	Total
N	2	7	6	6	21
Metabolic characteristics					
SUV_{max}	4.6	7.4	17.6	7.8	10.1
SUV_{mean}	2.2	4.3	8.3	4.9	5.4
Size (mm)					
MR T1 in-phase	17	18.3	28.5	13.7	19.5
Conspicuity, score					
MR STIR	1	2.3	3.7	3.7	2.9
MR T1 water	1	3.1	3.3	2.7	2.9
MR T1 fat	1	3.9	3	3.3	3.5
MR T1 in-phase	1	2.9	3	2.2	2.5
MR T1 out-phase	1	3.3	3.7	2.8	3.1

CT, computed tomography; ^{18}F-FDG, ^{18}F-fluorodeoxyglucose; MR T1 water, fat, in-phase, out-phase, T1-weighted 3D dual-echo gradient-recalled echo pulse sequence, liver accelerated volume acquisition, corresponding water, fat, in-phase and out-phase reconstruction; MR STIR: short TI inversion recovery sequence; SUV_{max}, maximum standardized uptake value; SUV_{mean}, mean standardized uptake value.

General

The superior soft tissue contrast and the consecutive ability to assess early metastatic infiltration of bone marrow make PET/MRI a promising modality in staging and response assessment in metastatic bony disease compared with PET/CT. However, compared with PET/CT as a standard of reference, PET/MRI as a new technology should have clear advantages in patient care and should ideally not place additional examination burden on the patients. There is a general workflow issue currently discussed in the literature with current PET/MRI protocols. Most of the protocols in such an early phase of a new modality are just 'normal' MR protocols that do not take into account the additional diagnostic information of the PET component. However, in our study, here, we evaluated a PET/MRI protocol that consists of three noncontrast sequences that allow for a whole-body PET/MRI approximately within the same time than a standard PET/CT [17].

Current literature

Our study suggests that one of the clinical scenarios where PET/MRI may be beneficial over PET/CT is an oncological patient with only few early bone metastases. In our series of patients, 25% of the lesions evaluated showed no definite morphological change in the bony structure on CT imaging whereas 95% of lesions had a clear morphological correlate on MR imaging. Although all these lesions were still detected because of their ^{18}F-FDG avidity, in cases of low metabolic activity (e.g. post-therapy), moving artefacts and small size, a pathological ^{18}F-FDG uptake in those lesions might not be very obvious. In this situation, the clear depiction of lesions on the MR component would ensure the detection of the lesions and correct distant staging of the

disease. This observation is supported by the recent work of Eiber *et al.* [18], who drew a similar conclusion .

The presence of ^{18}F-FDG-positive bone lesions on PET with negative findings at CT is not uncommon and is a known clinical issue. In the study by Taira *et al.* [15], 27% (31 out of 113) of ^{18}F-FDG-positive bone lesions analysed were found to be CT negative. In addition, MRI has been shown to find metastasis not visible on ^{18}F-FDG-PET or CT imaging [9]. In an early comparison, Antoch *et al.* [8] reported that MRI was more accurate in evaluating the bone structure for the presence of metastasis in a study comparing the staging accuracies of whole-body MRI and PET/CT. These finding were later supported in a study by Schmidt *et al.* [12], where whole-body MR imaging was found to have superior sensitivity and accuracy compared with PET/CT in the detection of bone metastases [12]. Therefore, in PET/MRI, even in cases of low ^{18}F-FDG activity, the likelihood of correct detection and staging seems to be higher than PET/CT. However, according to the results of our study, in patients with a high likelihood of metastatic bone disease, the use of PET/MRI would likely not result in improved diagnostic confidence as both PET/CT and PET/MRI would detect multiple lesions with no further therapeutic consequence.

Overall, we found an improved lesion conspicuity as well as higher reader confidence in the evaluation of PET/MRI compared with PET/CT. The lesion-by-lesion analysis showed that the highest lesion conspicuity was achieved by PET/MR imaging using the T1-weighted sequence highlighting the alterations in the bone marrow (T1 fat reconstruction). The significant increase in lesions conspicuity on MR imaging was mainly because of 21 ^{18}F-FDG-positive bone lesions not visible on CT imaging. These lesions likely represent bone marrow infiltration that have not yet resulted in considerable change in bone density but already changed signal in MR imaging [1]. Interestingly, the mean size of these lesions was quite substantial (19.5 mm). These results are partly in agreement with a recent study with a similar number of evaluated lesions [18]. There, PET/MRI with a T1-weighted sequence in addition to the Dixon-based AC sequence was superior in lesion delineation. Several differences have to be noted compared with our study. One of the reasons for the improved delineation in this additional T1-weighted sequence might be the higher matrix compared with the Dixon sequence. However, overall detection was not significantly different. Additional differences are that the PET/CT was partly performed with contrast media compared with a non-contrast PET/MRI. In our study, we strictly used non-contrast PET/CT for our comparison. An important aspect that was evaluated in our study was the reader confidence. Interestingly, although overall lesion detection was the same between PET/CT and PET/MRI, the additionally detectable lesions on the MRI component obviously support the diagnostic confidence for the reader – a fact that cannot be neglected in clinical routine reading, again, especially in lesions with low ^{18}F-FDG uptake.

Several studies have evaluated the important issue of differences in AC in PET imaging deriving from CT-based AC or MR-based AC. Phantom studies showed an increase in the relative error by up to 6.8% in the body and up to 31.0% for bony regions when the bones are ignored by the AC algorithm. In simulated clinical studies, the mean relative error may be as high 15% for body lesions and 30.7% for bony lesions [19]. Differences for the head and brain are lower [20]. These issues certainly have an impact on the detection of metastatic bone disease in simultaneous PET/MRI. These issues are even more pronounced when simulating therapy response, where it was found that simulated PET AC leads to a considerable underestimation of tracer uptake in bone lesions. The underestimation is dependent on the lesion composition with the largest error in sclerotic lesions [21]. As we used a trimodality set-up for our evaluation, we cannot compare or comment on those differences; however, this might be considered an advantage of the trimodality set-up for scientific comparisons where no underestimation can occur. Interestingly, in our patient population, the mean conspicuity of neither lytic nor sclerotic lesions was significantly different on T1 imaging compared with CT density. However, there was a difference in sclerotic and lytic lesions compared with STIR. This is remarkable, because usually – in MR imaging – fat-saturated T2 imaging is considered the ideal sequence to search for the major pathologies and especially bone lesions [22,23]. In PET/MRI (or PET/CT-MRI), the PET component is always available (no choice), but one has a choice which sequences are being used in the MR part of the examination. Thus, in the context of PET/MR, the sequences of choice might be different from those in MR imaging alone.

Limitation

The possible limitation of the study is that only ^{18}F-FDG-positive bone lesions were selected for the analysis. Thus, evaluation of benign lesions is not part of this study. Histological verification of ^{18}F-FDG-positive bone lesions was not always possible (and ethically not justifiable), but all patients had histological verification of their primary disease and the available imaging and clinical data were used to assess the analysed lesions on the basis of standard imaging criteria. We did not evaluate a possible clinical impact of PET/MR versus PET/CT in our patient population.

Conclusion

PET/MRI offers higher diagnostic confidence and an improved conspicuity in bone metastases compared with PET/CT. However, the overall detection rate was not

different. The highest possible clinical impact of PET/MRI appears to be in patients with limited early bone metastatic disease.

Acknowledgements

This research project was supported by an institutional research grant from GE Healthcare. Research by Andrei Samarin was supported by the European Union through the European Regional Development Fund.

Conflicts of interest

Patrick Veit-Haibach received IIS Grants from Bayer Healthcare, Siemens Medical Solutions, Roche Pharmaceutical and speaker fees from GE Healthcare. Gustav von Schulthess is a grant recipient from GE Healthcare and receives speaker fees from GE Healthcare. For the remaining authors there are no conflicts of interest.

References

1 Choi J, Raghavan M. Diagnostic imaging and image-guided therapy of skeletal metastases. *Cancer Control* 2012; **19**:102–112.
2 Lecouvet FE, Larbi A, Pasoglou V, Omoumi P, Tombal B, Michoux N, *et al.* MRI for response assessment in metastatic bone disease. *Eur Radiol* 2013; **23**:1986–1997.
3 Pace L, Nicolai E, Aiello M, Catalano O, Salvatore M. Whole-body PET/MRI in oncology: current status and clinical applications. *Clin Transl Imaging* 2013; **1**:31–44.
4 Engelhard K, Hollenbach HP, Wohlfart K, von Imhoff E, Fellner FA. Comparison of whole-body MRI with automatic moving table technique and bone scintigraphy for screening for bone metastases in patients with breast cancer. *Eur Radiol* 2004; **14**:99–105.
5 Mentzel HJ, Kentouche K, Sauner D, Fleischmann C, Vogt S, Gottschild D, *et al.* Comparison of whole-body STIR-MRI and ^{99m}Tc-methylene-diphosphonate scintigraphy in children with suspected multifocal bone lesions. *Eur Radiol* 2004; **14**:2297–2302.
6 Steinborn MM, Heuck AF, Tiling R, Bruegel M, Gauger L, Reiser MF. Whole-body bone marrow MRI in patients with metastatic disease to the skeletal system. *J Comput Assist Tomogr* 1999; **23**:123–129.
7 Yang HL, Liu T, Wang XM, Xu Y, Deng SM. Diagnosis of bone metastases: a meta-analysis comparing (1)(8)FDG PET, CT, MRI and bone scintigraphy. *Eur Radiol* 2011; **21**:2604–2617.
8 Antoch G, Vogt FM, Freudenberg LS, Nazaradeh F, Goehde SC, Barkhausen J, *et al.* Whole-body dual-modality PET/CT and whole-body MRI for tumor staging in oncology. *JAMA* 2003; **290**:3199–3206.
9 Ghanem NA, Pache G, Lohrmann C, Brink I, Bley T, Kotter E, *et al.* MRI and (18)FDG-PET in the assessment of bone marrow infiltration of the spine in cancer patients. *Eur Spine J* 2007; **16**:1907–1912.
10 Heusner T, Golitz P, Hamami M, Eberhardt W, Esser S, Forsting M, *et al.* "One-stop-shop" staging: should we prefer FDG-PET/CT or MRI for the detection of bone metastases? *Eur J Radiol* 2011; **78**:430–435.
11 Qu X, Huang X, Yan W, Wu L, Dai K. A meta-analysis of (1)(8)FDG-PET-CT, (1)(8)FDG-PET, MRI and bone scintigraphy for diagnosis of bone metastases in patients with lung cancer. *Eur J Radiol* 2012; **81**: 1007–1015.
12 Schmidt GP, Schoenberg SO, Schmid R, Stahl R, Tiling R, Becker CR, *et al.* Screening for bone metastases: whole-body MRI using a 32-channel system versus dual-modality PET-CT. *Eur Radiol* 2007; **17**:939–949.
13 Wu LM, Chen FY, Jiang XX, Gu HY, Yin Y, Xu JR. ^{18}F-FDG PET, combined FDG-PET/CT and MRI for evaluation of bone marrow infiltration in staging of lymphoma: a systematic review and meta-analysis. *Eur J Radiol* 2012; **81**:303–311.
14 Zamagni E, Nanni C, Patriarca F, Englaro E, Castellucci P, Geatti O, *et al.* A prospective comparison of ^{18}F-fluorodeoxyglucose positron emission tomography-computed tomography, magnetic resonance imaging and whole-body planar radiographs in the assessment of bone disease in newly diagnosed multiple myeloma. *Haematologica* 2007; **92**:50–55.
15 Taira AV, Herfkens RJ, Gambhir SS, Quon A. Detection of bone metastases: assessment of integrated FDG PET/CT imaging. *Radiology* 2007; **243**:204–211.
16 Kuhn FP, Crook DW, Mader CE, Appenzeller P, von Schulthess GK, Schmid DT. Discrimination and anatomical mapping of PET-positive lesions: comparison of CT attenuation-corrected PET images with coregistered MR and CT images in the abdomen. *Eur J Nucl Med Mol Imaging* 2013; **40**:44–51.
17 Huellner MW, Appenzeller P, Kuhn FP, Husmann L, Pietsch CM, Burger IA, *et al.* Whole-body nonenhanced PET/MR versus PET/CT in the staging and restaging of cancers: preliminary observations. *Radiology* 2014; **273**:859–869.
18 Eiber M, Takei T, Souvatzoglou M, Mayerhoefer ME, F yer S, Gaertner FC, *et al.* Performance of whole-body integrated 18F-FDG PET/MR in comparison to PET/CT for evaluation of malignant bone lesions. *J Nucl Med* 2014; **55**:191–197.
19 Akbarzadeh A, Ay MR, Ahmadian A, Alam NR, Zaidi H. MRI-guided attenuation correction in whole-body PET/MR: assessment of the effect of bone attenuation. *Ann Nucl Med* 2013; **27**:152–162.
20 Larsson A, Johansson A, Axelsson J, Nyholm T, Asklund T, Riklund K, Karlsson M. Evaluation of an attenuation correction method for PET/MR imaging of the head based on substitute CT images. *MAGMA* 2013; **26**:127–136.
21 Samarin A, Burger C, Wollenweber SD, Crook DW, Burger IA, Schmid DT, *et al.* PET/MR imaging of bone lesions – implications for PET quantification from imperfect attenuation correction. *Eur J Nucl Med Mol Imaging* 2012; **39**:1154–1160.
22 Vanel D, Casadei R, Alberghini M, Razgallah M, Busacca M, Albisinni U. MR imaging of bone metastases and choice of sequence: spin echo, in-phase gradient echo, diffusion, and contrast medium. *Semin Musculoskelet Radiol* 2009; **13**:97–103.
23 Vanel D, Dromain C, Tardivon A. MRI of bone marrow disorders. *Eur Radiol* 2000; **10**:224–229.

APPENDIX 2

ELULOOKIRJELDUS

1. Isikuandmed

Ees- ja perekonnanimi	Andrei Šamarin
Sünniaeg ja -koht	22.07.1979, Tallinn, Eesti
Kodakondsus	Eesti
E-posti aadress	andrei.samarin@regionaalhaigla.ee

2. Hariduskäik

Õppeasutus (nimetus lõpetamise ajal)	Lõpetamise aeg	Haridus (eriala/kraad)
Tallinna Tehnikaülikool	2016	Doktorantuur/PhD
Tartu Ülikool	2007	Radioloogia residentuur/ Radioloog
Tartu Ülikool	2003	Arstiteaduskond/Arst

3. Keelteoskus (alg-, kesk- või kõrgtase)

Keel	Tase
Vene	Emakeel
Eesti	Kõrgtase
Inglise	Kõrgtase
Saksa	Algtase

4. Täiendusõpe

Õppimise aeg	Täiendusõppe korraldaja nimetus
03/2013	University Hospital Zurich, Switzerland - scientific visit
02/2011 - 11/2011	University Hospital Zurich, Switzerland - PET/MR imaging research fellowship
02/2010 - 03/2010	University Hospital Zurich, Switzerland - PET/CT imaging clinical fellowship
11/2008 - 10/2009	University of Florida, Gainesville, USA – radiology fellowship
09/2005 - 10/2005	Armed Forces Institute of Pathology (AFIP), Washington, DC, USA - six week radiologic pathology correlation course

5. Teenistuskäik

Töötamise aeg	Tööandja nimetus	Ametikoht
Alates 2007	SA Põhja-Eesti Regionaalhaigla	Radioloog
Alates 2014	Tallinna Tehnikaülikool, Tehnomeedikum, Kardiovaskulaarse meditsiini instituut	Assistent
02/2011 - 11/2011	University Hospital Zurich, Switzerland	Teadur
2005–2007	SA Põhja-Eesti Regionaalhaigla	arst-resident
2003–2004	SA Tartu Ülikooli Kliinikum	arst-resident

6. Teadustegevus

Ainevahetuse ja morfoloogia hübriidkuvamine positronemissioontomograafia, magnetresonantstomograafia ja kompuutertomograafia abil

7. Artiklid rahvusvahelistes eelretsentseeritavates ajakirjades (ETIS 1.1):

1.) **Samarin A**, Hüllner M, Queiroz MA, Stolzmann P, Burger IA, von Schulthess G, Veit-Haibach P. 18F-FDG-PET/MR increases diagnostic confidence in detection of bone metastases compared with 18F-FDG-PET/CT. Nucl Med Commun. 2015 Dec; 36(12):1165-73
2.) Mamot C, Klingbiel D, Hitz F, Renner C, Pabst T, Driessen C, Mey U, Pless M, Bargetzi M, Krasniqi F, Gigli F, Hany T, **Samarin A**, Biaggi C, Rusterholz C, Dirnhofer S, Zucca E, Martinelli G. Final Results of a Prospective Evaluation of the Predictive Value of Interim Positron Emission Tomography in Patients With Diffuse Large B-Cell Lymphoma Treated With R-CHOP-14 (SAKK 38/07). J Clin Oncol. 2015 Aug 10;33(23):2523-9.
3.) **Samarin A**, Kuhn FP, Brandsberg F, von Schulthess G, Burger IA. Image registration accuracy of an in-house developed patient transport system for PET/CT+MR and SPECT+CT imaging. Nucl Med Commun. 2015 Feb;36(2):194-200.
4.) Burger IA, Schwarz EI, **Samarin A**, Breitenstein S, Weber A, Hany TF. Correlation between therapy response assessment using FDG PET/CT and histopathologic tumor regression grade in hepatic metastasis of colorectal carcinoma after neoadjuvant therapy. Ann Nucl Med. 2013 Feb;27(2):177-83
5.) **Samarin A**, Burger C, Wollenweber SD et al. PET/MR imaging of bone lesions – implications for PET quantification from imperfect attenuation correction. Eur J Nucl Med Mol Imaging (2012) 39:1154-1160

APPENDIX 3

CURRICULUM VITAE

1. Personal data

Name	Andrei Šamarin
Date and place of birth	22.07.1979
E-mail address	andrei.samarin@regionaalhaigla.ee

2. Education

Educational institution	Graduation year	Education (field of study/degree)
Tallinn University of Technology	2016	Doctoral study/ PhD
Tartu University	2007	Radiology residency /Radiologist
Tartu University	2003	Faculty of Medicine/ MD

3. Language competence/skills (fluent, average, basic skills)

Language	Level
Russian	Native language
Estonian	Fluent
English	Fluent
German	Basic skills

4. Special courses

Period	Educational or other organisation
03/2013	University Hospital Zurich, Switzerland - scientific visit
02/2011 - 11/2011	University Hospital Zurich, Switzerland - PET/MR imaging research fellowship
02/2010 - 03/2010	University Hospital Zurich, Switzerland - PET/CT imaging clinical fellowship
11/2008 - 10/2009	University of Florida, Gainesville, USA – radiology fellowship
09/2005 - 10/2005	Armed Forces Institute of Pathology (AFIP), Washington, DC, USA - six week radiologic pathology correlation course

5. Professional employment

Period	Organisation	Position
Since 2007	North Estonia Medical Centre Foundation	Radiologist
Since 2014	Tallinn University of Technology, Technomedicum of TUT, Centre of Cardiology	Assistant
02/2011 - 11/2011	University Hospital Zurich, Switzerland	Research fellow
2005–2007	North Estonia Medical Centre Foundation	radiology resident
2003–2004	Tartu University Hospital	radiology resident

6. Research activity

Hybrid PET/MR and PET/CT imaging of metabolism and morphology

7. Publications in international peer-reviewed journals (ETIS 1.1):

1.) **Samarin A**, Hüllner M, Queiroz MA, Stolzmann P, Burger IA, von Schulthess G, Veit-Haibach P. 18F-FDG-PET/MR increases diagnostic confidence in detection of bone metastases compared with 18F-FDG-PET/CT. Nucl Med Commun. 2015 Dec; 36(12):1165-73
2.) Mamot C, Klingbiel D, Hitz F, Renner C, Pabst T, Driessen C, Mey U, Pless M, Bargetzi M, Krasniqi F, Gigli F, Hany T, **Samarin A**, Biaggi C, Rusterholz C, Dirnhofer S, Zucca E, Martinelli G. Final Results of a Prospective Evaluation of the Predictive Value of Interim Positron Emission Tomography in Patients With Diffuse Large B-Cell Lymphoma Treated With R-CHOP-14 (SAKK 38/07). J Clin Oncol. 2015 Aug 10;33(23):2523-9.
3.) **Samarin A**, Kuhn FP, Brandsberg F, von Schulthess G, Burger IA. Image registration accuracy of an in-house developed patient transport system for PET/CT+MR and SPECT+CT imaging. Nucl Med Commun. 2015 Feb;36(2):194-200.
4.) Burger IA, Schwarz EI, **Samarin A**, Breitenstein S, Weber A, Hany TF. Correlation between therapy response assessment using FDG PET/CT and histopathologic tumor regression grade in hepatic metastasis of colorectal carcinoma after neoadjuvant therapy. Ann Nucl Med. 2013 Feb;27(2):177-83
5.) **Samarin A**, Burger C, Wollenweber SD et al. PET/MR imaging of bone lesions – implications for PET quantification from imperfect attenuation correction. Eur J Nucl Med Mol Imaging (2012) 39:1154-1160

DISSERTATIONS DEFENDED AT
TALLINN UNIVERSITY OF TECHNOLOGY ON
NATURAL AND EXACT SCIENCES

1. **Olav Kongas**. Nonlinear Dynamics in Modeling Cardiac Arrhytmias. 1998.
2. **Kalju Vanatalu**. Optimization of Processes of Microbial Biosynthesis of Isotopically Labeled Biomolecules and Their Complexes. 1999.
3. **Ahto Buldas**. An Algebraic Approach to the Structure of Graphs. 1999.
4. **Monika Drews**. A Metabolic Study of Insect Cells in Batch and Continuous Culture: Application of Chemostat and Turbidostat to the Production of Recombinant Proteins. 1999.
5. **Eola Valdre**. Endothelial-Specific Regulation of Vessel Formation: Role of Receptor Tyrosine Kinases. 2000.
6. **Kalju Lott**. Doping and Defect Thermodynamic Equilibrium in ZnS. 2000.
7. **Reet Koljak**. Novel Fatty Acid Dioxygenases from the Corals *Plexaura homomalla* and *Gersemia fruticosa.* 2001.
8. **Anne Paju**. Asymmetric oxidation of Prochiral and Racemic Ketones by Using Sharpless Catalyst. 2001.
9. **Marko Vendelin**. Cardiac Mechanoenergetics *in silico*. 2001.
10. **Pearu Peterson**. Multi-Soliton Interactions and the Inverse Problem of Wave Crest. 2001.
11. **Anne Menert**. Microcalorimetry of Anaerobic Digestion. 2001.
12. **Toomas Tiivel**. The Role of the Mitochondrial Outer Membrane in *in vivo* Regulation of Respiration in Normal Heart and Skeletal Muscle Cell. 2002.
13. **Olle Hints**. Ordovician Scolecodonts of Estonia and Neighbouring Areas: Taxonomy, Distribution, Palaeoecology, and Application. 2002.
14. **Jaak Nõlvak**. Chitinozoan Biostratigrapy in the Ordovician of Baltoscandia. 2002.
15. **Liivi Kluge**. On Algebraic Structure of Pre-Operad. 2002.
16. **Jaanus Lass**. Biosignal Interpretation: Study of Cardiac Arrhytmias and Electromagnetic Field Effects on Human Nervous System. 2002.
17. **Janek Peterson**. Synthesis, Structural Characterization and Modification of PAMAM Dendrimers. 2002.
18. **Merike Vaher**. Room Temperature Ionic Liquids as Background Electrolyte Additives in Capillary Electrophoresis. 2002.
19. **Valdek Mikli**. Electron Microscopy and Image Analysis Study of Powdered Hardmetal Materials and Optoelectronic Thin Films. 2003.
20. **Mart Viljus**. The Microstructure and Properties of Fine-Grained Cermets. 2003.
21. **Signe Kask**. Identification and Characterization of Dairy-Related *Lactobacillus.* 2003.
22. **Tiiu-Mai Laht**. Influence of Microstructure of the Curd on Enzymatic and Microbiological Processes in Swiss-Type Cheese. 2003.
23. **Anne Kuusksalu**. 2–5A Synthetase in the Marine Sponge *Geodia cydonium*. 2003.
24. **Sergei Bereznev**. Solar Cells Based on Polycristalline Copper-Indium Chalcogenides and Conductive Polymers. 2003.

25. **Kadri Kriis**. Asymmetric Synthesis of C_2-Symmetric Bimorpholines and Their Application as Chiral Ligands in the Transfer Hydrogenation of Aromatic Ketones. 2004.
26. **Jekaterina Reut**. Polypyrrole Coatings on Conducting and Insulating Substracts. 2004.
27. **Sven Nõmm**. Realization and Identification of Discrete-Time Nonlinear Systems. 2004.
28. **Olga Kijatkina**. Deposition of Copper Indium Disulphide Films by Chemical Spray Pyrolysis. 2004.
29. **Gert Tamberg**. On Sampling Operators Defined by Rogosinski, Hann and Blackman Windows. 2004.
30. **Monika Übner**. Interaction of Humic Substances with Metal Cations. 2004.
31. **Kaarel Adamberg**. Growth Characteristics of Non-Starter Lactic Acid Bacteria from Cheese. 2004.
32. **Imre Vallikivi**. Lipase-Catalysed Reactions of Prostaglandins. 2004.
33. **Merike Peld**. Substituted Apatites as Sorbents for Heavy Metals. 2005.
34. **Vitali Syritski**. Study of Synthesis and Redox Switching of Polypyrrole and Poly(3,4-ethylenedioxythiophene) by Using *in-situ* Techniques. 2004.
35. **Lee Põllumaa**. Evaluation of Ecotoxicological Effects Related to Oil Shale Industry. 2004.
36. **Riina Aav**. Synthesis of 9,11-Secosterols Intermediates. 2005.
37. **Andres Braunbrück**. Wave Interaction in Weakly Inhomogeneous Materials. 2005.
38. **Robert Kitt**. Generalised Scale-Invariance in Financial Time Series. 2005.
39. **Juss Pavelson**. Mesoscale Physical Processes and the Related Impact on the Summer Nutrient Fields and Phytoplankton Blooms in the Western Gulf of Finland. 2005.
40. **Olari Ilison**. Solitons and Solitary Waves in Media with Higher Order Dispersive and Nonlinear Effects. 2005.
41. **Maksim Säkki**. Intermittency and Long-Range Structurization of Heart Rate. 2005.
42. **Enli Kiipli**. Modelling Seawater Chemistry of the East Baltic Basin in the Late Ordovician–Early Silurian. 2005.
43. **Igor Golovtsov**. Modification of Conductive Properties and Processability of Polyparaphenylene, Polypyrrole and polyaniline. 2005.
44. **Katrin Laos**. Interaction Between Furcellaran and the Globular Proteins (Bovine Serum Albumin β-Lactoglobulin). 2005.
45. **Arvo Mere**. Structural and Electrical Properties of Spray Deposited Copper Indium Disulphide Films for Solar Cells. 2006.
46. **Sille Ehala**. Development and Application of Various On- and Off-Line Analytical Methods for the Analysis of Bioactive Compounds. 2006.
47. **Maria Kulp**. Capillary Electrophoretic Monitoring of Biochemical Reaction Kinetics. 2006.
48. **Anu Aaspõllu.** Proteinases from *Vipera lebetina* Snake Venom Affecting Hemostasis. 2006.
49. **Lyudmila Chekulayeva**. Photosensitized Inactivation of Tumor Cells by Porphyrins and Chlorins. 2006.

50. **Merle Uudsemaa**. Quantum-Chemical Modeling of Solvated First Row Transition Metal Ions. 2006.
51. **Tagli Pitsi**. Nutrition Situation of Pre-School Children in Estonia from 1995 to 2004. 2006.
52. **Angela Ivask**. Luminescent Recombinant Sensor Bacteria for the Analysis of Bioavailable Heavy Metals. 2006.
53. **Tiina Lõugas**. Study on Physico-Chemical Properties and Some Bioactive Compounds of Sea Buckthorn (*Hippophae rhamnoides* L.). 2006.
54. **Kaja Kasemets**. Effect of Changing Environmental Conditions on the Fermentative Growth of *Saccharomyces cerevisae* S288C: Auxo-accelerostat Study. 2006.
55. **Ildar Nisamedtinov**. Application of ^{13}C and Fluorescence Labeling in Metabolic Studies of *Saccharomyces* spp. 2006.
56. **Alar Leibak**. On Additive Generalisation of Voronoï's Theory of Perfect Forms over Algebraic Number Fields. 2006.
57. **Andri Jagomägi**. Photoluminescence of Chalcopyrite Tellurides. 2006.
58. **Tõnu Martma**. Application of Carbon Isotopes to the Study of the Ordovician and Silurian of the Baltic. 2006.
59. **Marit Kauk**. Chemical Composition of $CuInSe_2$ Monograin Powders for Solar Cell Application. 2006.
60. **Julia Kois**. Electrochemical Deposition of $CuInSe_2$ Thin Films for Photovoltaic Applications. 2006.
61. **Ilona Oja Açik**. Sol-Gel Deposition of Titanium Dioxide Films. 2007.
62. **Tiia Anmann**. Integrated and Organized Cellular Bioenergetic Systems in Heart and Brain. 2007.
63. **Katrin Trummal**. Purification, Characterization and Specificity Studies of Metalloproteinases from *Vipera lebetina* Snake Venom. 2007.
64. **Gennadi Lessin**. Biochemical Definition of Coastal Zone Using Numerical Modeling and Measurement Data. 2007.
65. **Enno Pais**. Inverse problems to determine non-homogeneous degenerate memory kernels in heat flow. 2007.
66. **Maria Borissova**. Capillary Electrophoresis on Alkylimidazolium Salts. 2007.
67. **Karin Valmsen**. Prostaglandin Synthesis in the Coral *Plexaura homomalla*: Control of Prostaglandin Stereochemistry at Carbon 15 by Cyclooxygenases. 2007.
68. **Kristjan Piirimäe**. Long-Term Changes of Nutrient Fluxes in the Drainage Basin of the Gulf of Finland – Application of the PolFlow Model. 2007.
69. **Tatjana Dedova**. Chemical Spray Pyrolysis Deposition of Zinc Sulfide Thin Films and Zinc Oxide Nanostructured Layers. 2007.
70. **Katrin Tomson**. Production of Labelled Recombinant Proteins in Fed-Batch Systems in *Escherichia coli*. 2007.
71. **Cecilia Sarmiento**. Suppressors of RNA Silencing in Plants. 2008.
72. **Vilja Mardla**. Inhibition of Platelet Aggregation with Combination of Antiplatelet Agents. 2008.
73. **Maie Bachmann**. Effect of Modulated Microwave Radiation on Human Resting Electroencephalographic Signal. 2008.
74. **Dan Hüvonen**. Terahertz Spectroscopy of Low-Dimensional Spin Systems. 2008.

75. **Ly Villo**. Stereoselective Chemoenzymatic Synthesis of Deoxy Sugar Esters Involving *Candida antarctica* Lipase B. 2008.
76. **Johan Anton**. Technology of Integrated Photoelasticity for Residual Stress Measurement in Glass Articles of Axisymmetric Shape. 2008.
77. **Olga Volobujeva**. SEM Study of Selenization of Different Thin Metallic Films. 2008.
78. **Artur Jõgi**. Synthesis of 4'-Substituted 2,3'-dideoxynucleoside Analogues. 2008.
79. **Mario Kadastik**. Doubly Charged Higgs Boson Decays and Implications on Neutrino Physics. 2008.
80. **Fernando Pérez-Caballero**. Carbon Aerogels from 5-Methylresorcinol-Formaldehyde Gels. 2008.
81. **Sirje Vaask**. The Comparability, Reproducibility and Validity of Estonian Food Consumption Surveys. 2008.
82. **Anna Menaker**. Electrosynthesized Conducting Polymers, Polypyrrole and Poly(3,4-ethylenedioxythiophene), for Molecular Imprinting. 2009.
83. **Lauri Ilison**. Solitons and Solitary Waves in Hierarchical Korteweg-de Vries Type Systems. 2009.
84. **Kaia Ernits**. Study of In_2S_3 and ZnS Thin Films Deposited by Ultrasonic Spray Pyrolysis and Chemical Deposition. 2009.
85. **Veljo Sinivee**. Portable Spectrometer for Ionizing Radiation "Gammamapper". 2009.
86. **Jüri Virkepu**. On Lagrange Formalism for Lie Theory and Operadic Harmonic Oscillator in Low Dimensions. 2009.
87. **Marko Piirsoo**. Deciphering Molecular Basis of Schwann Cell Development. 2009.
88. **Kati Helmja**. Determination of Phenolic Compounds and Their Antioxidative Capability in Plant Extracts. 2010.
89. **Merike Sõmera**. Sobemoviruses: Genomic Organization, Potential for Recombination and Necessity of P1 in Systemic Infection. 2010.
90. **Kristjan Laes**. Preparation and Impedance Spectroscopy of Hybrid Structures Based on $CuIn_3Se_5$ Photoabsorber. 2010.
91. **Kristin Lippur**. Asymmetric Synthesis of 2,2'-Bimorpholine and its 5,5'-Substituted Derivatives. 2010.
92. **Merike Luman**. Dialysis Dose and Nutrition Assessment by an Optical Method. 2010.
93. **Mihhail Berezovski**. Numerical Simulation of Wave Propagation in Heterogeneous and Microstructured Materials. 2010.
94. **Tamara Aid-Pavlidis**. Structure and Regulation of BDNF Gene. 2010.
95. **Olga Bragina**. The Role of Sonic Hedgehog Pathway in Neuro- and Tumorigenesis. 2010.
96. **Merle Randrüüt**. Wave Propagation in Microstructured Solids: Solitary and Periodic Waves. 2010.
97. **Marju Laars**. Asymmetric Organocatalytic Michael and Aldol Reactions Mediated by Cyclic Amines. 2010.
98. **Maarja Grossberg**. Optical Properties of Multinary Semiconductor Compounds for Photovoltaic Applications. 2010.

99. **Alla Maloverjan**. Vertebrate Homologues of Drosophila Fused Kinase and Their Role in Sonic Hedgehog Signalling Pathway. 2010.
100. **Priit Pruunsild**. Neuronal Activity-Dependent Transcription Factors and Regulation of Human *BDNF* Gene. 2010.
101. **Tatjana Knjazeva**. New Approaches in Capillary Electrophoresis for Separation and Study of Proteins. 2011.
102. **Atanas Katerski**. Chemical Composition of Sprayed Copper Indium Disulfide Films for Nanostructured Solar Cells. 2011.
103. **Kristi Timmo.** Formation of Properties of $CuInSe_2$ and $Cu_2ZnSn(S,Se)_4$ Monograin Powders Synthesized in Molten KI. 2011.
104. **Kert Tamm**. Wave Propagation and Interaction in Mindlin-Type Microstructured Solids: Numerical Simulation. 2011.
105. **Adrian Popp**. Ordovician Proetid Trilobites in Baltoscandia and Germany. 2011.
106. **Ove Pärn**. Sea Ice Deformation Events in the Gulf of Finland and This Impact on Shipping. 2011.
107. **Germo Väli**. Numerical Experiments on Matter Transport in the Baltic Sea. 2011.
108. **Andrus Seiman**. Point-of-Care Analyser Based on Capillary Electrophoresis. 2011.
109. **Olga Katargina**. Tick-Borne Pathogens Circulating in Estonia (Tick-Borne Encephalitis Virus, *Anaplasma phagocytophilum*, *Babesia* Species): Their Prevalence and Genetic Characterization. 2011.
110. **Ingrid Sumeri**. The Study of Probiotic Bacteria in Human Gastrointestinal Tract Simulator. 2011.
111. **Kairit Zovo**. Functional Characterization of Cellular Copper Proteome. 2011.
112. **Natalja Makarytsheva**. Analysis of Organic Species in Sediments and Soil by High Performance Separation Methods. 2011.
113. **Monika Mortimer**. Evaluation of the Biological Effects of Engineered Nanoparticles on Unicellular Pro- and Eukaryotic Organisms. 2011.
114. **Kersti Tepp**. Molecular System Bioenergetics of Cardiac Cells: Quantitative Analysis of Structure-Function Relationship. 2011.
115. **Anna-Liisa Peikolainen**. Organic Aerogels Based on 5-Methylresorcinol. 2011.
116. **Leeli Amon**. Palaeoecological Reconstruction of Late-Glacial Vegetation Dynamics in Eastern Baltic Area: A View Based on Plant Macrofossil Analysis. 2011.
117. **Tanel Peets**. Dispersion Analysis of Wave Motion in Microstructured Solids. 2011.
118. **Liina Kaupmees**. Selenization of Molybdenum as Contact Material in Solar Cells. 2011.
119. **Allan Olspert**. Properties of VPg and Coat Protein of Sobemoviruses. 2011.
120. **Kadri Koppel**. Food Category Appraisal Using Sensory Methods. 2011.
121. **Jelena Gorbatšova**. Development of Methods for CE Analysis of Plant Phenolics and Vitamins. 2011.
122. **Karin Viipsi**. Impact of EDTA and Humic Substances on the Removal of Cd and Zn from Aqueous Solutions by Apatite. 2012.

123. **David Schryer**. Metabolic Flux Analysis of Compartmentalized Systems Using Dynamic Isotopologue Modeling. 2012.
124. **Ardo Illaste**. Analysis of Molecular Movements in Cardiac Myocytes. 2012.
125. **Indrek Reile**. 3-Alkylcyclopentane-1,2-Diones in Asymmetric Oxidation and Alkylation Reactions. 2012.
126. **Tatjana Tamberg**. Some Classes of Finite 2-Groups and Their Endomorphism Semigroups. 2012.
127. **Taavi Liblik**. Variability of Thermohaline Structure in the Gulf of Finland in Summer. 2012.
128. **Priidik Lagemaa**. Operational Forecasting in Estonian Marine Waters. 2012.
129. **Andrei Errapart**. Photoelastic Tomography in Linear and Non-linear Approximation. 2012.
130. **Külliki Krabbi**. Biochemical Diagnosis of Classical Galactosemia and Mucopolysaccharidoses in Estonia. 2012.
131. **Kristel Kaseleht**. Identification of Aroma Compounds in Food using SPME-GC/MS and GC-Olfactometry. 2012.
132. **Kristel Kodar**. Immunoglobulin G Glycosylation Profiling in Patients with Gastric Cancer. 2012.
133. **Kai Rosin**. Solar Radiation and Wind as Agents of the Formation of the Radiation Regime in Water Bodies. 2012.
134. **Ann Tiiman**. Interactions of Alzheimer's Amyloid-Beta Peptides with Zn(II) and Cu(II) Ions. 2012.
135. **Olga Gavrilova**. Application and Elaboration of Accounting Approaches for Sustainable Development. 2012.
136. **Olesja Bondarenko**. Development of Bacterial Biosensors and Human Stem Cell-Based *In Vitro* Assays for the Toxicological Profiling of Synthetic Nanoparticles. 2012.
137. **Katri Muska**. Study of Composition and Thermal Treatments of Quaternary Compounds for Monograin Layer Solar Cells. 2012.
138. **Ranno Nahku**. Validation of Critical Factors for the Quantitative Characterization of Bacterial Physiology in Accelerostat Cultures. 2012.
139. **Petri-Jaan Lahtvee**. Quantitative Omics-level Analysis of Growth Rate Dependent Energy Metabolism in *Lactococcus lactis*. 2012.
140. **Kerti Orumets**. Molecular Mechanisms Controlling Intracellular Glutathione Levels in Baker's Yeast *Saccharomyces cerevisiae* and its Random Mutagenized Glutathione Over-Accumulating Isolate. 2012.
141. **Loreida Timberg**. Spice-Cured Sprats Ripening, Sensory Parameters Development, and Quality Indicators. 2012.
142. **Anna Mihhalevski**. Rye Sourdough Fermentation and Bread Stability. 2012.
143. **Liisa Arike**. Quantitative Proteomics of *Escherichia coli*: From Relative to Absolute Scale. 2012.
144. **Kairi Otto**. Deposition of In_2S_3 Thin Films by Chemical Spray Pyrolysis. 2012.
145. **Mari Sepp**. Functions of the Basic Helix-Loop-Helix Transcription Factor TCF4 in Health and Disease. 2012.
146. **Anna Suhhova**. Detection of the Effect of Weak Stressors on Human Resting Electroencephalographic Signal. 2012.

147. **Aram Kazarjan**. Development and Production of Extruded Food and Feed Products Containing Probiotic Microorganisms. 2012.
148. **Rivo Uiboupin**. Application of Remote Sensing Methods for the Investigation of Spatio-Temporal Variability of Sea Surface Temperature and Chlorophyll Fields in the Gulf of Finland. 2013.
149. **Tiina Kriščiunaite**. A Study of Milk Coagulability. 2013.
150. **Tuuli Levandi**. Comparative Study of Cereal Varieties by Analytical Separation Methods and Chemometrics. 2013.
151. **Natalja Kabanova**. Development of a Microcalorimetric Method for the Study of Fermentation Processes. 2013.
152. **Himani Khanduri**. Magnetic Properties of Functional Oxides. 2013.
153. **Julia Smirnova**. Investigation of Properties and Reaction Mechanisms of Redox-Active Proteins by ESI MS. 2013.
154. **Mervi Sepp**. Estimation of Diffusion Restrictions in Cardiomyocytes Using Kinetic Measurements. 2013.
155. **Kersti Jääger**. Differentiation and Heterogeneity of Mesenchymal Stem Cells. 2013.
156. **Victor Alari**. Multi-Scale Wind Wave Modeling in the Baltic Sea. 2013.
157. **Taavi Päll**. Studies of CD44 Hyaluronan Binding Domain as Novel Angiogenesis Inhibitor. 2013.
158. **Allan Niidu**. Synthesis of Cyclopentane and Tetrahydrofuran Derivatives. 2013.
159. **Julia Geller**. Detection and Genetic Characterization of *Borrelia* Species Circulating in Tick Population in Estonia. 2013.
160. **Irina Stulova**. The Effects of Milk Composition and Treatment on the Growth of Lactic Acid Bacteria. 2013.
161. **Jana Holmar**. Optical Method for Uric Acid Removal Assessment During Dialysis. 2013.
162. **Kerti Ausmees**. Synthesis of Heterobicyclo[3.2.0]heptane Derivatives *via* Multicomponent Cascade Reaction. 2013.
163. **Minna Varikmaa**. Structural and Functional Studies of Mitochondrial Respiration Regulation in Muscle Cells. 2013.
164. **Indrek Koppel**. Transcriptional Mechanisms of BDNF Gene Regulation. 2014.
165. **Kristjan Pilt**. Optical Pulse Wave Signal Analysis for Determination of Early Arterial Ageing in Diabetic Patients. 2014.
166. **Andres Anier**. Estimation of the Complexity of the Electroencephalogram for Brain Monitoring in Intensive Care. 2014.
167. **Toivo Kallaste**. Pyroclastic Sanidine in the Lower Palaeozoic Bentonites – A Tool for Regional Geological Correlations. 2014.
168. **Erki Kärber**. Properties of ZnO-nanorod/In_2S_3/$CuInS_2$ Solar Cell and the Constituent Layers Deposited by Chemical Spray Method. 2014.
169. **Julia Lehner**. Formation of Cu_2ZnSnS_4 and $Cu_2ZnSnSe_4$ by Chalcogenisation of Electrochemically Deposited Precursor Layers. 2014.
170. **Peep Pitk**. Protein- and Lipid-rich Solid Slaughterhouse Waste Anaerobic Co-digestion: Resource Analysis and Process Optimization. 2014.
171. **Kaspar Valgepea**. Absolute Quantitative Multi-omics Characterization of Specific Growth Rate-dependent Metabolism of *Escherichia coli*. 2014.

172. **Artur Noole**. Asymmetric Organocatalytic Synthesis of 3,3'-Disubstituted Oxindoles. 2014.
173. **Robert Tsanev**. Identification and Structure-Functional Characterisation of the Gene Transcriptional Repressor Domain of Human Gli Proteins. 2014.
174. **Dmitri Kartofelev**. Nonlinear Sound Generation Mechanisms in Musical Acoustic. 2014.
175. **Sigrid Hade**. GIS Applications in the Studies of the Palaeozoic Graptolite Argillite and Landscape Change. 2014.
176. **Agne Velthut-Meikas**. Ovarian Follicle as the Environment of Oocyte Maturation: The Role of Granulosa Cells and Follicular Fluid at Pre-Ovulatory Development. 2014.
177. **Kristel Hälvin**. Determination of B-group Vitamins in Food Using an LC-MS Stable Isotope Dilution Assay. 2014.
178. **Mailis Päri**. Characterization of the Oligoadenylate Synthetase Subgroup from Phylum Porifera. 2014.
179. **Jekaterina Kazantseva**. Alternative Splicing of *TAF4*: A Dynamic Switch between Distinct Cell Functions. 2014.
180. **Jaanus Suurväli**. Regulator of G Protein Signalling 16 (RGS16): Functions in Immunity and Genomic Location in an Ancient MHC-Related Evolutionarily Conserved Synteny Group. 2014.
181. **Ene Viiard**. Diversity and Stability of Lactic Acid Bacteria During Rye Sourdough Propagation. 2014.
182. **Kristella Hansen**. Prostaglandin Synthesis in Marine Arthropods and Red Algae. 2014.
183. **Helike Lõhelaid**. Allene Oxide Synthase-lipoxygenase Pathway in Coral Stress Response. 2015.
184. **Normunds Stivrinš**. Postglacial Environmental Conditions, Vegetation Succession and Human Impact in Latvia. 2015.
185. **Mary-Liis Kütt**. Identification and Characterization of Bioactive Peptides with Antimicrobial and Immunoregulating Properties Derived from Bovine Colostrum and Milk. 2015.
186. **Kazbulat Šogenov**. Petrophysical Models of the CO_2 Plume at Prospective Storage Sites in the Baltic Basin. 2015.
187. **Taavi Raadik**. Application of Modulation Spectroscopy Methods in Photovoltaic Materials Research. 2015.
188. **Reio Põder**. Study of Oxygen Vacancy Dynamics in Sc-doped Ceria with NMR Techniques. 2015.
189. **Sven Siir**. Internal Geochemical Stratification of Bentonites (Altered Volcanic Ash Beds) and its Interpretation. 2015.
190. **Kaur Jaanson**. Novel Transgenic Models Based on Bacterial Artificial Chromosomes for Studying BDNF Gene Regulation. 2015.
191. **Niina Karro**. Analysis of ADP Compartmentation in Cardiomyocytes and Its Role in Protection Against Mitochondrial Permeability Transition Pore Opening. 2015.
192. **Piret Laht**. B-plexins Regulate the Maturation of Neurons Through Microtubule Dynamics. 2015.
193. **Sergei Žari**. Organocatalytic Asymmetric Addition to Unsaturated 1,4-Dicarbonyl Compounds. 2015.

194. **Natalja Buhhalko**. Processes Influencing the Spatio-temporal Dynamics of Nutrients and Phytoplankton in Summer in the Gulf of Finland, Baltic Sea. 2015.
195. **Natalia Maticiuc**. Mechanism of Changes in the Properties of Chemically Deposited CdS Thin Films Induced by Thermal Annealing. 2015.
196. **Mario Öeren**. Computational Study of Cyclohexylhemicucurbiturils. 2015.
197. **Mari Kalda**. Mechanoenergetics of a Single Cardiomyocyte. 2015.
198. **Ieva Grudzinska**. Diatom Stratigraphy and Relative Sea Level Changes of the Eastern Baltic Sea over the Holocene. 2015.
199. **Anna Kazantseva**. Alternative Splicing in Health and Disease. 2015.
200. **Jana Kazarjan**. Investigation of Endogenous Antioxidants and Their Synthetic Analogues by Capillary Electrophoresis. 2016.
201. **Maria Safonova**. SnS Thin Films Deposition by Chemical Solution Method and Characterization. 2016.
202. **Jekaterina Mazina**. Detection of Psycho- and Bioactive Drugs in Different Sample Matrices by Fluorescence Spectroscopy and Capillary Electrophoresis. 2016.
203. **Karin Rosenstein**. Genes Regulated by Estrogen and Progesterone in Human Endometrium. 2016.
204. **Aleksei Tretjakov**. A Macromolecular Imprinting Approach to Design Synthetic Receptors for Label-Free Biosensing Applications. 2016.
205. **Mati Danilson**. Temperature Dependent Electrical Properties of Kesterite Monograin Layer Solar Cells. 2016.
206. **Kaspar Kevvai**. Applications of ^{15}N-labeled Yeast Hydrolysates in Metabolic Studies of *Lactococcus lactis* and *Saccharomyces cerevisiae*. 2016.
207. **Kadri Aller**. Development and Applications of Chemically Defined Media for Lactic Acid Bacteria. 2016.
208. **Gert Preegel**. Cyclopentane-1,2-dione and Cyclopent-2-en-1-one in Asymmetric Organocatalytic Reactions. 2016.
209. **Jekaterina Služenikina**. Applications of Marine Scatterometer Winds and Quality Aspects of their Assimilation into Numerical Weather Prediction Model HIRLAM. 2016.